2014

CLUSTERS BRIDGING DISCIPLINES

Swayamprabha Behera
Virginia Commonwealth University

CLUSTERS BRIDGING DISCIPLINES

A dissertation submitted in partial fulfillment of the requirements for the degree of

Doctor of Philosophy in Nanoscience and Nanotechnology

at Virginia Commonwealth University

By

Swayamprabha Behera

M.S. in Physics/Applied Physics

Virginia Commonwealth University, 2011

Director: Purusottam Jena, Ph. D.

Distinguished Professor, Department of Physics

Virginia Commonwealth University

Richmond, Virginia, 23284

August, 2014

Acknowledgment

Working on my Ph.D. has been a wonderful and overwhelming experience. I am indebted to many people who have contributed their valuable insights for making my Ph.D. a joyful, comprehensive and an unforgettable experience.

I am deeply grateful to my supervisor Dr. Puru Jena, whose constant encouragement, supervision and support from the preliminary to the concluding level, has enabled me to develop an understanding of the subject. To work with him has been a real pleasure and honor for me. His advice on both researches as well as on my career aspects has been invaluable. Above all, I earnestly appreciate his fatherly affection and care.

Dr. Jena is an amazing scientist. His compassion for physics is commendable. Sometime we get very confused from the awkward results we get from our calculations, but the way he explains the phenomena and his deep understanding behind the problem is surprising and fills us with enthusiasm to work on the problem. In spite of his busy schedule he is always approachable.

I would like to thank Dr. Hani El Kaderi at Virginia Commonwealth University, Dr. Gerd F. Gantefo¨r at University of Konstanz, Dr. K. H. Bowen at Johns Hopkins University, Dr. Gennady Gutsev and Dr. Anil Kandalam for their collaboration.
I would also like to thank Dr. Hani El Kaderi, Dr. Marilyn Bishop and Dr. Dexian Ye for serving as my committee members.

A special thank to my research group members especially Mary, Devleena, Santanab (Dr. Santanab Giri), Jian (Dr. Jian Zhou), Brandon, Jorly (Dr. Jorly Joseph), Kalpa (Dr. Kalpataru Pradhan), Kung (Dr. Kung Tao), Miao Miao (Dr Miao Miao Wu), Dr. Wang and Dr. Sun for their discussion, guidance, proof reading my thesis, and spending fun time during lunch and coffee. I am thankful to all other classmates who directly or indirectly contributed to the successful completion of my Ph.D. degree.

I would like to thank the VCU computer center and National Energy Research Scientific Computing Center (NERSC), for carrying out my computational research. Without their support my work would not have been possible.

Last but not least, I wish to thank my loving husband Govind, for his encouragement, support, and patience to peruse my career in USA. My parents and family have given me their unequivocal support throughout, for which my mere expression of thanks does not suffice. A special thank to my loving and precious 14 months old daughter, Anvita whose smile takes away all my worries and revitalizes me.

Table of Contents

Acknowledgement……...ii
Table of Contents……iv
List of Figures……...viii
List of Tables……xiii
Abstract……..xv
Chapter 1: Introduction……1
1.1 A Brief History……..2
1.2 Electron Counting Rules……4
1.3 Theoretical Approach and Experimental techniques…….7
1.4 Synopsis…….9
References……..11
Chapter 2: Theoretical Methods…….14
2.1 The Schrodinger Equation……..14
2.2 The Born-Oppenheimer Approximation……..16
2.3 The Hartree Approximation.……18
2.4 The Hartree-Fock Approximation.……...19
2.5 Density Functional Theory.…….22
2.5.1 Thomas-Fermi-Dirac Approximation……...22
2.5.2 Hohenberg-Kohn Formulation.…….23
2.5.3 Kohn-Sham Equations.…….25
2.5.4 Functionals for Exchange-Correlation.…….27
2.5.4.1 The Local Density Approximation (LDA) ……..27

2.5.4.2 The Generalized Gradient Approximation (GGA) ……..28

2.5.4.3 The Hybrid GGA Functional……29

2.5.4.4 The Hybrid meta-GGA Functional……30

2.6 Basis sets.……31

2.7 Computational Methodology……...33

References……..37

Chapter 3: Clusters as Superatoms……40

3.1 Clusters mimicking properties of halogens: '*Superhalogens*' ……42

3.1.1 Introduction……...42

3.1.2 Results and Discussions……45

3.1.2.1 Onset of Superhalogen Behavior in NO_x ……..45

3.1.2.2 MNO_3; M = Li, Mg, Al……..47

3.1.2.3 $M(NO_3)_2$; M = Li, Mg, Al……..49

3.1.2.4 $M(NO_3)_3$; M = Mg, Al……...50

3.1.2.5 $M(NO_3)_4$; M = Al……..52

3.1.2.6 Stability with respect to fragmentation …….53

3.1.2.7 Designing Hypersalts using Superhalogen ligand…….54

3.1.3 Conclusion……56

3.2 Clusters mimicking properties of alkalis: '*Superalkalis*'…….57

3.2.1 Introduction……..57

3.2.2 Results and Discussions……58

3.2.2.1 Designing Supersalts using Superalkalis and Superhalogens……58

3.2.2.1.1 Superalkalis…….58

3.2.2.1.2 Superhalogens…….59

3.2.2.1.3 Supersalts……60

3.2.2.2 Designing Hyperhalogens using Superalkali core…….65

3.2.3 Conclusion……71

3.3 Clusters mimicking the chemistry of catalysts ……...71

3.3.1 Introduction……...71

3.3.2 Results and Discussions……74

3.3.2.1 Comparison between Pd_n and $(ZrO)_n$ (for n=1-5)…….75

3.3.2.2 Interaction of gas molecules (H_2, O_2 and CO) with neutral Pd_n and $(ZrO)_n$ clusters (n=1-3)…….77

3.3.2.3 Interaction of gas molecules (H_2, O_2 and CO) with cationic Pd_n and $(ZrO)_n$ clusters (n=1-3)…….84

3.3.2.4 Interaction of gas molecules (H_2, O_2 and CO) with anionic Pd_n and $(ZrO)_n$ clusters (n=1-3)…….88

3.3.3 Conclusion……92

References……..94

Chapter 4: Reaction of Hydrogen with Coinage Metal Clusters…….....102

4.1 Interaction mechanism of hydrogen with Cu_n and Ag_n clusters (n=1-5)…...103

4.1.1 Introduction…….103

4.1.2 Results and Discussions …….104

4.1.2.1 Cu_n and $Cu_{n-1}H$ clusters……...104

4.1.2.2 Ag_n and $Ag_{n-1}H$ clusters ……..113

4.1.3 Conclusion……...……...119

References……121

Chapter 5: Gas Storage and Sequestration – A Cluster Approach……..123

5.1. Gas uptake by borazine-linked polymer (BLPs)……...125

5.1.1 Introduction…….125

5.1.2 Theoretical methods……126

5.1.3 Results and Discussions……..127

5.1.4 Conclusions…….130

5.2 Gas uptake by benzimidazole-linked polymers (BILPs) ……..130

5.2.1 Introduction…….130

5.2.2 Theoretical methods……....131

5.2.3 Results and Discussions……..131
5.2.4 Conclusions…….136
References……137
Chapter 6: Summary……139
6.1 Major findings……139
6.2 Ongoing research……...142
Appendix I……...143
Appendix II……..……150
Appendix III…….156

List of Figures

Figure 3-1: Optimized geometry of neutral and anionic NO_x (x = 1−3)……...45

Figure 3-2: Optimized geometries of neutral and anionic MNO_3 (M =Li, Mg, Al)
(a) $LiNO_3$, (b) $MgNO_3$, and (c) $AlNO_3$……..48

Figure 3-3: Optimized geometries of neutral and anionic $M(NO_3)_2$ (M = Li, Mg, Al)
(a) $Li(NO_3)_2$, (b) $Mg(NO_3)_2$, and (c) $Al(NO_3)_2$……..50

Figure 3-4: Optimized geometries of neutral and anionic $M(NO_3)_3$ (M = Mg, Al).
(a)$Mg(NO_3)_3$ and (b) $Al(NO_3)_3$……..51

Figure 3-5: Optimized geometries of neutral and anionic $M(NO_3)_4$ (M = Al)……..52

Figure 3-6: Ground-state structures of (from left) $KLi(NO_3)_2$, $KMg(NO_3)_3$, and $KAl(NO_3)_4$. The first row and the second row are the front and the side views of the respective salts' clusters…….55

Figure 3-7: Optimized geometries of superalkalis (from left: Li_3O^+, Cs_2Cl^+, $Cs_2NO_3^+$)...59

Figure 3-8: Optimized geometries of superhalogens (from left: BF_4^-, BeF_3^-, NO_3^-)…….59

Figure 3-9: Optimized geometries of isomers of $(Li_3O)(BF_4)$ supersalt. The ground state is defined as ΔE = 0.0 eV……...61

Figure 3-10: Optimized geometries of (a) $(Li_3O)(BeF_3)$ and (b) $(Li_3O)(NO_3)$ supersalts……62

Figure 3-11: Optimized geometries of isomers of $(Li_3O)(BF_4)_2$ molecules. The ground state is defined as ΔE = 0.0 eV…….66

Figure 3-12: Optimized geometries of isomers $(Li_3O)(BeF_3)_2$ molecules. The ground state is defined as ΔE = 0.0 eV…….67

Figure 3-13: Optimized geometries of isomers $(Li_3O)(NO_3)_2$ and $(Li_3O)_2(NO_3)_3$ molecules……...68

Figure 3-14: Optimized geometries of $(Cs_2Cl)(NO_3)_2$ and $(Cs_2NO_3)(NO_3)_2$ molecules...69

Figure 3-15: Ground state geometries with electronic state of neutral $(ZrO)_n$ and Pd_n (n = 2-5) clusters……75

Figure 3-16: Ground state geometries of H_2 interacting with neutral Pd_n and $(ZrO)_n$ clusters. The bond lengths are given in Å and the NBO charges are given in units of electron charge, e……...78

Figure 3-17: Ground state geometries of O_2 interacting with neutral Pd_n and $(ZrO)_n$ clusters. The bond lengths are given in Å and the NBO charges are given in units of electron charge, e……...80

Figure 3-18: Ground state geometries of CO interacting with neutral Pd_n and $(ZrO)_n$ clusters. The bond lengths are given in Å and the NBO charges are given in units of electron charge, e……...82

Figure 3-19: Ground state geometries of H_2 interacting with cationic Pd_n and $(ZrO)_n$ clusters. The bond lengths are given in Å and the NBO charges are given in units of electron charge, e……...85

Figure 3-20: Ground state geometries of O_2 interacting with cationic Pd_n and $(ZrO)_n$ clusters. The bond lengths are given in Å and the NBO charges are given in units of electron charge, e……...86

Figure 3-21: Ground state geometries of CO interacting with cationic Pd_n and $(ZrO)_n$ clusters. The bond lengths are given in Å and the NBO charges are given in units of electron charge, e……...87

Figure 3-22: Ground state geometries of H_2 interacting with anionic Pd_n and $(ZrO)_n$ clusters. The bond lengths are given in Å and the NBO charges are given in units of electron charge, e……...89

Figure 3-23: Ground state geometries of O_2 interacting with anionic Pd_n and $(ZrO)_n$ clusters. The bond lengths are given in Å and the NBO charges are given in units of electron charge, e……...90

Figure 3-24: Ground state geometries of CO interacting with anionic Pd_n and $(ZrO)_n$ clusters. The bond lengths are given in Å and the NBO charges are given in units of electron charge, e……...91

Figure 4-1: Photoelectron spectra of Cu^-, Cu_n^-, and $Cu_{n-1}H^-$ (n = 2–5). The insets in the spectra of Cu_2H^- and Cu_4H^- are an expanded version of the peak found at 1.46 eV and 1.51 eV, respectively……..105

Figure 4-2: Optimized anionic and neutral geometries of CuH and Cu_2. Bond lengths (in Å) and NBO charges (in brackets) are given…….107

Figure 4-3: Optimized anionic and neutral geometries of Cu_2H and Cu_3. Bond lengths (in Å) and NBO charges (in brackets) are given……108

Figure 4-4: Optimized anionic and neutral geometries of Cu_3H and Cu_4. Bond lengths (in Å) and NBO charges (in brackets) are given……...109

Figure 4-5: Optimized anionic and neutral geometries of Cu_4H and Cu_5. Bond lengths (in Å) and NBO charges (in brackets) are given……...111

Figure 4-6: Plots of the highest occupied molecular orbitals (HOMOs) of Cu_n^- and $Cu_{n-1}H^-$ for $n \geq 3$ (isovalue 0.02 $Å^{-3}$)……112

Figure 4-7: Photoelectron spectra of Ag^-, Ag_n^-, and $Ag_{n-1}H^-$ (n = 2–5)…….113

Figure 4-8: Optimized anionic and neutral geometries of AgH and Ag_2. Bond lengths (in Å) and NBO charges (in brackets) are given……...114

Figure 4-9: Optimized anionic and neutral geometries of Ag_2H and Ag_3. Bond lengths (in Å) and NBO charges (in brackets) are given……...115

Figure 4-10: Optimized anionic and neutral geometries of Ag_3H and Ag_4. Bond lengths (in Å) and NBO charges (in brackets) are given……..116

Figure 4-11: Optimized anionic and neutral geometries of Ag_4H and Ag_5. Bond lengths (in Å) and NBO charges (in brackets) are given……..117

Figure 4-12: Plots of the highest occupied molecular orbitals (HOMOs) of Ag_n^- and $Ag_{n-1}H^-$ for $n \geq 3$ (isovalue 0.02 $Å^{-3}$)……...119

Figure 5-1: Optimized geometries of (a) H_2, (b) CO_2, and (c) CH_4 adsorbed onto chlorinated borazine calculated from the M06/6-311+G* level of theory. Bond lengths are in Å. Front and side views are given on the left and right panel respectively……...129

Figure 5-2: Fully optimized geometries of (a) BILP-4@2SO_2 and (b) BILP-4@4SO_2. The bond lengths are in Å……...132

Figure 5-3: Partially optimized geometries of (a) BILP-3@3SO_2 and (b) BILP-3@6SO_2. The bond lengths are in Å……134

Figure I1: Isomers of neutral and anionic clusters of $LiNO_3$ optimized using B3LYP/6-311++G** showing the energy difference (ΔE) measured with respect to its ground state counterpart……...143

Figure I2: Isomers of neutral and anionic clusters of $Li(NO_3)_2$ optimized using B3LYP/6-311++G** showing the energy difference (ΔE) measured with respect to its ground state counterpart……...144

Figure I3: Isomers of neutral and anionic clusters of $MgNO_3$ optimized using B3LYP/6-311++G** showing the energy difference (ΔE) measured with respect to its ground state counterpart……...145

Figure I4: Isomers of neutral and anionic clusters of $Mg(NO_3)_2$ optimized using B3LYP/6-311++G** showing the energy difference (ΔE) measured with respect to its ground state counterpart……...146

Figure I5: Isomers of neutral and anionic clusters of $Mg(NO_3)_3$ optimized using B3LYP/6-311++G** showing the energy difference (ΔE) measured with respect to its ground state counterpart……...147

Figure I6: Isomers of neutral and anionic clusters of $AlNO_3$ optimized using B3LYP/6-311++G** showing the energy difference (ΔE) measured with respect to its ground state counterpart……...148

Figure I7: Isomers of neutral and anionic clusters of $Al(NO_3)_2$ optimized using B3LYP/6-311++G** showing the energy difference (ΔE) measured with respect to its ground state counterpart……...148

Figure I8: Isomers of neutral and anionic clusters of $Al(NO_3)_4$ optimized using B3LYP/6-311++G** showing the energy difference (ΔE) measured with respect to its ground state counterpart……...149

Figure II1: Isomers for the adsorption of H_2, O_2 and CO to neutral Pd. The energy difference (ΔE) is measured with respect to its ground state……...150

Figure II2: Isomers for the adsorption of H_2, O_2 and CO to neutral ZrO. The energy difference (ΔE) is measured with respect to its ground state……...151

Figure II3: Isomers for the adsorption of H_2, O_2 and CO to neutral Pd_2. The energy difference (ΔE) is measured with respect to its ground state……...152

Figure II4: Isomers for the adsorption of H_2, O_2 and CO to neutral $(ZrO)_2$. The energy difference (ΔE) is measured with respect to its ground state……...153

Figure II5: Isomers for the adsorption of H_2, O_2 and CO to neutral Pd_3. The energy difference (ΔE) is measured with respect to its ground state……..154

Figure II6: Isomers for the adsorption of H_2, O_2 and CO to neutral $(ZrO)_3$. The energy difference (ΔE) is measured with respect to its ground state……...155

Figure III1: Optimized geometries of (a) H_2, (b) CO_2 and (c) CH_4 adsorbed on chlorinated borazine calculated at LDA/6-311+G* level of theory. The bond lengths are in Å. Front and side views are given on the left and right panel, respectively……156

Figure III2: Optimized geometries of (a) H_2, (b) CH_4 adsorbed on chlorinated borazine calculated at B3LYP/6-311+G* level of theory. The bond lengths are in Å. Front and side views are given on the left and right panel, respectively…….157

FigureIII3: Fully optimized geometries of (a) BILP-4@2SO_2 and (b) BILP-4@4SO_2 calculated at LDA/6-311+G* level of theory. The bond lengths are in Å……...158

Figure III4: Partially optimized geometries of (a) BILP-3@3SO_2 and (b) BILP-3@6SO_2 calculated at LDA/6-311+G* level of theory. The bond lengths are in Å. Front and side views are given on the left and right panel respectively……..159

Figure III5: Fully Optimized geometries of BILP-3@6SO_2 calculated at (a) LDA/6-311+G* and (b) M06/6-311+G* level of theory…….160

List of Tables

Table 3-1: Electron Detachment Energies of NO_x (x = 1−3) and MNO_3 (where M = Li, Mg, Al)……...46

Table 3-2: Electron Detachment Energies of $M(NO_3)_x$ clusters at the B3LYP/6-311++G** level of theory……..53

Table 3-3: Fragmentation Energies of the $M(NO_3)_x$ Clusters……54

Table 3-4: Fragmentation Energies of the Hypersalts $KM(NO_3)_x$……56

Table 3-5: Calculated Vertical Ionization Potential (VIP), Electron Affinity (EA), Vertical Detachment Energy (VDE), and Binding Energy (ΔE) of the studied superalkali, superhalogen, supersalt, and potential hyperhalogen complexes; (a), (b), and (c) represent different isomers for a particular system……...64

Table 3-6: Electron Affinity (EA), Vertical Ionization Potential (IP), Hardness (η) and Binding Energy (E_b) of $(ZrO)_n$ and Pd_n clusters where n=1-5. Available experimental results are given in parentheses……..76

Table 3-7: Adsorption energies (E_{ads}) in eV and electronic states in parentheses of neutral Pd_n and $(ZrO)_n$ (n=1-3) clusters interacting with H_2, O_2 and CO…….83

Table 3-8: Adsorption energies (E_{ads}) in eV and electronic states in parentheses of Pd_n^+ and $(ZrO)_n^+$ (n=1-3) clusters interacting with H_2, O_2 and CO……..88

Table 3-9: Adsorption energies (E_{ads}) in eV and electronic states in parentheses of Pd_n^- and $(ZrO)_n^-$ (n=1-3) clusters interacting with H_2, O_2 and CO……..92

Table 4-1: Experimental and theoretical results of vertical detachment energies (VDEs) and theoretical electron affinities (EAs) in eV of Cu_n and $Cu_{n-1}H$…….....106

Table 4-2: Experimental and theoretical results of Vertical Detachment Energies (VDEs) and theoretical Electron Affinities (EAs) in eV of Ag_n and $Ag_{n-1}H$……114

Table 5-1: Comparison of calculated binding energy of CO_2, H_2 and CH_4 to CB with experimental values…….128

Table 5-2: Binding energies (E_b) of BILP-4@*n*SO_2 (n=2, 4) and BILP-3@*n*SO_2 (n=3, 6) using different methods……..135

Table III-1: Binding affinities (E_b) of BILP-3@*n*SO_2 (n=3, 6) using different methods after fully optimizing the geometries……...160

Abstract

CLUSTERS BRIDGING DISCIPLINES

By Swayamprabha Behera, Ph.D.

A dissertation submitted in partial fulfillment of the requirements for the degree of Doctor of Philosophy in Nanoscience and Nanotechnology at Virginia Commonwealth University

Virginia Commonwealth University, 2014

Director: Purusottam Jena, Ph. D.

Distinguished Professor, Department of Physics

Clusters constitute an intermediate state of matter between molecules and solids whose properties are size dependent and can be tailored. In recent years, cluster science has become one of the most exciting areas of research since their study can not only bridge our understanding between atoms and their bulk but also between various disciplines. In addition, clusters can serve as a source of new materials with uncommon properties. This dissertation deals with an in-depth

study of clusters as a bridge across physics, chemistry, and materials science and provides a fundamental understanding of the structure-property relationships by focusing on three different topics. The first topic deals with superatoms which are clusters that mimic the chemistry of atoms. I show that superhalogens and superalkalis can be designed to mimic the chemistry of halogen and alkali atoms, respectively. An entirely new class of salts can then be synthesized by using these superatoms as the building blocks. I have also explored the possibility of designing highly electronegative species called hyperhalogens by using superhalogens as ligands or superalkalis as core and a combination of both. Another aspect of my work on superatom is to examine if traditional catalysts (namely Pd) can be replaced by clusters composed of earth-abundant elements (namely Zr and O). This is accomplished by comparing the electronic structure and reactivity of Pd clusters with isoelectronic ZrO clusters. The second topic deals with a study of the electronic structure of coinage metal (Cu and Ag) clusters and see if they remain unchanged when a metal atom is replaced by an isoelectronic hydrogen atom as is the case with Au-H clusters. The third topic deals with clusters as model of polymeric materials to understand their gas storage and sequestration properties. This is accomplished by studying the trapping of H_2, CO_2, CH_4 and SO_2 molecules in borazine-linked polymers (BLPs) and benzimidazole-linked polymers (BILPs). The first two topics provide a bridge between physics and chemistry, while the third topic provides a bridge to materials science.

Chapter 1

INTRODUCTION

Clusters are defined as finite aggregates of atoms and may contain from a few to tens of thousands of atoms. They are the fundamental form of matter in which every atom and every charge counts. The forces that bind them together may vary from strong metallic to weak van der Waals or from ionic to covalent bonds.

The properties of clusters are unique and change non-monotonically with the addition of even a single atom. Their properties are very different from those of the corresponding bulk phases. For example, bulk gold, which is known to be chemically inert, becomes very reactive when cluster sizes are below 2-3 nm[1,2]. V and Rh, which are paramagnetic in bulk, become ferromagnetic when they form small clusters[3,4]. Mn, which is antiferromagnetic in bulk, becomes ferromagnetic in clusters containing five or fewer atoms and shows ferrimagnetic behavior in larger clusters[5,6]. Cu clusters smaller than 50 nm are considered to be super hard materials that do not exhibit the same malleability and ductility as bulk Cu. Thus the properties of clusters depend on their size. They vary drastically for smaller clusters, and as size increase, the variation of properties become less significant. These properties approach those of the corresponding bulk phase for very large clusters. The particular size of the cluster at which its transition to the

corresponding bulk occurs is difficult to determine. This transition depends upon the types of atoms forming the cluster and the properties being studied. Many of the differences between clusters and bulk arise due to a quantum confinement effect, where the electrons are confined to a potential well. In this case, the electrons fill discrete energy levels instead of having the continuous bands that are characteristic of a solid. A systematic study of the electronic structure and properties of the clusters as a function of size can provide a bridge that links atoms, molecules and the bulk phase.

1.1 A Brief History:

The origin of cluster science as we know it today dates back to the first set of experiments using mass spectrometer ion source in the 1950s[7]. The next considerable advance occurred in the 1960s when intense molecular beams[7] at low temperature were used to produce clusters by supersonic expansion. The discoveries of these two techniques were one of the most important factors in the growth of cluster science. During this time, molecular clusters of inert gas atoms and of low melting point metals were the subject of considerable interest. In the 1980s, studies of clusters progressed rapidly with the development of the laser vaporization techniques[8] which enabled researchers to produce clusters of any element in the periodic table. In this technique, a given element or material is vaporized by a laser pulse in the presence of an inert carrier gas, usually helium, and the products of clustering in the cooling plasma are studied by mass spectroscopy.

Cluster science has become a robust field of research in the past four decades. While many unique properties of clusters have been found over the years, two discoveries, made near simultaneously, stand out. The first one, reported by W. D. Knight, K. Clemenger, W. A. de Heer,

W. A. Saunders, M. Y. Chou and M. L. Cohen in 1984, is the discovery of magic numbers in the mass spectra of free small sodium clusters[9]. This study was made by vaporizing an alkali metal from a gas aggregation source, ionizing the resulting clusters, and measuring the evolving cluster distribution using time-of-flight mass spectroscopy. Intense peaks were found corresponding to clusters containing magic number of atoms *i.e,* 2, 8, 18, 20, 34, 40 *etc.* that are unusually stable. These magic numbers are characterized by the formation of discrete electronic shells separated by energy gaps. In short, clusters with filled electronic shells are more stable and less reactive than clusters with open shells. This behavior can be explained from the fact that, inert gas atoms such as He, Ne, Ar, Kr, Xe, and Rn are chemically unreactive due to their filled electronic shells. The second key work was the discovery of the C_{60} fullerene in the gas phase by H. W. Kroto, J. R. Heat, S. C. O'Brian, R. F. Curl and R. E. Smalley[10] in 1985. Synthesis of C_{60} clusters in macroscopic quantities[11] later in 1990 allowed their assembly into fulleride crystals. It has been one of the most exciting developments in cluster science and it is the only elemental cluster that has been assembled to form a solid. The properties of fulleride crystal are very different from graphite and diamond although each of these materials is composed of carbon atoms as building blocks. For example, the bonding between C_{60} molecules are van der Waals in character, the carbon atom in graphite and diamond, on the other hand, are covalent in nature. The discovery of magic number and the fullerene clusters were made possible by the efforts in many laboratories and confirmed that materials composed of clusters are very different from those of assembled from atoms. While the initial focus in cluster research was to understand how the properties of matter evolve one atom at a time, these two seminal works pointed to a new direction.

Later in 1992, Khanna and Jena[12] introduced the idea behind the feasibility of producing materials *via* cluster assembly, known as cluster assembled material (CAM). This strategy is a

bottom-up approach for designing novel nanoscale materials, as opposed to the *top-down* approach, which involve successive subdivision of bulk matter. For such materials to exist, each cluster has to be stable to from the building units. Such an ideal situation can be realized when the geometric close packing as well as electronic shell closing could be simultaneously achieved to enhance its stability[12] . Such clusters not only have the desired properties but also are strong enough that they remain intact when assembled to form the extended material and the materials assembled from them exhibit properties very different from those composed of individual atoms[13].

Designing of novel materials by assembling cluster involves three synergistic steps[14]. First, stable clusters should be identified from theoretical calculations. One of the guiding principles to identify such clusters is by following electron counting rules; a brief description of these rules is given in the following section. Second, theoretical predictions must be verified by experiments in the gas phase. Some of the widely used experimental techniques that produce cluster are mentioned in the section 1.3. Third, these clusters should be assembled in bulk form using synthetic chemical approaches. However, one may encounter practical problems in synthesizing cluster materials. The major difficulty is their metastablility, which makes them coalesce to form larger clusters and, thus, destroying their original properties. Potentially, there are various ways to overcome this, such as passivating them with organic ligands[15], inserting them into a cage[16] or depositing them on proper surfaces[17].

1.2 Electron Counting Rules:

To speed up theoretical investigation of stable clusters, electron counting rules have been known to play an important role. Some of the widely used electrons counting rules are the

Jellium rule, *Octet rule*, *18-electron rule*, *Wade-Mingos rule and Aromaticity rule*. Each of them is described below:

(a) *Jellium rule*[9]*:* This model is described by Knight *et al*[9] where the charge of all nuclei and core electrons in the cluster are uniformly distributed throughout the size of the cluster. The energy levels of the electrons are maintained with a specific potential and corresponds to $1S^2$, $1P^6$, $1D^{10}$, $2S^2$, $1F^{14}$ and so on. The electrons are filled in the shell according to Pauli's exclusion principle. As the shells are filled, clusters containing 2, 8, 20, 40 *etc.* electrons become more stable as they correspond to closed shells. This rule accounts for the stability of free electron metal clusters containing magic numbers of atoms and can also be applicable for charged as well as heteroatomic clusters. Na_n^+ clusters[18] where number of Na atoms corresponding to n = 3, 9, 21, 41, and so on are examples for charged magic clusters, where KAl_{13} and Na_2Al_6 containing 40 and 20 electrons respectively are examples for the heteroatomic magic clusters. Magic clusters are characterized by having large HOMO-LUMO gaps and are less reactive than those with open shell electronic shells.

(b) *Octet rule*[19,20]*:* This rule is responsible not only for the inertness of noble gas atoms but also for the reactivity of elements such as alkali metals and halogens. According to this rule, eight electrons are required to complete the valence of a simple element and to attain a noble gas configuration. This rule is applicable to elements with atomic number < 20. This rule can be used to theoretically design clusters that mimic the chemistry of elements in the periodic table. Two examples that belong to this category are superhalogens and superalkalis. This class of clusters is discussed in depth in chapter 3.

(c) *Eighteen-electron rule:* As per this rule, 18 valence electrons (10 *d*-electrons, 2 *s*-electrons and 6 *p*-electrons) are required to complete the electronic shell[21]. This rule has been successful in explaining a wide range of transition metal complexes. Some examples include: Ferrocene $[Fe(C_5H_5)_2]$ and Nickel Carbonyl $[Ni(CO)_4]$ where Fe and Ni have the electronic configuration of $3d^64s^2$ and $3d^84s^2$. The ligands, C_5H_5 and CO contribute respectively, five and two electrons to the valence pool, thus the total number of electrons involved in both of the molecules are 18. Similarly, in icosahedral $Au_{12}W$ cluster, W contributes six valence electrons and Au atom being monovalent contributes 1, thus, the total number of electrons is 18. This has been predicted theoretically[22] and confirmed experimentally[23].

(d) *Wade-Mingos rule*[24,25]*:* Originally this rule was formulated by Wade, and later, further developed by Mingos to predict the structure of electron deficient clusters such as boranes and carboranes. One example is the borane cluster B_nH_n, where B_n forms a polyhedron with *n* vertices and each H-atom is radially bonded. Each BH pair in this cluster contributes four valence electrons, of which 2 are involved in the covalent bond between B and H, and two are involved in cage bonding. According to this rule, $(2n+1)$ pairs of electrons are required for cage bonding. Hence $B_nH_n^{2-}$ referred to as *closoboranes*, represents a stable cluster.

(e) *Aromaticity rule*: This rule accounts for the stability of σ/Π-electron systems and is based on 'Hückel's rule' which states that a system containing $(4n+2)$ delocalized σ/Π electrons are stable and are called aromatic, whereas a cluster containing $4n$ σ/Π electrons are unstable and are antiaromatic (where n is an integer). Aromaticity is associated with extra stability arising from

the electron delocalization in complete circuits. Examples for aromatic and antiaromatic systems are respectively benzene and cyclobutadiene.

In my dissertation, I will make use of some of these rules to design clusters with tailored properties. As discussed earlier, synthesis of stable cluster assembled materials requires a synergy between theory and experiment. Theoretical investigations not only allow a fundamental understanding but also as a predictive basis for guiding new experimental works. A brief description of both these approaches is given in the following section.

1.3 Theoretical Approach and Experimental Techniques:

In the last thirty years, cluster science has become a rapidly expanding field of interdisciplinary study as experimental and theoretical techniques have advanced and computational power has increased. These techniques play a crucial role in studying the behavior of clusters. On the experimental side, the developments of innovative techniques allow for the synthesis, characterization, and investigation of the properties of selected clusters of any size and composition, whereas on the theoretical side, developments in theoretical methods, aided by the progress in computational resources, helps to understand the structure-dependent properties of clusters, which are difficult to determine directly and unambiguously using experiments. A synergistic effort between both helps not only in the synthesis of novel nanomaterials but also in understanding their unique characteristics.

Structures of clusters are markedly different from their bulk counterparts. Bulk solid primarily exhibits 14 different lattice symmetries, the most prevalent being the body-centered cubic (bcc), face centered cubic (fcc) and hexagonal closed-packed (hcp). For example, alkali

metals such as Li form bcc structures, coinage metals such as Au form fcc structures, and transition metals such as Ti form hcp structures. On the other hand, a given composition of a cluster has several distinct isomers. This makes the determination of the lowest energy geometry very difficult. In current theoretical approaches, in order to obtain the lowest energy structure of a specific cluster, geometries are optimized by starting with a large number of initial configurations. Any isomer lying within a very small energy range of the lowest energy structure is considered as potential candidate for the ground state geometry. The isomer in the narrow energy range whose properties are in agreement with experimental results is then considered as the preferred ground state of the cluster. It is also possible that experimentally one may not always observe the ground state structure. Theoretical methods based on quantum chemical approaches and density functional theory is able to provide accurate and often quantitative information on the ground state structures and properties of clusters.

The experimental techniques that are mostly used are photoelectron spectroscopy (PES)[26], trapped ion electron diffraction (TIED)[27], ion mobility spectrometry (IMS) [28] and infrared absorption spectroscopy (IRAS)[29]. The PES, TIED and IMS techniques are carried out on *charged* clusters whereas the IRAS experiment provide information on *neutral* clusters. The PES experiment is conducted only on anionic clusters, whereas IMS and TIED experiments can be conducted on both anionic and cationic clusters. Using a PES experiment, one can measure the adiabatic electron affinity (AEA) and vertical detachment energy (VDE), which can be used to deduce the structural properties of a cluster by comparing with the theoretically computed results. The details on computational calculations are given in section 2.7 of Chapter 2. In the TIED technique, on the other hand, one compares the entire simulated diffraction pattern of

theoretically generated candidate geometries with the experiment. IRAS technique measures the vibrational spectra of the clusters and directly reflects their symmetry.

1.4 Synopsis:

Studies on clusters can not only bridge our understanding between atoms and their bulk counterparts, but can also create a bridge between various disciplines. Understanding various properties of clusters helps us to deal with problems that exist in many different fields of science. In a series of articles[30,31,32] in the *Proceedings of the National Academy of Sciences*, Jena and Castlemann has shown how the field of cluster science have bridged between various disciplines such as physics, chemistry, environmental science, materials science and biology.

My Ph.D. dissertation involves the use of clusters as a bridge connecting physics, chemistry, and materials science. The work described here is theoretical and its aim is to provide a fundamental understanding of the structure-property relationships of clusters. The evolution of properties such as ionization potentials (IPs), electron affinities (EAs), vertical detachment energies (VDEs), binding energies, dissociation energies, HOMO-LUMO gaps, hardness (η), and reactivity of the clusters as a function of size and composition were studied. Some works have also been conducted in joint collaboration with experimental groups.

The dissertation progresses in the following way. The first project involves the theoretical design of clusters that mimic the chemistry of atoms in the periodic table. This class of cluster is known as a *superatom*. The work focusses on three different kinds of atoms, namely, halogens, alkali metals, and transition metal atoms. The first category includes the theoretical design of superhalogens whose properties not only mimic halogen atoms but are better oxidizing agents than halogens. The second category consists of superalkalis whose properties not only mimic

alkali metal atoms, but also their preference to donate an electron is higher than those of alkali metal atoms. In the third class of clusters consisting of a transition metal oxide, namely ZrO whose properties may represent that of Pd, a known catalyst. The details on this class of cluster are discussed in Chapter 3.

My second project is based on the use of clusters for studying reactions. Catalysis plays an important role in the chemical industry and industrial research. Current knowledge for designing desired catalytic systems has long been a major challenge. The field of cluster science plays a major role in understanding the basic reaction mechanisms in catalysis. The project based on this class of clusters involves coinage metal clusters interacting with hydrogen. The details on this class of cluster are discussed in Chapter 4.

Clusters have been used in the past as models to study the properties of extended systems such as crystals and proteins by replacing such systems with a few atoms confined to the geometry of their bulk counterpart[33]. Based on this, my third project involves the use of clusters as a model of polymeric systems for understanding their gas storage and sequestration mechanisms. Two new polymers, namely borazine-linked polymers (BLPs) and benzimidazole-linked polymers (BILPs), were synthesized in El Kaderi's group that have shown exceptionally high uptake for gases such as H_2, CO_2, CH_4 and SO_2. We performed the theoretical studies using the polymeric building units to understand the reason behind its high uptake and the relevant interaction mechanism. The details on the theoretical investigations are discussed in Chapter 5.

My dissertation is organized as follows: The theoretical methods are described in Chapter 2. Chapter 3, 4 and 5 are devoted to discuss various properties of clusters. Finally, the summary of all the works along with ongoing research is given in Chapter 6.

References

[1] Valden, M., Lai, X. & Goodman, D. W. Onset of catalytic activity of gold clusters on titania with the appearance of nonmetallic properties. *Science* **281,** 1647–1650 (1998).

[2] Haruta, M. *et al.* Low-Temperature Oxidation of Co Over Gold Supported on TiO_2, Alpha-Fe_2O_3, and Co_3O_4. *J. Catal.* **144,** 175–192 (1993).

[3] Liu, F., Khanna, S. & Jena, P. Magnetism in Small Vanadium Clusters. *Phys. Rev. B* **43,** 8179–8182 (1991).

[4] Bucher, J., Douglass, D. & Bloomfield, L. Magnetic-Properties of Free Cobalt Clusters. *Phys. Rev. Lett.* **66,** 3052–3055 (1991).

[5] Nayak, S. K. & Jena, P. Anomalous magnetism in small Mn clusters. *Chem. Phys. Lett.* **289,** 473–479 (1998).

[6] Knickelbein, M. B. Experimental observation of superparamagnetism in manganese clusters. *Phys. Rev. Lett.* **86,** 5255–5257 (2001).

[7] Becker, E. W., in *Metal Clusters*, eds. Trager, F. & Putlitz, G. (Springer, Berlin), 1986.

[8] Dietz, T., Duncan, M., Powers, D. & Smalley, R. Laser Production of Supersonic Metal Cluster Beams. *J. Chem. Phys.* **74,** 6511–6512 (1981).

[9] Knight, W. *et al.* Electronic Shell Structure and Abundances of Sodium Clusters. *Phys. Rev. Lett.* **52,** 2141–2143 (1984).

[10] Kroto, H., Heath, J., Obrien, S., Curl, R. & Smalley, R. C-60 - Buckminsterfullerene. *Nature* **318,** 162–163 (1985).

[11] Kratschmer, W., Lamb, L., Fostiropoulos, K. & Huffman, D. Solid C_{60} - a New Form of Carbon. *Nature* **347,** 354–358 (1990).

[12] Khanna, S. & Jena, P. Assembling Crystals from Clusters. *Phys. Rev. Lett.* **69,** 1664–1667 (1992).

[13] Jena, P., Khanna, S.N., Physics of cluster assembled materials*, Materials Science and Engineering* A217/218, 218-222, (1996).

[14] Jena, P. Beyond the Periodic Table of Elements: The Role of Superatoms. *J. Phys. Chem. Lett.* **4,** 1432–1442 (2013).

[15] Rosch, N., Pacchioni, G. In Clusters and Colloids: From Theory to Applications, Schmid, G, Ed., VCH: Weinheim, Germany, 1994, p 5. See also references therein.

[16] Bein, Th., Jacobs, P. A., Schmidt, F. In Metal Microclusters in Zeolites, Jacobs, P. A., Ed., Elsevier: Amsterdam (1982).

[17] Brune, H., Giovannini, M., Bromann, K. & Kern, K. Self-organized growth of nanostructure arrays on strain-relief patterns. *Nature* **394,** 451–453 (1998).

[18] Rao, B., Jena, P., Manninen, M. & Nieminen, R. Spontaneous Fragmentation of Multiply Charged Metal-Clusters. *Phys. Rev. Lett.* **58,** 1188–1191 (1987).

[19] Lewis, G. N., The Atom and the Molecule. *J. Am. Chem. Soc*. **38**, 762–785 (1916).

[20] Langmuir, I., The Arrangement of Electrons in Atoms and Molecules. *J. Am. Chem. Soc*. 41, 868−934 (1919).

[21] Langmuir, I., Types of Valence. *Science* **54,** 59−67 (1921).

[22] Pyykko, P.; Runenberg, N., Icosahedral W@Au_{12}: A Predicted Closed Shell Species Stablized by Aurophilic Attraction and Relativity and in Accord with 18-Electron Rule. *Angew. Chem., Int. Ed*. **41**, 2174−2280 (2002).

[23] Li, X., Kiran, B., Li, J., Zhai, H. J., Wang, L. S., Experimental Observation and Confirmation of Icosahedral W@Au_{12} and Mo@Au_{12} Molecules. *Angew. Chem., Int. Ed.* **41**, 4786−4789 (2002).

[24] Wade, K., The Structural Significance of the Number of Skeletal Bonding Electron-Pairs in Carboranes, the Higher Boranes and Borane Anions, and Various Transition-Metal Carbonyl Cluster Compounds. *Chem. Commun.,* 792−793 (1971).

[25] Mingos, D. M. P. A General Theory for Cluster and Ring Compounds of the Main Group and Transition Elements. *Nature* **236,** 99−102 (1972).

[26] Ji, M. *et al.* Experimental and theoretical investigation of the electronic and geometrical structures of the Au_{32} cluster. *Angew. Chem.-Int. Edit.* **44,** 7119–7123 (2005).

[27] Xing, X., Yoon, B., Landman, U. & Parks, J. H. Structural evolution of Au nanoclusters: From planar to cage to tubular motifs. *Phys. Rev. B* **74,** 165423 (2006).

[28] Furche, F. *et al.* The structures of small gold cluster anions as determined by a combination of ion mobility measurements and density functional calculations. *J. Chem. Phys.* **117,** 6982–6990 (2002).

[29] Gruene, P. *et al.* Structures of neutral Au_7, Au_{19}, and Au_{20} clusters in the gas phase. *Science* **321,** 674–676 (2008).

[30] Castleman, A. W. & Jena, P. Clusters: A bridge between disciplines. *Proc. Natl. Acad. Sci. U. S. A.* **103,** 10552–10553 (2006).

[31] Jena, P. & Castleman, A. W. Clusters: A bridge across the disciplines of physics and chemistry. *Proc. Natl. Acad. Sci. U. S. A.* **103,** 10560–10569 (2006).

[32] Castleman, A. W. & Jena, P. Clusters: A bridge across the disciplines of environment, materials science, and biology. *Proc. Natl. Acad. Sci. U. S. A.* **103,** 10554–10559 (2006).

[33] Baerends, E. J., Ellis, D. E. & Ros, P. Self-consistent molecular Hartree-Fock-Slater calculations - I. The computational procedure. *Chem. Phys.* **2,** 41–51 (1973).

Chapter 2

THEORETICAL METHODS

This part of the dissertation provides a brief overview of the theoretical methods that have been used to study the systems of interest. A number of different methods and basis sets are employed. The Gaussian 03 and Gaussian 09 software have been used to perform the calculations using the super computers at VCU and Berkeley National Laboratory. The following sections begin with quantum chemical methods and thereafter density functional theory (DFT) is introduced.

2.1 The Schrodinger Equation

The chemistry of elements and compounds is guided by their electronic configuration. To have a theoretical understanding of the structure, stability and reactivity of chemical species, it is, therefore, important to calculate electronic properties. In 1926, Schrodinger proposed an equation, whose solution determines the exact energy of a system[1]. The time-independent non-relativistic Schrodinger equation is defined as an eigen-value problem of the form,

$$\hat{H}\,\Psi = E\,\Psi \qquad (2.1)$$

where $\hat{H}$ is the Hamiltonian operator that operates on Ψ, the wave function of the system and E is the energy eigenvalue. This is a second order differential equation, as will be seen from the description of $\hat{H}$.

In a system consisting of *N* electrons and *M* nuclei, the wave function of the i^{th} state of a system is represented by,

$$\Psi_i = \Psi_i \ (\vec{x}_1, \vec{x}_2, \ldots . \vec{x}_N, \vec{R}_1, \vec{R}_2, \ldots . \vec{R}_M \ ) \tag{2.2}$$

It is dependent on 3*N* spatial coordinates $\{\vec{r}_i\}$, and *N* spin coordinates $\{s_i\}$ of the electrons, which are collectively termed as $\vec{x}_i$, given by $\{\vec{x}_i\} = \{\vec{r}_i, s_i\}$ and 3*M* spatial coordinates of the nuclei, $\{\vec{R}_i\}$.

The Hamiltonian operator $\hat{H}$ is a differential operator that acts on the total wave function and can be written as[2],

$$H = -\frac{\hbar^2}{2m_e}\sum_{i=1}^{N}\nabla_i^2 - \frac{\hbar^2}{2M_A}\sum_{A=1}^{M}\nabla_A^2 - e^2\sum_{i=1}^{N}\sum_{A=1}^{M}\frac{Z_A}{r_{iA}} + e^2\sum_{i=1}^{N}\sum_{j>i}^{N}\frac{1}{r_{ij}} + e^2\sum_{A=1}^{M}\sum_{B>A}^{M}\frac{Z_A Z_B}{r_{AB}} \tag{2.3}$$

where *i* and *j* run over *N* electrons and *A* and *B* run over *M* nuclei. Z_A and Z_B are atomic numbers, M_A and m_e are the mass of nucleus and electron respectively, and $\hbar = \frac{h}{2\pi}$ where *h* is Planck's constant. r_{iA}, r_{ij} and r_{AB} are respectively the distance between the electron *i* and nuclei *A*, electron *i* and electron *j*, and nuclei A and nuclei B. The first two terms are the kinetic energy (T) of the electron and the nuclei respectively. The third term (potential energy term) represents attractive electrostatic interaction between the nuclei and electrons (V_{Ne}). The fourth and fifth terms are the potential energies due to electron–electron (V_{ee}) and nucleus–nucleus interaction,

respectively. Both terms are repulsive in nature. Here the Laplacian operator ∇_q^2 is defined as sum of differential operators given by,

$$\nabla_q^2 = \frac{\partial^2}{\partial x_q^2} + \frac{\partial^2}{\partial y_q^2} + \frac{\partial^2}{\partial z_q^2} \tag{2.4}$$

The ∇_i^2 and the ∇_A^2 are the analogous expressions for electron and nuclear coordinates *i* and A respectively.

It is a common practice to write these quantum mechanical equations using atomic units. This means that $\widehat{H}$ is written in terms of Hartree, all the lengths in terms of the Bohr radius, and M_A in terms of the electron mass M_e. The expressions for a Hartree (Ha) and a Bohr radius (a_0) are respectively, $\frac{\hbar^2}{m{a_0}^2} = \frac{e^2}{a_0} = 1$ Ha and $a_0 = \frac{\hbar^2}{me^2}$. Also the expressions for all distances and mass of the nucleus can be written as $r_{i,new} = \frac{r_{i,old}}{a_0}$ and $M_{A,new} = \frac{M_{A,old}}{m_e}$ respectively. We will not include the subscripts namely old and new in the later expression. Therefore, the Hamiltonian can now be written as,

$$\hat{H} = -\frac{1}{2}\sum_{i=1}^{N}\nabla_i^2 - \frac{1}{2}\sum_{A=1}^{M}\frac{1}{M_A}\nabla_A^2 - \sum_{i=1}^{N}\sum_{A=1}^{M}\frac{Z_A}{r_{iA}} + \sum_{i=1}^{N}\sum_{j>i}^{N}\frac{1}{r_{ij}} + \sum_{A=1}^{M}\sum_{B>A}^{M}\frac{Z_A Z_B}{r_{AB}} \tag{2.5}$$

The exact solution Ψ for the equation (2.5), however, has been a challenge to many. The equation is a partial differential equation in 4*N*+3*M* coordinates and therefore, impossible to solve analytically for systems with more than one electron. Even worse, systems of interest to chemists are mostly multi-atomic systems, where each atom has multiple electrons. Such studies are computationally expensive and require simplified approximation schemes. The Schrodinger equation can be simplified with the aid of several approximations, which are described below successively.

2.2 The Born-Oppenheimer Approximation

The major step toward simplifying the above problem is by the application of the Born–Oppenheimer approximation[3] or the clamped-nuclei approximation. This approximation is valid only when the ratio of electron to nuclear mass is considerably small. Therefore, the kinetic energy of the nucleus is assumed to be zero and the repulsive potential energy due to nucleus–nucleus interactions can be assumed to be almost constant. Then, the complete Hamiltonian given by equation (2.5) reduces to the so-called electronic Hamiltonian H_{ele} which is given by,

$$\hat{H}_{ele} = -\frac{1}{2}\sum_{i=1}^{N}\nabla_i^2 - \sum_{i=1}^{N}\sum_{A=1}^{M}\frac{Z_A}{r_{iA}} + \sum_{i=1}^{N}\sum_{j>i}^{N}\frac{1}{r_{ij}} = \hat{T} + \hat{V}_{Ne} + \hat{V}_{ee} \tag{2.6}$$

The attractive potential $\hat{V}_{Ne}$ is often termed as the external potential V_{ext} in density functional theory. Now, the main task in electronic structure calculation is reduced to solving the electronic Schrödinger equation given by,

$$\hat{H}_{ele}\psi_{ele} = E_{ele}\,\psi_{ele} \tag{2.7}$$

where $\psi_{ele} = \psi_{ele}(\vec{x}_1, \vec{x}_2, \ldots \vec{x}_N)$ (2.8)

As subsequent discussions will focus only on the electronic Schrodinger equation, the subscript '*ele*' is dropped hereafter. However, it can be exactly solved only for a single electron system. Approximations are required to solve multi-electron systems because of the complexity of the electron–electron interaction in the many-particle system.

2.3 The Hartree Approximation

In this approximation[4], the one–N electron problem is separated into N–one electron Schrödinger equations. Here the Hamiltonian of one of these has the form,

$$\hat{H} = \sum_{i=1}^{N} \hat{h}(i) \tag{2.9}$$

where *h(i)* is the operator describing the kinetic energy and potential energy of electron *i* and is defined as,

$$\hat{h}(i) = -\frac{1}{2}\sum_{i=1}^{N} \nabla_i^2 - \sum_{A=1}^{M} \frac{Z_A}{r_{iA}} + \sum_{j=1}^{N} \frac{1}{r_{ij}} \tag{2.10}$$

The wave function is a simple product of spin orbital wave functions for each electron and is defined as the Hartree product (HP) wave function. The Hartree product[5] wave function is given by,

$$\Psi^{HP}(x_1, x_2, \ldots, x_N) = \chi_1(\vec{x}_1)\chi_2(\vec{x}_2) \ldots \chi_N(\vec{x}_N) \tag{2.11}$$

where χ_i is a spin orbital *i* (a solution of one particle Schrodinger equation), x_i is position of electron *i*. The Hartree equation is an eigen-value equation of the form,

$$\hat{h}(i)\chi_i(\vec{x}_i) = \varepsilon_i \chi_i(\vec{x}_i) \tag{2.12}$$

The Schrödinger equation for the whole system is of the form,

$$H\psi^{HP} = E\psi^{HP} \tag{2.13}$$

Here the eigenvalue, *E* is the sum of the spin orbital energies of each of the spin orbitals appearing in ψ^{HP}

$$E = \varepsilon_i + \varepsilon_j + \ldots + \varepsilon_k \tag{2.14}$$

The Hartree method provides a great foundation for numerically approximating many body systems. However, it has some drawbacks. The important one is that the total wave function is not anti-symmetric under interchange of electron coordinates and doesn't obey the Pauli Exclusion Principle.

2.4 The Hartree-Fock Approximation

In the Hartree–Fock[5,6] approximation, the total wave function of the N-electron system is approximated by an anti-symmetrized product of *N* single-electron wave functions, $\chi_i(\vec{x}_j)$. This product is usually represented by a determinant called the *Slater determinant* Φ_{SD}[7]. Here, the correlated electron-electron repulsion is not specifically taken into account; only its average effect is included in the calculation. The Slater determinant is given by,

$$\psi_{SD}(\vec{x}_1,\vec{x}_2,\ldots\vec{x}_N)=\frac{1}{\sqrt{N!}}\begin{pmatrix}\chi_1(\vec{x}_1) & \chi_2(\vec{x}_1) & . & . & . & \chi_N(\vec{x}_1)\\ \chi_1(\vec{x}_2) & \chi_2(\vec{x}_2) & . & . & . & \chi_N(\vec{x}_2)\\ . & . & . & . & . & .\\ . & . & . & . & . & .\\ . & . & . & . & . & .\\ \chi_1(\vec{x}_N) & \chi_2(\vec{x}_N) & . & . & . & \chi_N(\vec{x}_N)\end{pmatrix} \tag{2.15}$$

Here $\frac{1}{\sqrt{N!}}$ is the normalization factor and $\chi_i(\vec{x}_j)$ is called the spin orbital of particle *i* as a function of position $\vec{x}_j$.

In the Hartree-Fock (HF) approximation, the anti-symmetric property of electrons is taken into account. $\psi(\vec{x}_1,\vec{x}_2)$ is anti-symmetric with respect to interchange of coordinates of electron 1 and 2,

$$\psi(\vec{x}_1,\vec{x}_2) = -\psi(\vec{x}_2,\vec{x}_1) \tag{2.16}$$

The Slater determinant obeys the Pauli Exclusion Principle. When two electrons are assigned to the same spin orbital, i.e. χ_1 and χ_2 are the same, then the determinant is zero.

The Hartree-Fock equation is an eigenvalue equation of the form,

$$f(i)\chi_j(\vec{x}_i) = \varepsilon_i\chi_j(\vec{x}_i) \qquad (i = 1,\ldots,N) \tag{2.17}$$

where the ε_i are the eigenvalues of the N number of equations, χ_j is the spin orbital j, and $f(i)$ is an effective one-electron operator, called the *Fock* operator, of the form,

$$f(i) = -\frac{1}{2}\nabla_i^2 - \sum_{A=1}^{M}\frac{Z_A}{r_{iA}} + v^{HF}(i) \tag{2.18}$$

where $v^{HF}(i)$ is the *Hartree-Fock potential* (the average repulsive potential experienced by the i^{th} electron due to the remaining $N-1$ electrons). Thus, the complicated two-electron repulsion operator $\frac{1}{r_{ij}}$ in the Hamiltonian is replaced by the simple one-electron operator $v^{HF}(i)$ where the electron-electron repulsion is taken into account only in an average way. $v^{HF}(i)$ has following two components,

$$v^{HF}(i) = \sum_j^N \left(J_j(\vec{x}_i) - K_j(\vec{x}_i)\right) \tag{2.19}$$

where J and K are Coulomb and exchange operators, respectively.

The total energy for the HF approximation is given as below,

$$E_{HF} = \sum_{i=1}^{N}\varepsilon_i - \frac{1}{2}\sum_{i=1}^{N}\sum_{j=1}^{N}(J_{ij} - K_{ij}) \tag{2.20}$$

where the Coulomb operator (due to a pair-wise Coulomb interaction between the i^{th} electron and the other electrons in all occupied spin orbitals) is given by,

$$J_{ij} = \langle ii|jj\rangle = \int d\vec{x}_i\, d\vec{x}_j \frac{|\chi_i(\vec{x}_i)|^2|\chi_j(\vec{x}_j)|^2}{r_{ij}} \tag{2.21}$$

And the exchange operator (due to the exchange of two variables within spin orbitals) is given by,

$$K_{ij} = \langle ij|ji\rangle = \int d\vec{x}_i \, d\vec{x}_j \frac{\chi_i^*(\vec{x}_i)\chi_j(\vec{x}_i)\chi_j^*(\vec{x}_j)\chi_i(\vec{x}_j)}{r_{ij}} \tag{2.22}$$

However, due to the Coulomb and Exchange terms appearing in the Hartree-Fock (HF) Hamiltonian, solving the Schrödinger equation involves calculating a large number of two-electron integrals. Hence, the HF method requires greater computational effort compared to that of the Hartree method. Moreover, the HF approximation doesn't take into account the short-range (*dynamical*) correlation between the electrons. This is due to the fact that the wave function ψ is represented as a rigid single *Slater determinant*, which makes the electrons interact with the average potential due to other electrons, instead of pair wise interactions. Hence, this method fails in describing the bond strengths, although it gives energies with an error of about 1 percent.

In order to include *dynamical correlation*, the many-body wave function is represented by a linear combination of *Slater determinants*. The Configuration Interaction (CI) or multi-configuration expansion method includes these multi-determinant wave functions. Many types of calculations begin with a Hartree–Fock calculation and subsequently correct for electron-electron repulsion, also referred to as electron-electron correlations. Møller–Plesset perturbation theory (MP_n) and coupled cluster theory (CC) are examples of these Post-Hartree–Fock methods. However, due to the large number of configurations required, it becomes computationally expensive to employ the Post Hartree-Fock methods for large systems. Hence, the application of these methods is usually limited to relatively small molecules/clusters where an accurate representation of the electron system is possible.

2.5 Density Functional Theory

There is significant computational expense associated with the Hartree-Fock method, as the wave function is dependent on 4N variables, three spatial variables and one spin variable for each of the N-electrons. The earliest formulation of density functional theory led to a simplification of this problem by expressing the energy as a functional of electron density, which depends only on three spatial co-ordinates.

2.5 .1 Thomas-Fermi-Dirac Approximation

The first attempt to use the electron density rather than the wave function for obtaining information about atomic and molecular systems was proposed by Thomas[8] and Fermi[9] in 1927. They showed that the kinetic energy of an electronic system E_{TF} can be expressed as a function of the electron density $\rho(\vec{r})$. Electrons were assumed to be non-interacting with a homogeneous gas density. The electron density is similar to the probability density and is given by,

$$\rho_i(\vec{r}_i) = \sum_{i=1}^{N} \int |\psi_i(\vec{r}_i)|^2 d\vec{r}_i \tag{2.23}$$

Where $\rho_i(\vec{r}_i)$ has the property

$$\sum_{i=1}^{N} \int \rho_i(\vec{r}_i) d\vec{r}_i = N \tag{2.24}$$

$\rho_i(\vec{r}_i)$ denotes the probability of finding the i^{th} electron out of N electrons at any point within a given volume $d\vec{r}_i$.

The Thomas-Fermi kinetic energy is then given by,

$$T_{TF}[\rho(\vec{r})] = \frac{3}{10}(3\pi^2)^{2/3} \int \rho^{5/3}(\vec{r}) d\vec{r} \tag{2.25}$$

If this kinetic energy is combined with the classical expression for the nuclear-electron attractive potential and the electron-electron repulsive potential, the resulting expression will give the total energy of an atom, given by,

$$E_{TF}[\rho(\vec{r})] = \frac{3}{10}(3\pi^2)^{2/3} \int \rho^{5/3}(\vec{r})d\vec{r} - Z\int \frac{\rho(\vec{r})}{r}d\vec{r} + \frac{1}{2}\iint \frac{\rho(\vec{r})\rho(\vec{r})}{r_{12}}d\vec{r}_1 d\vec{r}_2 \quad (2.26)$$

where the second term represents the attractive nucleus-electron Coulomb interaction and the third term represents the inter-electronic repulsion. It is to be noted that this expression does not account for the electron-electron exchange energy.

In 1930, Dirac[10] introduced an exchange term in the Thomas-Fermi energy given by,

$$K_D[\rho] = -\frac{3}{4}\left(\frac{3}{\pi}\right)^{1/3}\int[\rho(\vec{r})]^{4/3}\, d\vec{r} \quad (2.27)$$

and the resulting energy functional is therefore given by the Thomas-Fermi-Dirac approximation,

$$E_{TFD}[\rho(\vec{r})] = E_{TF}[\rho(\vec{r})] + K_D[\rho] \quad (2.28)$$

The importance of the Thomas-Fermi-Dirac approximation is that, it could express the kinetic energy as a functional of the electron density. Also it reduced the many-body problem involving 3*N* spatial co-ordinates to 3 spatial co-ordinates[11]. However, this method does not estimate the energies accurately. This drawback arises from assuming electrons to be uniformly distributed in space.

2.5.2 Hohenberg-Kohn Formulation

Density functional theory as we know it today was developed in 1964 and was based on two theorems proposed by Hohenberg and Kohn[12]. These theorems apply to a system consisting of electrons moving under the influence of an external potential $V_{ext}(\vec{r})$.

The first theorem states that:

"The external potential $V_{ext}\ (\vec{r})$ *is (to within a constant) a unique functional of* $\rho(\vec{r})$*; since, in turn* $V_{ext}\ (\vec{r})$ *fixes* $\widehat{H}$ *we see that the full many particle ground state is a unique functional of* $\rho(\vec{r})$*."*

The attractive potential $\hat{V}_{Ne}$ as mentioned in equation (2.6) of the Born–Oppenheimer approximation can be represented as the external potential $V_{ext}\ (\vec{r})$. According to this theorem, $V_{ext}\ (\vec{r})$ can be expressed in terms of the electron density $\rho(\vec{r})$. The authors proved that two different external potentials $V_{ext}\ (\vec{r})$ and $V'_{ext}\ (\vec{r})$ cannot result in the same $\rho(\vec{r})$. They further proposed that the kinetic energy of the electrons and the inter-electronic repulsion could also be expressed as functionals of $\rho(\vec{r})$. That is, by knowing the ground state density, the Hamiltonian of a many-electron system can be fully determined. Thus, the total energy as a functional of the electron density can be written as,

$$E[\rho] = T[\rho] + V_{ext}[\rho] + V_{ee}[\rho] \tag{2.29}$$

where the first term is the kinetic energy of the electrons, the second term is the external potential (*i.e.* the attraction between nuclei and electrons) and the third term is the inter-electronic repulsion. This inter-electronic repulsion $V_{ee}[\rho]$ can be written as a sum of the Coulomb electrostatic interaction and the non-classical exchange-correlation energy E_{XC} are given by,

$$V_{ee} = \frac{1}{2} \iint \frac{\rho(\vec{r}_1)\rho(\vec{r}_2)}{r_{12}} d\vec{r}_1 d\vec{r}_1 + E_{XC} \tag{2.30}$$

Equation (2.29) can be re-written as,

$$E[\rho] = F_{HK}\ [\rho] + \int \rho(\vec{r})\, V_{ext}\ (\vec{r}) d\vec{r} \tag{2.31}$$

where $F_{HK}[\rho] = T[\rho] + V_{ee}[\rho]$ (2.32)

It is to be noted that $F_{HK}[\rho]$ is independent of the external potential and is therefore a universal functional, identical for all systems.

The second Hohenberg-Kohn theorem applies to a variational theorem for calculating the ground state energy of a system as a functional of the electron density. It states that:

"The density that minimizes the energy functional is the exact ground state density".

Mathematically, the ground state energy can be obtained from,

$$E_0[\rho] = \min(F_{HK}[\rho] + \int \rho(\vec{r})\, V_{ext}\ (\vec{r}) d\vec{r}\ ) \tag{2.33}$$

It is to be noted that though the Hohenberg-Kohn theorems state that the kinetic energy and the Hamiltonian can be constructed from the electron density. However it does not tell us how to do this. Therefore, it is unclear from these theorems what the functional form of $F_{HK}[\rho]$ is. The Kohn-Sham equations published in 1965 address these issues.

2.5.3 Kohn-Sham Equations

The central assertion of the Kohn-Sham[13] scheme is that, for a particular ground state density $\rho(\vec{r})$ of a system of interacting particles, there exists a system of non-interacting particles. Calculations are performed on this fictitious system of non-interacting particles to yield the ground state total energy of the system of interest. The total wave function of the system is given by a Slater determinant of independent single electron orbitals, φ_i, called the Kohn-Sham orbitals. The electron density is given by

$$\rho = \sum_{i=1}^{N} |\varphi_i|^2 \tag{2.34}$$

where $\varphi_i = \varphi_i(\vec{r})$

The effective Hamiltonian for the system is given by,

$$\hat{H} = \left[-\frac{1}{2}\nabla^2 + \hat{V}_{eff}(\vec{r})\right] \tag{2.35}$$

The first term on the right hand side of this equation is the kinetic energy operator and the second term represents the "effective potential". The effective potential includes the effects from the external potential (i.e. the electron-nucleus interaction), the inter-electron Coulomb repulsion and the exchange-correlation potential. The Kohn-Sham wave functions therefore satisfy the equation,

$$\left[-\frac{1}{2}\nabla^2 + \hat{V}_{eff}(\vec{r})\right]\varphi_i = \epsilon_i\varphi_i \tag{2.36}$$

The total energy of the interacting system is given by,

$$E_{KS} = \mathrm{T}[\rho] + J[\rho] + E_{Ne}[\rho] + E_{XC}[\rho] \tag{2.37}$$

where the exact kinetic energy of the non-interacting system is given by,

$$T[\rho] = -\frac{1}{2}\sum_{i=1}^{N}\int \varphi_i^*(\vec{r})\nabla_i^2\varphi_i(\vec{r})d\vec{r} \tag{2.38}$$

The Coulomb repulsion can be expressed as,

$$J[\rho] = \frac{1}{2}\sum_{i=1}^{N}\sum_{j>i}^{N}\iint \frac{|\varphi_i(\vec{r}_1)|^2\ |\varphi_i(\vec{r}_2)|^2}{r_{12}}\ d\vec{r}_1 d\vec{r}_2 \tag{2.39}$$

The nucleus-electron interaction is given by,

$$E_{Ne}[\rho] = -\sum_{i=1}^{N}\int \sum_{A=1}^{M}\frac{Z_A}{r_{1A}}|\varphi_i(\vec{r}_1)|^2 d\vec{r}_1 \tag{2.40}$$

The Kohn-Sham equations are solved self-consistently. An initial density is first chosen and the effective potential is constructed. The solution yields a new initial density. This process is continued until the input and output densities are the same within the precision level desired. The importance of the Kohn-Sham method is that it converted the many-body problem into an independent particle problem. The exact kinetic energy of the system of non-interacting particles is first calculated and then the contributions from the inter-electronic interactions are estimated

as E_{XC}. It is important to note that the total energy only depends on the electron density $\rho(\vec{r})$, and except for E_{XC}, all components of the total energy have explicit functional forms. The approximations that have been made to construct the functional form of E_{XC} will be discussed in the next section. As will be shown, E_{XC} can be expressed approximately as a functional of $\rho(\vec{r})$.

2.5.4 Functionals for Exchange-Correlation

In density functional theory (DFT), the exchange correlation energy E_{XC} is expressed as a functional of the electron density. However, the exact form of exchange-correlation energy (E_{XC}) is difficult to obtain. Hence, in DFT, one uses an approximate form for E_{XC}, which can be treated in two parts; one term dealing with the exchange energy E_X, and the other term dealing with the correlation energy E_C. Therefore, E_{XC} can be expressed as:

$$E_{XC}[\rho(\vec{r})] = E_X[\rho(\vec{r})] + E_C[\rho(\vec{r})] \tag{2.41}$$

where E_X is the exchange energy of the Slater determinant of Kohn-Sham orbital and E_C is the correlation energy. It should be emphasized that the exchange energy is usually numerically larger than the corresponding correlation energy.

2.5.4.1 Local Density Approximation (LDA)

This is the first approximation made to E_{XC}. It is based on the homogenous electron gas. In this approximation, the electron density is assumed to be a slowly varying function of $\vec{r}$. The exchange energy, E_X in the LDA approximation is defined as,

$$E_X^{LDA} = \int \rho(\vec{r})\epsilon_x \, d\vec{r} = -\frac{3}{4}\left(\frac{3}{\pi}\right)^{1/3} \int [\rho(\vec{r})]^{4/3} \, d\vec{r} \tag{2.42}$$

where ϵ_x is the exchange energy per particle and is given by,

$$\epsilon_x = -\frac{3}{4}\left(\frac{3}{\pi}\right)^{1/3}[\rho(\vec{r})]^{1/3} \tag{2.43}$$

There is no such explicit expression for the correlation part E_C. Various authors have presented analytical expression for ϵ_C. One of the most widely prevalent LDA functionals used for ϵ_C is given by Vosko, Wilk and Nusair, and referred to as the VWN potential[14].

This functional is called a local approximation because it depends only on the density of the coordinate where the functional is evaluated. The LDA is a moderately-accurate approximation. The advantage of the LDA method is that, it is relatively simple and computationally inexpensive. The main disadvantages, on the other hand, are that this method overestimates bonding and underestimates equilibrium volume as well as band gap. Also, the functional cannot describe reaction barriers or calculate total energies correctly. This arises from the issue that the LDA method underestimates the exchange energy by about 10% and overestimates the correlation energy to be double the actual value.

2.5.4.2 Generalized Gradient Approximation (GGA)

The LDA method approximates the energy of the true density by the energy of a local constant density. Therefore, in situations where the density $\rho(\vec{r})$ varies rapidly with $\vec{r}$ (such as in molecules), the true energy of the system is poorly represented. To overcome the limitation of LDA, the Generalized Gradient Approximation (GGA) is used. In GGA, the functionals are dependent on both the density ρ and its gradient $\nabla\rho$.

The gradient-corrected functional is of the form,

$$E_{XC}^{GGA} = E_{XC}[\rho(\vec{r}), \nabla\rho(\vec{r})] \quad (2.44)$$

There are several functionals that are used for GGA exchange and correlation. Examples include the B88 functional for exchange[15], the LYP functional for correlation and the PW91 functional for exchange and correlation[16]. The gradient-corrected exchange functional proposed by Becke in 1988 termed as B88 is given as,

$$E_X^{B88} = E_X^{LDA} + \Delta E_X^{B88} \quad (2.45)$$

$$\text{where } \Delta E_X^{B88} = -\beta\rho^{1/3} \frac{x^2}{1+6\beta x \sinh^{-1} x} \quad (2.46)$$

The parameter β is determined from atomic data, and x is defined as:

$$x = \frac{|\nabla\rho|}{\rho^{4/3}} \quad (2.47)$$

These functionals go beyond local in order to account for the non-homogeneity of the real density. However, describing GGA as non-local is not correct. In a mathematical sense, the GGA functional are perfectly local: the values of the functional at a point $\vec{r}$ depend only on density $\rho(\vec{r})$ and its gradient $\nabla\rho(\vec{r})$.

2.5.4.3 The Hybrid GGA Functional

In 1993, Becke[17] proposed a gradient-corrected exchange functional which is a combination of both the exact HF exchange and DFT exchange energies; hence this functional is termed as a hybrid functional. The 3-parameter exchange functional, together with the correlation functional proposed by Lee, Yang and Parr[18] is called the B3LYP and is mathematically expressed as,

$$E_{XC}^{B3LYP} = E_X^{LDA} + a_0(E_x^{HF} - E_x^{LDA}) + a_X\Delta E_X^{B88} + E_C^{VWN} + a_C(E_C^{LYP} - E_C^{VWN}) \quad (2.48)$$

Here, a_0 = 0.20, a_X = 0.72 and a_C = 0.81 are semi-empirical coefficients, determined by fitting to experimental data.

As can be seen, the B3LYP functional is a combination of the LDA exchange, the HF exchange, and Becke's gradient corrected exchange with the Lee-Yang-Parr gradient corrected correlation functionals. It is important to point out that, though hybrid functionals partially account for the electron-electron self-interaction term, effects of this non-physical term are not totally canceled in density functional theory.

2.5.4.4 The Hybrid meta-GGA Functional

Meta-GGA DFT functional in its original form includes the second derivative of the electron density (the Laplacian). These functionals incorporate a further term in the expansion, depending on the density, the gradient of the density and the Laplacian (second derivative) of the density.

Many density functionals are unable to treat the polarizability of conjugated systems[19]. This failure may be attributed to an incorrect long range behavior of the effective potentials generated by the density functionals that have been popularly used [21]. This incorrect long-range behavior results from a self-interaction error in local DFT exchange[21]. One way to correct the long-range errors in DFT effective potentials is to mix Hartree-Fock exchange with DFT correlation. This will not only eliminate the long-range self-interaction error but also give an overall average performance as good as or better than B3LYP.

One of the meta-hybrid GGA DFT functionals that have been developed recently are a set of four M06 suite of functionals[20, 21]. The family includes the functionals M06-L, M06, M06-2X

and M06-HF, with a different amount of exact exchange in each. For example, M06-L is fully local without HF exchange (thus it cannot be considered hybrid), M06 has 27% of HF exchange, M06-2X 54% of HF exchange and M06-HF 100% of HF exchange. The M06-L functional is good for transition metals, inorganic and organometallic systems, whereas M06, M06-2X and M06-HF functionals are the best for the study of organometallics and non-covalently interacting systems. This suite includes dispersion forces, improving one of the biggest deficiencies in DFT methods.

2.6 Basis sets

A basis set is a set of functions which are combined in linear combinations to create molecular orbitals. These functions are typically atomic orbitals centered on atoms, but can theoretically be any function. The molecular orbitals Ψ_i, which are represented as a Linear Combination of Atomic Orbitals (LCAO) is given as,

$$\psi_i = \sum_{\mu=1}^{N} C_{\mu i}\, \chi_\mu \tag{2.49}$$

where $C_{\mu i}$ are molecular orbital expansion coefficients, χ_μ is the μ-th orbital and N is number of atomic orbitals. There are two types of basis functions commonly used in electronic structure calculations. They are *Slater Type Orbitals (STOs)*[22] and *Gausssian Type Orbitals (GTOs)*[23]. The Slater Type Orbitals decay exponentially with increasing distance from the nucleus and are given by,

$$\chi(r,\theta,\varphi) = Nr^{n-1}e^{-\xi r}Y_{l,m}(\theta,\varphi) \tag{2.50}$$

where N is the normalization constant, ξ is called "Slater orbital exponent". (r,θ,φ) are spherical coordinates and $Y_{l,m}$ are the conventional spherical harmonics. Slater basis functions

resemble the true atomic orbitals more closely than Gaussian basis functions, displaying the correct nuclear cusp and asymptotic decay. This leads to a more accurate and more intuitive description of the molecular orbitals at the same size of basis set. However, these require calculation of 3 or 4 centered electron integrals in SCF calculations, which is computationally expensive. Therefore, STOs are used mainly for atomic and linear systems.

It was realized by Frank Boys[24] that STOs can be represented as a linear combination of Gaussian orbitals. Since it is relatively easier to calculate integrals (such as overlap integral and so on) using Gaussian orbitals, GTOs are widely used today. GTOs can be expressed as,

$$\chi(x,y,z) = Nx^{l_x}y^{l_y}z^{l_z}e^{-\xi r^2} \tag{2.51}$$

where l_x , l_y and l_z determine the angular part of orbital and ξ represents the radial part of the function. The use of *Gaussian-Type orbitals (GTOs)* reduces the computational cost but has some drawbacks. The e^{-r^2} dependence, results in a zero slope at the nucleus, instead of a cusp.

In general, it takes about three times as many GTOs as STOs to achieve a particular degree of accuracy. Therefore, a number of GTOs are combined to form one contracted Gaussian function (CGF). The simplest basis sets have only one basis function (or one contracted function in case of CGF) to represent each atomic orbital and are therefore called minimal basis sets. One of the most widely used minimal basis sets is the STO-*n*G basis set which is constructed by a linear combination of *n* primitive GTO functions[25]. For example, the STO-3G basis set is made of 3 GTO functions. In higher basis sets, called double-zeta basis sets, two functions are used for each atomic orbital. Now, given that only the valence electrons are involved in bonding, the core electrons can be treated by minimal basis sets while the valence electrons can be represented by double/triple/quadruple zeta basis sets. Basis sets of this kind, developed by Pople and coworkers, are called split valence basis sets[26, 27]. They are represented as X-YZG (for double

zeta basis sets). This means that X primitive GTOs are used to represent each of the core electrons, and the outer electrons are each represented by two basis functions, each consisting of Z and Y primitive GTOs, respectively. For example, in the 6-311G basis, 6 primitive GTOs make up each of the core orbitals, and the valence orbitals are represented by 3 basis functions, each of which is composed of 3, 1, and 1 Gaussian functions, respectively. Polarization functions (represented as *) and diffuse functions (represented as +) are added to improve basis sets. The former allows flexibility for atoms to form chemical bonds, while the latter helps to improve the predicted properties of systems with diffuse electron density such as anions.

The inert core electrons of atoms heavier than krypton (such as gold) are often modeled by an effective core potential (ECP) called pseudopotential. The pseudopotential is an effective potential constructed to replace the atomic all-electron potential such that core states are eliminated and the valence electrons are described by pseudo-wavefunctions with significantly fewer nodes. The pseudopotential is called relativistic if relativistic effects have been incorporated into it. For example, the Stuttgart pseudopotential (SDD) is a common relativistic pseudopotential used for gold[28, 29].

2.7 Computational Methodology

This section describes the computational details of each of the systems studied in the following chapters. In all the work, structural, electronic and spectroscopic properties of clusters have been studied using density functional theory (DFT). Also in some cases the calculations are repeated using *ab-initio* quantum chemistry methods. The basis sets that represent the atomic orbitals have been chosen to be optimal for the system under investigation. The choice of the level of theory was based on earlier literature available for similar systems that gave reliable

results and that matches well with experiments. A good agreement between theory and experiment will not only validate the approach being used, but, equally important, will also provide information on the cluster geometry that can only be achieved, at present, from theoretical studies.

In Chapter 3, we used density functional theory (DFT) and Becke's 3 parameter hybrid functional for exchange and Lee-Yang-Parr functional for correlation (B3LYP)[30,31]. In section 3.1 of this chapter, we have also repeated some of the calculations for the smaller clusters using the coupled-cluster method with singles and doubles and non-iterative inclusion of triples (CCSD(T)) in order to validate the accuracy of DFT-B3LYP for these systems. For these studies the geometries optimized at the DFT-B3LYP level were used. We have used 6-311++G** basis functions for Li, Mg, Al, N and O for all the calculations. We have also repeated few of our calculations for the smaller clusters with different basis functions, namely, 6-311++G(3df) in order to see how sensitive the results are to changing basis functions. The results at different levels of theory are presented in Table 3-1 of chapter 3 for a number of clusters. We note that, with the exception of NO, these results agree with each other and with experiment within 0.3 eV. This sets the accuracy level of our computed results. In section 3.2, we used the basis set 6-311++G(2d) for Li, Be, B, N, O, F, Cl, and SDD[32] for Cs. The basis sets used in section 3.3 are the Stuttgart pseudo potential (SDD)[32] basis functions for Pd and Zr atoms, whereas triple- ζ valence plus polarization (TZVP) basis functions are used for O, C, and H atoms. These basis sets, along with DFT-B3LYP, have been found to predict accurately the ground state, spin multiplicity, and reaction energies of clusters composed of these elements[33,34,35].

In Chapter 4, we also use the DFT-B3LYP method, along with different basis sets, such as the 6-311++G(3d), the Stuttgart pseudo potential (SDD)[32] and the 6-311++G for Cu, Ag, and

H, respectively. The computational details of section 5.1.1 and 5.1.2 will be discussed in Chapter 5.

In all cases, several initial structures were optimized to find the ground state geometry and calculate the corresponding total energy. We also determined the ground state spin multiplicities by calculating the total energies for allowable spins, *e.g.* doublet and quartet for odd-electron systems and singlet and triplet for even-electron systems. Optimizations have been carried out without any symmetry constraint. The dynamical stability of the clusters was confirmed by carrying out frequency calculations, which were all found to be positive. In addition, Natural Bond Orbital (NBO) analysis was performed to give an indication of the nature of bonding involved in the clusters. We used the default optimization algorithm included in Gaussian (*i.e.* the Berny algorithm) to obtain the lowest energy geometry[36]. The SCF convergence threshold for all runs was set at a total energy change of 1×10^{-6} (atomic unit) a.u, while geometry optimization convergence criteria were 0.45×10^{-3}, 0.3×10^{-3}, 1.8×10^{-3} and 1.2×10^{-3} a.u. for maximum force, RMS force, maximum displacement and RMS displacement, respectively. The calculated energies were utilized to compute the parameters such as vertical detachment energy (VDE), the adiabatic detachment energy (ADE), the electron affinity (EA), vertical ionization potential (IP), hardness (η), HOMO-LUMO gap, and binding energy (E_b) of clusters. VDE is computed as the energy difference between the optimized structure of the anion, and the neutral at the anion geometry. The ADE is given by the energy difference between the optimized structure of the anion and that of its structurally similar neutral. The EA, on the other hand is the difference in the energy between the ground states of the anion and the neutral cluster. The EA and ADE values are the same when the ground state geometries of the anion and neutral cluster are about the same. The VDE is always larger than the ADE and EA, as the

neutral cluster is not allowed to relax. If the difference between the VDE and EA are nearly the same, it indicates that the geometry of the anion does not relax as the extra electron is removed, and if not, then the geometry of the neutral cluster is assumed to be protected by a significant energy barrier. Due to the presence of such barrier, it is difficult to determine the EA of a cluster experimentally. Vertical ionization potentials (IP), on the other hand are calculated as the energy difference between neutral clusters and their cations at the neutral ground state geometry. The parameter hardness (η) is given by (IP-EA). The definition for the binding energy is mentioned in the respective chapters based on the systems studied. One can compare between experimental and theoretical results by considering the threshold energies and the vertical detachment energies obtained from the experimental data. The threshold energy is determined by fitting the signal increase at low binding energy to a linear function whose intersection with the zero axes is taken as the threshold energy and the VDE is taken as the binding energy of the first maximum at the lowest binding energy. When the optimized geometry of neutral and anion are similar, the threshold energy can be compared to the calculated EA. If the geometries are very different the threshold energy is compared to the calculated ADE. All calculations were performed using the Gaussian 03 and Gaussian 09 softwares[37, 38] . The output symmetries were kept at a tolerance of 0.1 using Gaussview.

References

[1] Schrodinger, E. An Undulatory Theory of the Mechanics of Atoms and Molecules. *Phys. Rev.* **28**, 1049-1070 (1926).

[2] Koch, W., Holthausen, M. C., A Chemist's Guide to Density Functional Theory, Weinheim, New York : Wiley-VCH; 2001.

[3] Born, M., Oppenheimer, J. R. *Ann. Physik*. **41**, 457-484 (1927).

[4] Hartree, D. R. *Proc. Cambridge Phil. Soc*. **24**, 89, (1928).

[5] Szabo, A., Ostlund, N. S., Modern Quantum Chemistry: Introduction to Advanced Electronic Structure Theory; Macmillan, New York; 1982.

[6] Fock, V. *Z. Physik.* **48**, 73 (1928).

[7] Slater, J. C. *Phys. Rev.* **81**, 385 (1951).

[8] Thomas, L. H. *Proc. Cambridge. Philos. Soc.* **23**, 542-548 (1927).

[9] Fermi, E. *Rend. Accad. Naz. Lincei*. **6**, 602-607 (1927).

[10] Dirac, P. A. M. *Proc. Cambridge. Philos. Soc.* **26**, 376-385 (1930).

[11] Ashcroft, N. W. and Mermin, N. D. *Solid State Physics* (Holt, Rinehart and Winston, 1976).

[12] Hohenberg, P., Kohn, W. *Phys. Rev.* **136**, B864-B871 (1964).

[13] Kohn, W., Sham, L. J. *Phys. Rev.* **1965**, *140*, A1133-A1138.

[14] Vosko, S. J., Wilk, L., Nusair, M. *Can. J. Phys.* **58**, 1200-1211 (1980).

[15] Becke, A. D. *Phys. Rev. A*, **38**, 3098-3100, (1988).

[16] Perdew, J. P., Wang, W. *Phys. Rev. B*, **45**, 13244-13249 (1992).

[17] Becke, A. D. *J. Chem. Phys.* **98**, 5648-5652 (1993).

[18] Lee, C. T., Yang, W. T., Parr, R. G. *Phys. Rev. B*, **37**, 785-789 (1988).

[19] Champagne, B., Perpete, E. A., van Gisbergen, S. J. A., Baerends, E.-J., Snijders, J. G., Soubra-Ghaoui, C., Robins, K. A., Kirtman, B. *J. Chem. Phys.* **109**, 10489 (1998).

[20]Zhao, Y., Truhlar, D. G. *Theor. Chem. Acc.* **120**, 215–241 (2008).

[21] Zhao, Y.; Truhlar, D. G. *J. Phys. Chem. A*, **110**, 13126–13130 (2006).

[22] Slater, J. C. *Phys. Rev.* **36**, 57-64, (1930).

[23] Gill, P. M. W. *Adv. Quantum Chem.* **25**, 141-205 (1994).

[24] Boys, S. F. *Proc. R. Soc. (London) A.* **200**, 542 (1950).

[25] Hehre, W. J., Stewart, R. F., Pople, J. A. *J. Chem. Phys.* **51**, 2657-2664, (1969).

[26] Krishnan, R., Binkley, J. S., Seeger, R., Pople, J. A. *J. Chem. Phys.* **72**, 650-654 (1980).

[27] Mclean, A. D., Chandler, G. S. *J. Chem. Phys.* **72**, 5639-5648 (1980).

[28] Schwerdtfeger, P., Dolg, M., Schwarz, W. H. E., Bowmaker, G. A., Boyd, P. D. W. *J. Chem. Phys.* **91**, 1762-1774 (1989).

[29] Dolg, M., Wedig, U., Stoll, H., Preuss, H. *J. Chem. Phys.* **86**, 866-872 (1987).

[30] Becke, A. *J. Chem. Phys.* **98**, 5648 (1993).

[31] Lee, C., Yang, W., and Parr, R. *Phys. Rev. B.* **37**, 785 (1988).

[32] Dolg, M., Stoll, H., Preuss, H., and Pitzer, R., *J. Phys. Chem*. **97**, 5852 (1993).

[33] Cui, Q., Musaev, D.G., and Morokuma, K., *J. Chem. Phys*. **108**, 8418 (1998).

[34] Moc, J., Musaev, D.G., and Morokuma, K., *J. Phys. Chem. A* **104**, 11606 (2000).

[35] Johnson, G.E., Mitric, R., Tyo, E.C., Bonacic-Koutecky, V. and Castleman, A.W., *J. Am. Chem. Soc.* **130**, 13912 (2008).

[36] Frisch, M.J., Trucks, G.W., Schlegel, H.B., Scuseria, G.E., Robb, M.A., Cheeseman, J.R., Montgomery, J.A., Vreven, T., Kudin, K.N., Burant, J.C., Millam, J.M., Iyengar, S.S., Tomasi, J., Barone, V., Mennucci, B., Cossi, M., Scalmani, G., Rega, N., Petersson, G.A., Nakatsuji, H., Hada, M., Ehara, M., Toyota, Fukuda, R., Hasegawa, J., Ishida, M., Nakajima, T., Honda, Y., Kitao, O., Nakai, H., Klene, M., Li, X., Knox, J.E., Hratchian, H.P., Cross, J.B., Adamo, C., Jaramillo, J. , Gomperts, R., Stratmann, R.E., Yazyev, O., Austin, A.J., Cammi, R., Pomelli, C., Ochterski, J.W. , Ayala, P.Y., Morokuma, K., Voth, G.A., Salvador, P., Dannenberg, J.J., Zakrzewski, V.G., Dapprich, S., Daniels, A.D., Strain, M.C., Farkas, O., Malick, D.K., Rabuck, A.D., Raghavachari, K., Foresman, J.B., Ortiz, J.V., Cui, Q., Baboul, A.G., Clifford, S., Cioslowski, J., Stefanov, B.B., Liu, G., Liashenko, A., Piskorz, P., Komaromi, I., Martin, R.L., Fox, D.J., Keith, T., Al-Laham, M.A., Peng, C.Y., Nanayakkara, A., Challacombe, M., Gill,

P.M.W., Johnson, B., Chen, W., Wong, M.W., Gonzalez, C., Pople, J.A. *Gaussian 03, Revision B.01*, Gaussian, Inc., Pittsburgh, PA (2003).

[37] Frish, M. J. *et al*. Gaussian 03, Revision D.02, Gaussian, Inc., Wallingford CT, 2004.

[38] Frish, M. J. *et al*. Gaussian 09, Revision B.01, Gaussian, Inc., Wallingford CT, 2010.

Chapter 3

CLUSTERS AS SUPERATOMS

Atomic clusters with specific size and composition can be designed to mimic the chemistry of elements in the periodic table. This idea was put forth more than twenty years ago by Khanna and Jena[1], who termed such clusters as "superatoms". They suggested that superatoms can be regarded as *man-made* elements belonging to the third-dimension of a new three-dimensional periodic table. Just as conventional crystals are formed with atoms as the building blocks, one can imagine that a novel class of cluster-assembled materials can be formed with stable superatoms as the building blocks. This possibility was demonstrated first by focusing on the Al_{13} cluster. With 39 electrons, Al_{13} has an electronic configuration of $1S^2\ 1P^6\ 1D^{10}\ 2S^2\ 1F^{14}\ 2P^5$ in the jellium model[2] and requires only one electron to satisfy the electronic shell closure rule, just as Cl with an electronic configuration of $ns^2\ np^5$ requires a single electron to fulfill the octet-rule. The intense peak of the Al_{13}^- anion in the mass spectra and its inertness towards oxygen, observed by Castleman and coworkers[3] provided evidence for its unusual stability. Thus, it was hypothesized that Al_{13} can mimic the chemistry of a Cl atom. Li *et al*[4], later measured the electron affinity (EA) of Al_{13} to be 3.62 eV, which is nearly identical with that of Cl, namely, 3.61 eV. With a metal cation like K^+, Khanna and Jena[5] then predicted that Al_{13}^-

can form the anionic component of a cluster-salt, namely KAl_{13}. This prediction[5] was later confirmed by Zheng *et al*[6] who showed through photodetachment spectroscopy experiment that Al_{13} can indeed form a salt-like ionic molecule when interacting with an alkali metal, namely KAl_{13}, just as Cl does, namely KCl. Likewise, it has been found that, the Al_7^- cluster exhibits valence, of 2 and 4, which makes it analogous to C or Si and can be classified as a multiple valence superatom[7]. An Al_{14} cluster behaves like an alkaline earth atom when combined with iodine atoms to form $Al_{14}I_x^-$ cluster compounds, and hence can be regarded as a superalkaline earth atom[8]. There has been a considerable activity on superatoms5[, 9, 10, 11,12, 13,14]. The validity of the superatom concept is not confined to Al clusters. The characteristics of As_7^{3-} and As_{11}^{3-} have been found to be analogous to phosphorous atom and K_3O to alkali metals[15]. It has been shown in a recent report by Jadzinsky *et al*[16] that the Au_{102} cluster serves as building block of a nanoscale material. The stability of the Au_{102} motifs can be understood within a superatom concept by considering the outer 44 Au atoms to be linked to thiols, while the core of 58 remaining Au atoms corresponding to a closed electronic shell.

In the past decade considerable research has been carried out to design and synthesize superatoms using a variety of electron counting rules such as the octet rule[17], the 18-electron rule[18], and the Wade-Mingos rule[19], in addition to the jellium rule discussed in the above. A few cluster assembled materials have also been synthesized[20, 21].

In this chapter, we will discuss three different types of superatoms: 1) Clusters whose properties not only mimic halogen atoms but also have the ability, far greater than those of halogens, to attract an electron, 2) Clusters whose properties mimic the properties of alkalis and have the ability to lose an electron more easily the alkali metal atoms, and 3) A cluster that mimics the chemistry of a catalyst. The latter group of cluster consists of a transition metal

oxide, where here ZrO is studied. Its properties were found to represent that of Pd, a known catalyst. The first and second group of clusters belongs to a special class of superatoms and is known as "superhalogens" and "superalkalis", respectively. The former classes of clusters are strong oxidizing agents and serve as weekly coordinating anions. The later, however, have excellent reducing properties and form unusual charge-transfer salts when interacting with species with low electron affinity. These three types of superatoms are explained in details in sections 3.1, 3.2 and 3.3 respectively.

3.1 Clusters mimicking properties of halogens: '*Superhalogens*'

3.1.1 Introduction

Superhalogens are a class of highly electronegative molecules whose electron affinities (EAs) are much higher than those of halogens. Half of a century ago, Bartlett and co-workers were the first to show that PtF_6 can ionize an O_2 molecule or a Xe atom[22,23] and estimated its EA to be 6.8 eV. Gutsev and Boldyrev later generalized this finding and showed that a superhalogen can be represented by the formula $MX_{(k+1)/n}$ [17], where M is the central metal atom with maximal formal valence of k , and X is the electronegative atom with valence n. Conventional superhalogens consist of halogen atoms as ligands. The reason for their large electron affinity is that such a system is one electron short of attaining electronic shell closure. Once the extra electron is added, it becomes delocalized over (k + 1) halogens and greatly stabilizes the cluster. Consequently, the EA of such a molecular system is larger than that of the constituent halogen atoms, rendering its superhalogen properties. Using photoelectron spectroscopy, Wang *et al*[24] were the first to experimentally confirm the high EAs of superhalogens.

Over the years, many more kinds of superhalogens have been studied. Examples include metal-free superhalogens (such as H_nF_{n+1}[25]), polynuclear superhalogens (such as M_nX_{nk+1}[26,27]), halogen-free superhalogens where the halogens are replaced by O[28, 29], H[30], OH[31], CN[32], NCO[32], and electrophiles (such as COOH[33]). Moreover, species completely devoid of both metal and halogen atoms (such as BO_2[34], $B_{12}H_{13}$[35], $CB_{11}H_{12}$[35]) have also been found to exhibit superhalogen behavior.

The most important application of superhalogens is that they can be used as building blocks of unusual salts when combined with alkali cations. These salts are dubbed as "supersalts". A common example of such a salt is $KMnO_4$, where the anionic part, *i.e.* MnO_4 is a superhalogen, having an EA of 4.80 eV. $KMnO_4$ is widely used as a cleaning agent, and in organic chemistry, oxidizes alcohols into acids. Moreover, suitable superhalogens are also capable of forming strongly bound ionic compounds even when combined with closed-shell molecules such as NH_3, SiO_2, and H_2O, which have large ionization potentials[36,37]. One can also imagine synthesizing supersalts using superalkali as cations in place of normal alkali atoms and superhalogens as anions in place of halogens. Design of such salts is discussed in more detail in section 3.2.

In a recent study, it has been shown that a new class of species, called "hyperhalogens"[38], which are composed of a metal atom at the core and surrounded by superhalogen moieties can be created. Such species are represented by the formula MY_{m+1}, where M is a metal with valence *m* and Y is a superhalogen. This is another class of highly electronegative species whose EAs are even higher than that of their constituent superhalogens, thus providing a pathway to create strong negative ions. This discovery was made while systematically studying the interaction of BO_2 with Au atom. The EA of $Au(BO_2)_2$ was found to be significantly larger than that of BO_2 by

1.24 eV[39]. We note that BO_2 is a superhalogen with an electron affinity of 4.46 eV. Later studies[40,41] have shown that the electron affinity of $Cu(BO_2)_2$ and $Ag(BO_2)_2$ are also higher than that of BO_2, thus confirming the hyperhalogen concept. Hyperhalogens, when counter balanced by suitable cations can lead to the formation of a new class of salt known as "hypersalts". One such salt, namely $KAl(BH_4)_4$, has been recently synthesized[20], which is found to be very stable and exhibits unique properties. Aluminum borohydride, $Al(BH_4)_3$, is an ionic liquid which is highly volatile and pyrophoric under ambient conditions[42]. The EA of the ligand BH_4 is 3.18 eV and can act as a pseudo-superhalogen when paired with a metal cation such as Al. The metal Al is trivalent and when four BH_4 is added, it results in the formation of hyperhalogen $Al(BH_4)_4$, whose EA is even higher than that of its ligand BH_4 [43]. When this hyperhalogen is counter balanced by a cation such as K, it results in the formation of a complex, $KAl(BH_4)_4$, which is a hypersalt. This salt was found to be a stable solid at room temperature[20].

In the following section, we explore the superhalogen properties of the nitrate radical and test its potential to form hyperhalogens and hypersalts. One of the major applications of nitrates is as strong oxidizing agents, most notably in explosives. When they react with appropriate fuels, they produce a large amount of energy. Analogous to BO_2, which is known to be a superhalogen[34], NO_3 contains neither a metal atom nor a halogen atom. Therefore, all known nitrate salts including KNO_3, $Mg(NO_3)_2$, $Ca(NO_3)_2$, $NaNO_3$, and so forth, can be classified as "supersalts". Our objective is to see if the nitrate content of salts could be further increased by first designing hyperhalogens using NO_3 and then making the corresponding hypersalts. To analyze this, we first conducted a systematic study of nitrogen oxides NO_x, where $x = 1-3$. Next, we studied $M(NO_3)_x$, where M = Li, Mg, and Al and $x = 1-2$ for Li, $x = 1-3$ for Mg, and $x = 1-4$ for Al. By analogy, $Li(NO_3)_2$, $Mg(NO_3)_3$, and $Al(NO_3)_4$ should all be hyperhalogens, and

therefore, by adding an alkali metal K, $KLi(NO_3)_2$, $KMg(NO_3)_3$, and $KAl(NO_3)_4$ should yield hypersalts. The details on computational methodology for this study are given in section 2.9 of Chapter 2. The results and discussions are provided in the following section 3.1.2, followed by conclusions in section 3.1.3.

3.1.2 Results and Discussions

3.1.2.1 *Onset of Superhalogen Behavior in Nitrogen Oxides NO_x (where x = 1−3):*

In Figure 3-1, the optimized structures of neutral and anionic NO_x are shown. Their VDEs and ADEs are given in Table 3-1.

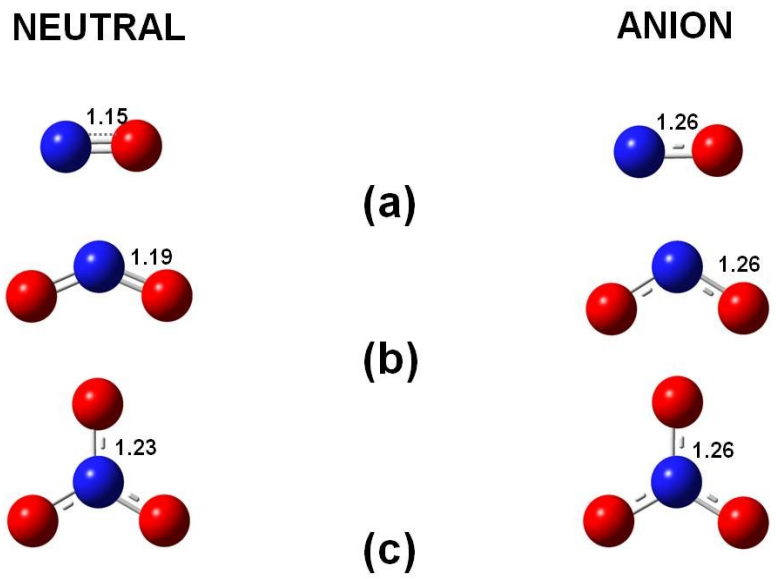

Figure 3-1: Optimized geometry of neutral and anionic NO_x (x = 1−3).

We find that both NO and NO_2 have quite low EAs (ADEs). Because N has a valence of 3 and O has a valence of 2, NO_2 formally requires only one electron to close its electronic shell. Despite this, its ADE is smaller than that of a halogen atom. A likely explanation for this unexpected behavior is as follows: The inter-electronic repulsion, once the extra electron is

added to NO_2, is exacerbated by the presence of the lone pair of electrons on N. Due to the small size, this effect could not be overcome by resonance. However, in NO_3, the optimal size is reached, and therefore, the stability gained by adding the extra electron overshadows the inter-electronic repulsion and hence, the emergence of superhalogen behavior of NO_3. It was found that the experimental value of the ADE of NO_2 varies from 1.8 to 3.9 eV, depending upon different experimental techniques such as laser photo detachment (LPD), laser photoelectron spectroscopy (LPES), ion/molecule reaction bracketing (IMRB), and so forth [46, 47,48, 44].

Table 3-1: Electron Detachment Energies of NO_x (x = 1−3) and MNO_3 (where M = Li, Mg, Al).

Cluster	**Expt ADE(eV)**	**B3LYP/6-311++G****		**CCSD(T)/6-311++G****		**B3LYP/ 6-311++G(3df)**	
		ADE(eV)	**VDE(eV)**	**ADE (eV)**	**VDE(eV)**	**ADE (eV)**	**VDE(eV)**
NO	0.026[45]	0.37	0.92	−0.27	0.20	0.29	0.84
NO_2	2.27-2.38 [46,47,48]	2.29	2.96	1.99	2.61	2.20	2.87
NO_3	3.937[49,50]	4.03	4.10	3.75	3.80	3.96	4.03
$LiNO_3$		0.62	0.69	0.48	0.54	0.59	0.66
$MgNO_3$		1.64	1.94	1.45	1.68	1.53	1.81
$AlNO_3$		1.65	2.81	1.27	2.49	1.59	2.72

Our value for the ADE of NO_2 is in agreement with that measured by Lineberger and co-workers[46], electron transfer reaction studies[48], and ab-initio SCF calculations by Simons and co-workers[51]. However, the theoretical ADE of NO differs from the experimental value[45] by an

order of magnitude. This is because the ADE of NO is very low, and hence, it is computationally challenging to predict it accurately from first-principles. The value of ADE for NO using the CCSD(T) method and the 6-311++G* basis set is closer to the experimental result than that obtained from DFT-B3LYP. It has been shown by Arrington *et al*[52] that by using the coupled cluster method and extrapolating to the complete basis set limit, the theoretical ADE of NO can be found to be 0.028 eV. Our CCSD(T) result, however, is different from that of Arrington *et al* because of our choice of basis set. Our objective here is to compare the results between DFT and CCSD(T) by keeping the same basis sets. The experimental value of the ADE of NO_3[49, 50] is well predicted by DFT-B3LYP. Also, the changes in the ADE and VDE values by changing basis sets are very small. Performing coupled cluster calculations that explicitly include triple excitation with a complete basis set is difficult for larger clusters. Because the results for the larger clusters using the CCSD(T) and 6-311++G** basis set are close to the experiment and to the DFT-B3LYP level of theory (see Table 3-1), we have used the DFT-based method for the remainder of the calculations. We also point out that in previous reports, this level of theory has been used successfully[53, 54, 55].

3.1.2.2 *MNO_3; M = Li, Mg, Al*

We now study the interaction of NO_3 with metal atoms Li, Mg, and Al and examine their ability to form hyperhalogens. The optimized structures of neutral and anionic $M(NO_3)$ clusters are given in Figure 3-2. $LiNO_3$ is a closed-shell salt where electronic shell closure of both Li and NO_3 is satisfied. Therefore, the ADE is low (see Table 3-1). The NBO charges on Li and NO_3 are +0.94e and −0.94e, respectively, which confirms ionic bonding. In contrast, in $MgNO_3$ and $AlNO_3$, all atomic valencies of metal atoms are not satisfied. Therefore, we see that their ADEs

are more than double that of $LiNO_3$. Except for $AlNO_3$, the difference between the ADE and VDE is not very large, signifying that the neutral and anionic clusters have quite similar structures. We also observe that the electron detachment energy increases as M is changed from Li to Mg to Al. It should be pointed out that the geometries of $LiNO_3^-$, $MgNO_3$, $AlNO_3$, and $AlNO_3^-$ given in Figure 3-2 do not correspond to the global minima. For neutral $AlNO_3$, the ground-state structure is $O_2N{-}Al{-}O$ (see Figure I6 of Appendix I). This is because the valence of Al is 3. Therefore, one O atom splits from the NO_3 moiety and attaches individually to Al. The ground-state structures of $LiNO_3^-$, $MgNO_3$, and $AlNO_3^-$ are analogous.

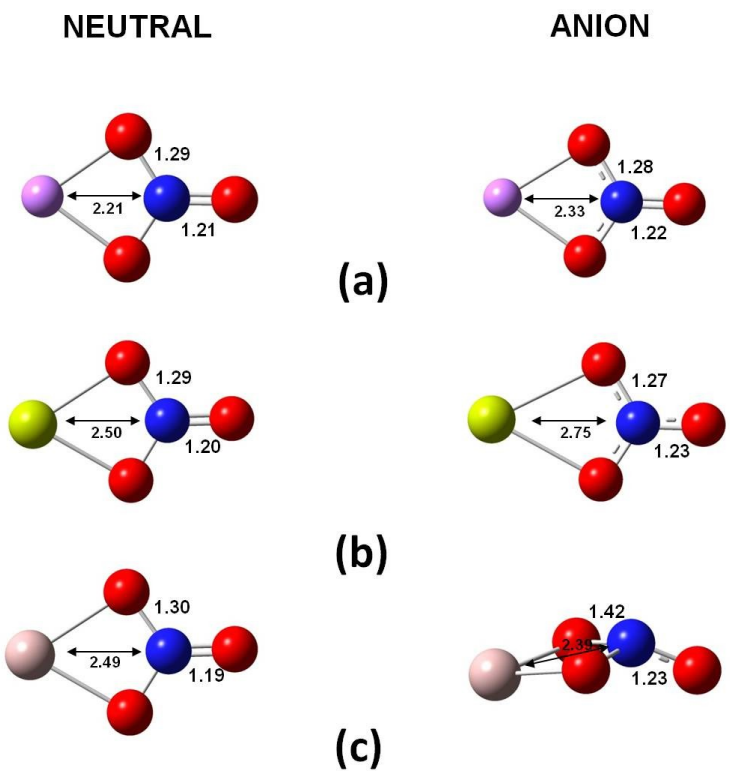

Figure 3-2: Optimized geometries of neutral and anionic MNO_3 (M =Li, Mg, Al).
(a) $LiNO_3$, (b) $MgNO_3$, and (c) $AlNO_3$

In earlier papers[56,57], we have shown that the mode of ligand binding plays an important role in determining the EA of a system. However, here, our goal is to achieve a fundamental understanding of how the ADE evolves in nitrate-based materials. Moreover, in the case of hyperhalogens and hypersalts, we note that the structures with intact NO_3 ligands are lowest in energy. Therefore, we emphasize the results where NO_3 moieties are intact. All VDEs, ADEs, and figures given in the text correspond to clusters with intact nitrate ligands. For systems where the ground state differs in structure, the geometries and corresponding relative energies are given in Appendix I.

3.1.2.3 *$M(NO_3)_2$; M = Li, Mg, Al*

The optimized geometries of $M(NO_3)_2$ are given in Figure 3-3. Two nitrate moieties are on opposite sides of the central metal atom. It should be pointed out that in species consisting of more than one ligand; dimerization of the ligand is possible. This has been shown to be the case in $Au(CN)_3$, where the ground-state structure is NC−Au−NCCN[56]. NO_3 does form a dimer N_2O_6. Though this dimer is stable with respect to dissociation into two NO_3 moieties by 1.04 eV, its fragmentation into N_2O_4+O_2 is favorable by 0.45 eV. Moreover, the NO_3−NO_3 binding energy (1.04 eV) is much less than M−NO_3 binding energies (5.14, 3.22, and 4.83 eV for M = Li, Mg, and Al, respectively). That is, NO_3 would much rather bind to the metal than to itself. This limits the probability of the dimerization of NO_3 before attaching to the metal atom. The structures of neutral and anionic $Li(NO_3)_2$ as well as neutral $Mg(NO_3)_2$ (as shown in Figure 3-3) are the global minimum structures. The ground-state geometries of $Al(NO_3)_2$ and $Mg(NO_3)_2^-$ are given in the Appendix I. From Table 3-2, we note that the ADE of $Li(NO_3)_2$ is 5.69 eV, which is higher than that of NO_3. Therefore, $Li(NO_3)_2$ is indeed a hyperhalogen. The extra electron is delocalized over

both nitrate groups in $Li(NO_3)_2$, as can be seen from the charge on each NO_3 of −0.44e in $Li(NO_3)_2^-$. In contrast, $Mg(NO_3)_2$ has a closed electronic shell. Therefore, its ADE is low. The bonding is ionic as the charge on Mg is +1.74 e, and that on each NO_3 is −0.87 e. In $Al(NO_3)_2$, the maximal valency of Al is not reached. Though the ADE is higher than that of $Mg(NO_3)_2$, it has not crossed the 3.62 eV benchmark. There is no efficient charge delocalization in either $Mg(NO_3)_2^-$ or $Al(NO_3)_2$.

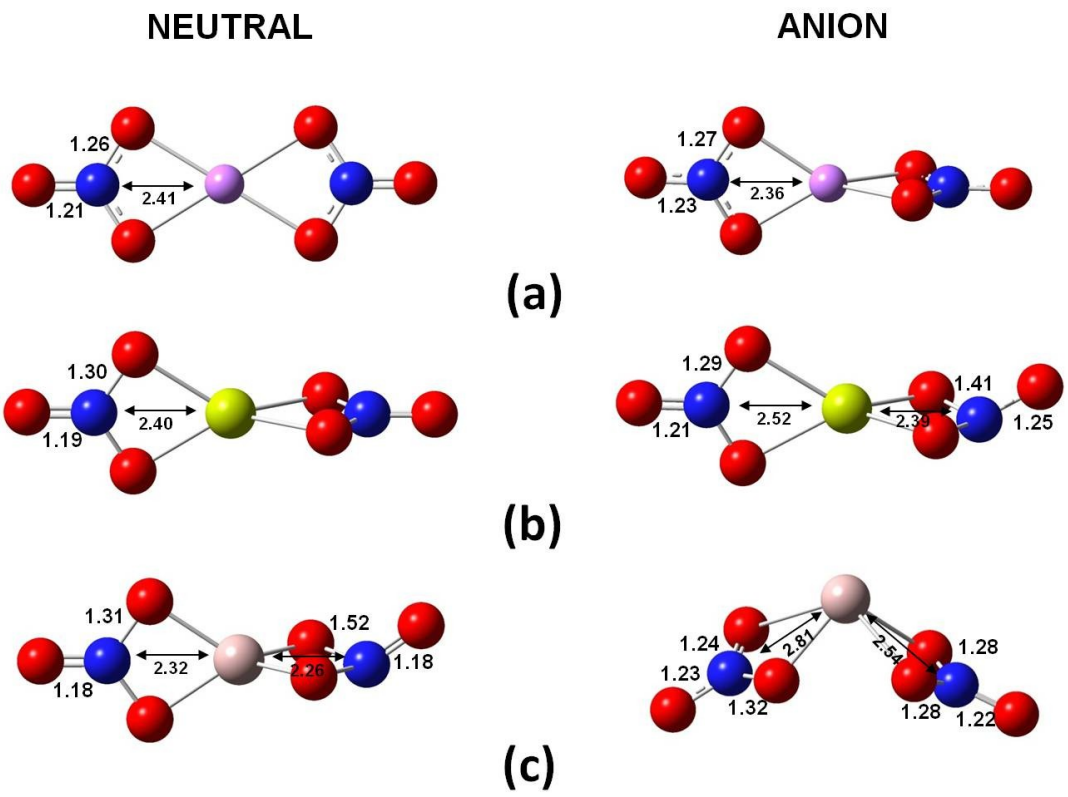

Figure 3-3: Optimized geometries of neutral and anionic $M(NO_3)_2$ (M = Li, Mg, Al). (a) $Li(NO_3)_2$, (b) $Mg(NO_3)_2$, and (c) $Al(NO_3)_2$.

3.1.2.4 *$M(NO_3)_3$; M = Mg, Al*

The optimized structures of neutral and anionic $M(NO_3)_3$ are shown in Figure 3-4. These geometries represent the global minima structures. Neutral $Mg(NO_3)_3$ has a C_1 symmetry.

However, we were also able to locate energetically nearly degenerate clusters with C_2 and C_3 symmetry (see Appendix I). This signifies that the bond between NO_3 and Mg is flexible, and minor changes in orientation of the NO_3 are possible. $Mg(NO_3)_3^-$ has D_3 symmetry, and the charge on all NO_3 moieties are equal to −0.91e. The effective charge delocalization makes the corresponding neutral a hyperhalogen. $Al(NO_3)_3$ is a neutral salt with a relatively low ADE (2.40 eV). In the neutral $Al(NO_3)_3$, the charge on Al is +1.82e, whereas that on each NO_3 is −0.61e. This cluster has C_3 symmetry as the three NO_3 ligands satisfy the valency of the Al atom. On the other hand, $Al(NO_3)_3^-$ is slightly distorted due to the presence of the extra electron in an otherwise closed-shell structure.

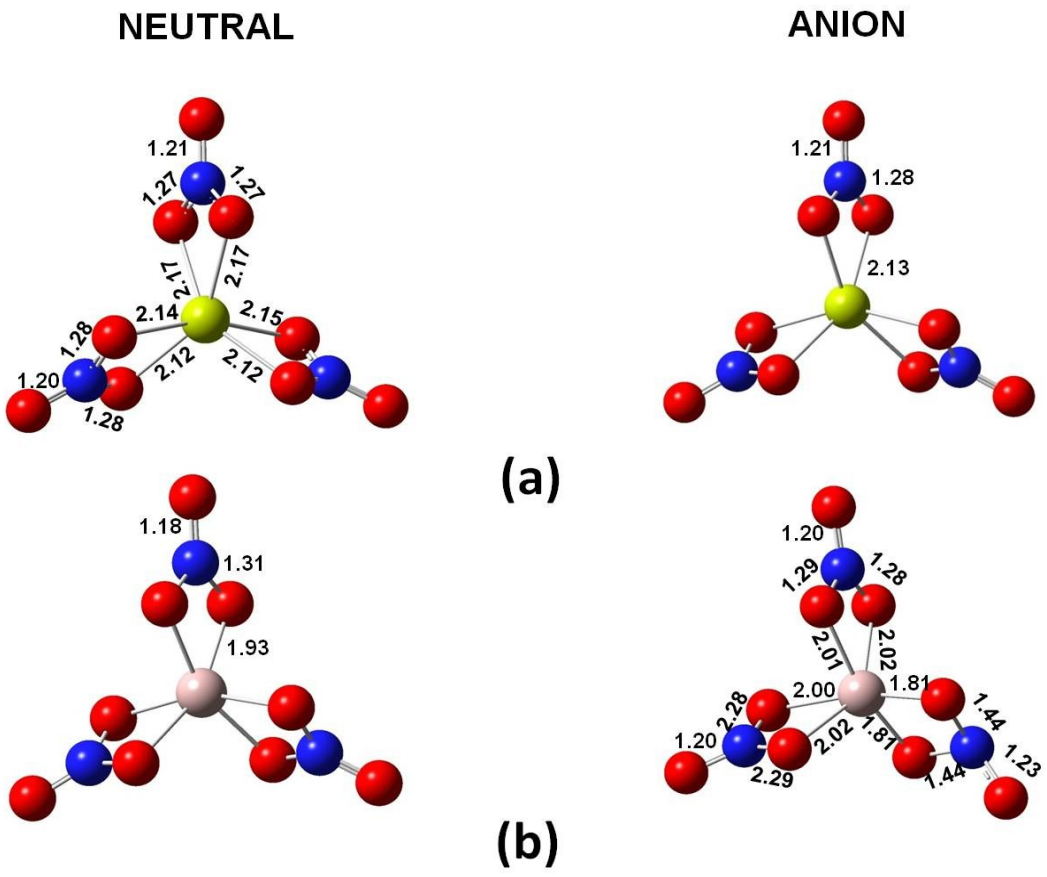

Figure 3-4: Optimized geometries of neutral and anionic $M(NO_3)_3$ (M = Mg, Al).
(a) $Mg(NO_3)_3$ and (b) $Al(NO_3)_3$.

3.1.2.5 $M(NO_3)_4$; M = Al

The optimized geometries of the neutral and the anionic clusters are given in Figure 3-5.

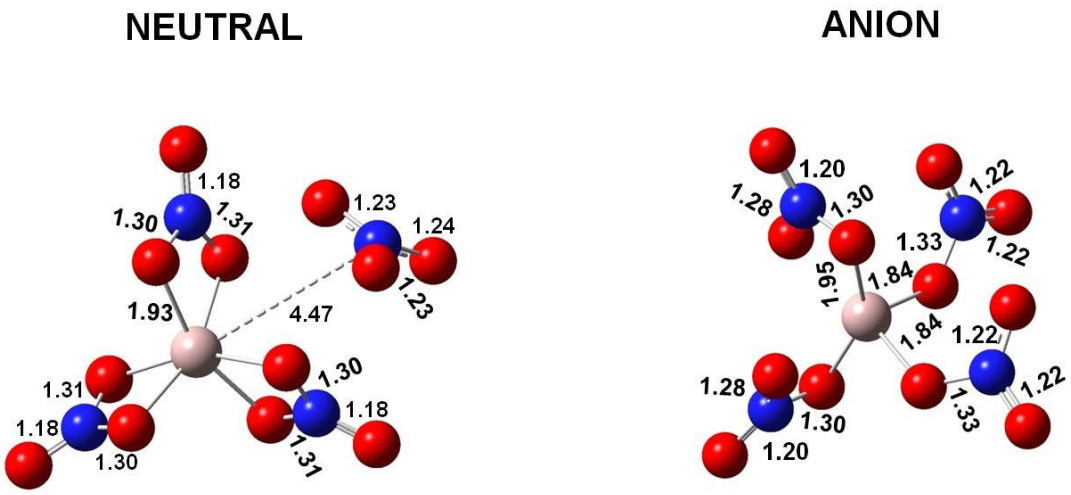

Figure 3-5: Optimized geometries of neutral and anionic $M(NO_3)_4$ (M = Al).

In the neutral cluster, as the valency of the Al atom is satisfied by three NO_3 ligands, we can see that the fourth NO_3 ligand is moving apart. This ligand behaves as an individual NO_3 molecule with its bond lengths similar to that of the neutral NO_3, whereas in the anionic cluster, the electron deficiency is satisfied upon adding an extra electron. We found two isomers in the anionic clusters with C_1 (as shown in Figure 3-5) and C_2 symmetry (as shown in Figure I8 of Appendix I) with an energy difference of +0.16 eV. The higher-energy isomer (C_2 symmetry) is found to be more symmetric compared to its ground-state isomer (C_1 symmetry). In the C_2 symmetry, the charge on Al is +1.97e, and that on each NO_3 ligand is −0.74e.

Table 3-2: Electron Detachment Energies of $M(NO_3)_x$ clusters at the B3LYP/6−311++G** level of theory.

	$M(NO_3)_x$					
	M=Li		M=Mg		M=Al	
x	VDE (eV)	ADE (eV)	VDE (eV)	ADE (eV)	VDE (eV)	ADE (eV)
2	5.80	5.69	3.03	1.45	3.74	2.31
3			6.69	6.64	4.34	2.40
4					6.86	6.42

3.1.2.6 Stability with respect to fragmentation:

To study the stability of these clusters, we have calculated the fragmentation energies of the neutral as well as the anionic clusters. The following fragmentation channels were considered:

$$\Delta E_{\text{neutral}} = -\{E[\text{M(NO}_3)_x] - E[\text{M(NO}_3)_{x-1}] - E[\text{NO}_3]\}$$

$$\Delta E^{1}_{\text{anion}} = -\{E[\text{M(NO}_3)_x^-] - E[\text{M(NO}_3)_{x-1}^-] - E[\text{NO}_3]\}$$

$$\Delta E^{2}_{\text{anion}} = -\{E[\text{M(NO}_3)_x^-] - E[\text{M(NO}_3)_{x-1}] - E[\text{NO}_3^-]\}$$

The fragmentation energies for the preferred neutral and anionic clusters are given in the Table 3-3. The fragmentation energies of the neutral $LiNO_3$, $Mg(NO_3)_2$, and $Al(NO_3)_3$ are very high as the number of NO_3 moieties satisfies the valency of the respective metal atoms. Hence, they are very stable salts. However, the fragmentation energy of the corresponding neutral species decreases drastically as the number of NO_3 moieties exceeds their valency because the clusters need one more electron to form a closed shell.

Table 3-3: Fragmentation Energies of the $M(NO_3)_x$ Clusters.

No. of NO_3	Cluster	BE in eV
x=1	$LiNO_3 \rightarrow Li + NO_3$	5.14
x=2	$Li(NO_3)_2 \rightarrow LiNO_3 + NO_3$	0.69
x=1	$MgNO_3 \rightarrow Mg + NO_3$	3.22
x=2	$Mg(NO_3)_2 \rightarrow MgNO_3 + NO_3$	4.92
x=3	$Mg(NO_3)_3 \rightarrow Mg(NO_3)_2 + NO_3$	0.28
x=1	$AlNO_3 \rightarrow Al + NO_3$	4.83
x=2	$Al(NO_3)_2 \rightarrow AlNO_3 + NO_3$	3.37
x=3	$Al(NO_3)_3 \rightarrow Al(NO_3)_2 + NO_3$	4.86
x=4	$Al(NO_3)_4 \rightarrow Al(NO_3)_3 + NO_3$	0.08
x=1	$LiNO_3^- \rightarrow Li + NO_3^-$	0.06
x=2	$Li(NO_3)_2^- \rightarrow LiNO_3 + NO_3^-$	2.35
x=1	$MgNO_3^- \rightarrow Mg + NO_3^-$	0.82
x=2	$Mg(NO_3)_2^- \rightarrow MgNO_3 + NO_3^-$	2.34
x=3	$Mg(NO_3)_3^- \rightarrow Mg(NO_3)_2 + NO_3^-$	2.89
x=1	$AlNO_3^- \rightarrow Al + NO_3^-$	2.45
x=2	$Al(NO_3)_2^- \rightarrow AlNO_3 + NO_3^-$	1.65
x=3	$Al(NO_3)_3^- \rightarrow Al(NO_3)_2 + NO_3^-$	3.22
x=4	$Al(NO_3)_4^- \rightarrow Al(NO_3)_3 + NO_3^-$	2.14

3.1.2.7 Designing Hypersalts using Superhalogen ligand: $KLi(NO_3)_2$, $KMg(NO_3)_3$, and $KAl(NO_3)_4$

From our above discussion we find that $Li(NO_3)_2$, $Mg(NO_3)_3$, and $Al(NO_3)_4$ are all hyperhalogens. By adding a counter cation such as K to the negative ions of these clusters, one can imagine forming *hypersalts*. Figure 3-6 shows the ground-state optimized structures of these salt moieties. To obtain these geometries we started with the anion geometry of the hyperhalogen and added a K atom to it.

The stability of these salts was determined by considering the energetics of the following dissociation pathways:

$$\Delta E_1 = -[KM(NO_3)_x - K^+ - M(NO_3)_x^-]$$

$$\Delta E_2 = -[KM(NO_3)_x - K - M(NO_3)_x]$$

$$\Delta E_3 = -[KM(NO_3)_x - KNO_3 - M(NO_3)_{x-1}]$$

These energies, given in Table 3-4, are all positive, indicating that these salts are stable with respect to fragmentation.

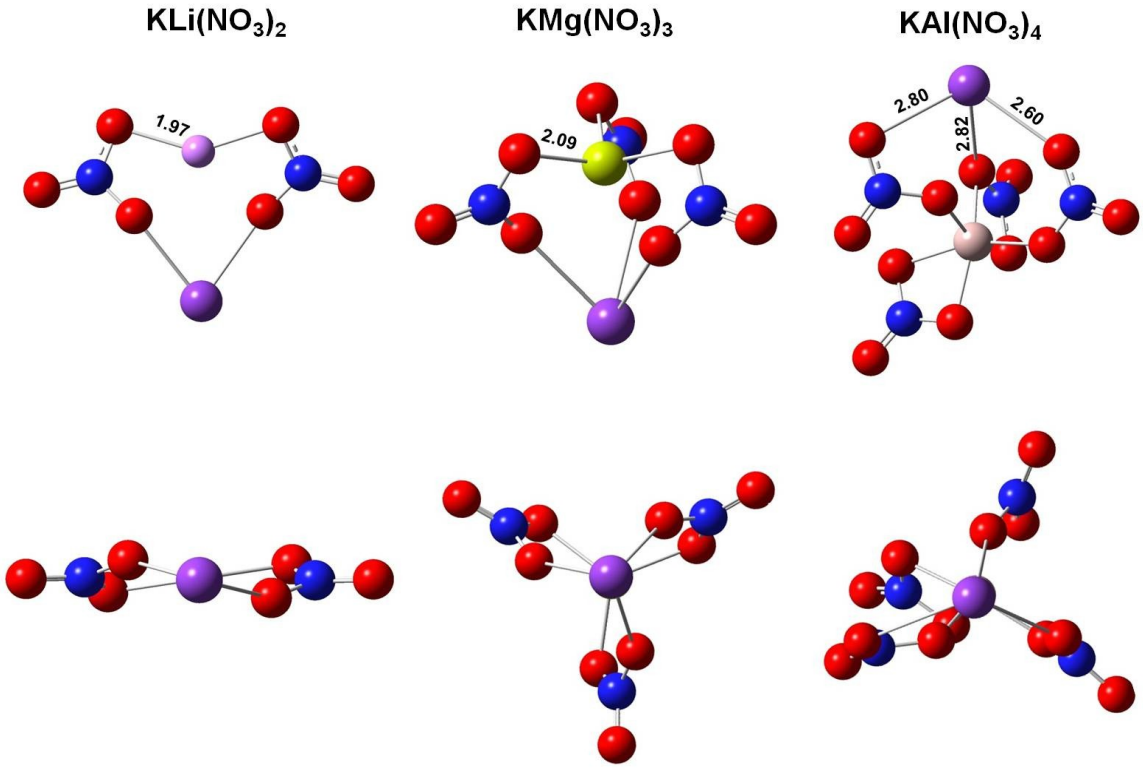

Figure 3-6: Ground-state structures of (from left) $KLi(NO_3)_2$, $KMg(NO_3)_3$, and $KAl(NO_3)_4$. The first row and the second row are the front and the side views of the respective salts' clusters.

We note that in 1998, $KLi(NO_3)_2$ was established to be a congruently melting compound using Raman spectroscopy[58]. It was found that Li ions are tetrahedrally coordinated to nitrate ions to

form polymeric complexes. Because the theoretically designed $KLi(NO_3)_2$ cluster consists of a single building unit of a polymeric $KLi(NO_3)_2$ system, it shows two-fold symmetry. When these units are assembled to form a polymeric system, it will lead to a crystal structure where all of the Li ions will be tetrahedrally coordinated with nitrate ions, giving it a symmetrical structure. A similar situation was found in the case of the $NaAlH_4$ crystal structure, where all of the H-atoms are tetrahedrally coordinated with Na; however, in the single building unit, two of the bond lengths between Na and H atoms are elongated[59, 60]. Similar structures were obtained by replacing K by Rb and Cs. We also note that $KAg(NO_3)_2$ is a known salt, which can be viewed as a hypersalt per our terminology.

Table 3-4: Fragmentation Energies of the Hypersalts $KM(NO_3)_x$.

Cluster	ΔE_1	ΔE_2	ΔE_3
$KLi(NO_3)_2$	4.24	5.43	1.63
$KMg(NO_3)_3$	4.00	6.14	1.94
$KAl(NO_3)_4$	4.19	5.79	1.38

3.1.3 Conclusion

We have carried out a systematic study of the structure and stability of neutral and anionic NO_x ($x = 1 - 3$) and $M(NO_3)_x$, where M = Li, Mg, and Al and $x = 1 - 2$ for Li, $x = 1 - 3$ for Mg, and $x = 1 - 4$ for Al. We found that the nitrate (NO_3) molecule whose EA of 4.03 eV is higher than that of Cl (3.6 eV) can be used as a building block of hyperhalogens containing metal atoms Li, Mg, and Al. This is confirmed by calculating the ADEs of the hyperhalogens $Li(NO_3)_2$, $Mg(NO_3)_3$, and $Al(NO_3)_4$, which are, respectively, 5.69, 6.64, and 6.42

eV. We have interacted these hyperhalogens with the cation K, and the resulting salts, namely, $KLi(NO_3)_2$, $KMg(NO_3)_3$, and $KAl(NO_3)_4$, are found to be stable against fragmentation. These salts are interpreted as hypersalts. This new class of salts, due to their high content of nitrates, may have applications as high energy density materials.

3.2 Clusters mimicking properties of alkalis: '*Superalkalis*'

3.2.1 Introduction

Among the elements in the periodic table, alkali metal atoms possess very low ionization potentials (IP), with Cs having the lowest IP, *i.e.* 3.89 eV, of them all. The class of cluster known as superalkali was proposed by Gutsev and Boldyrev[61] in 1982 with a general formula $M_{k+1}L$, where M is an alkali atom and L is an electronegative atom with valence of *k*. Typical examples of superalkalis includes Li_2X (X=F, Cl, Br, I)[62,63, 64, 65, 66], M_3O (M=Li, Na, K)[67,68, 69], Li_4N[70], BLi_6[71], *etc*. Studies in the past five years have greatly expanded the scope of superalkalis. For example, it has been shown that non-metallic (for example: $C_2H_9^+$, $O_2H_5^+$, $F_2H_3^+$) as well as polynuclear superalkalis cations (for example: $Li_3SO_3^+$, $Li_3CO_3^+$, $Li_3O_4^+$) with various functional groups as the central core can be synthesized[72,73].

A novel class of salts can be synthesized by either using superalkalis as cations or superhalogens as anions. These salts already exist. For example $CsAuF_6$[74], $KMnO_4$[75] , and $KMnCl_3$[76] can be regarded as $Cs^+(AuF_6)^-$, $K^+(MnO_4)^-$, and $K^+(MnCl_3)^-$ where the metal atoms form the conventional cation cores and the anions are known superhalogens. Similarly, experimentally synthesized Li_3NO_3[77] and Na_3NO_3 [78] can be thought of as $(Li_3O)^+(NO_2)^-$ and $(Na_3O)^+(NO_2)^-$ where the cation cores are superalkalis and NO_2 with an electron affinity of

2.27−2.38 eV[46,47] mimics the chemistry of a halogen anion. Possibility of creating salts with superalkalis as cations and superhalogens as anions are less explored.

Our objectives in this study are 2−fold: First, we investigate the possibility of creating *supersalts* by considering the interaction between Li_3O, Cs_2Cl, and Cs_2NO_3 as prototypical superalkalis and BF_4, BeF_3, and NO_3 as prototypical superhalogens. Second, we consider the possibility that superalkalis can also be used as the core to synthesize *hyperhalogens*. The details on computational methodology are provided in section 2.9 of chapter 2. Results and discussions are given in section 3.2.2, followed by conclusions in section 3.2.3.

3.2.2 Results and Discussions

3.2.2.1 Designing Supersalts using Superalkali and Superhalolgen:

3.2.2.1.1 Superalkalis:

We have used three molecules as examples of superalkalis. These include Cs_2Cl, $Cs_2(NO_3)$, and Li_3O. While they all satisfy the formula for superalkali in that each molecule has one electron more than required for shell closing, they have different cores. Cs_2Cl is the standard superalkali, which has two alkali atoms bound to one halogen atom. Similarly, in Cs_2NO_3 the Cl atom in Cs_2Cl atom is replaced by NO_3, which with an electron affinity of 4.03 eV, is a superhalogen[79]. Li_3O, however, can be thought of as $(Li_2O)Li$. It is an example of a hypermetalated molecule with a stoichiometry that violates the octet rule[80]. The equilibrium geometries of these superalkalis in cationic form along with bond lengths and NBO charges are given in Figure 3-7. The vertical ionization potentials (VIP), *i.e.*, energy needed to remove an electron from the neutral without changing its geometry, of Li_3O, Cs_2Cl, and Cs_2NO_3 are 3.85, 3.00, and 3.12 eV, respectively as shown in Table 3-5. These

values are less than the ionization potential of Cs, namely, 3.89 eV, and satisfy the definition of a superalkali. The above calculated values compare well with previous calculations[81].

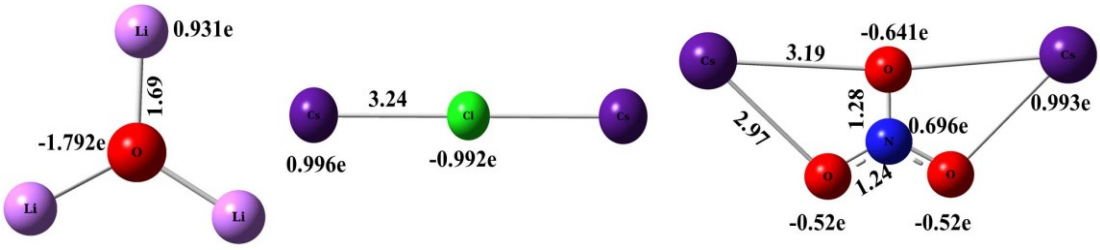

Figure 3-7: Optimized geometries of superalkalis (from left: Li_3O^+, Cs_2Cl^+, $Cs_2NO_3^+$).

3.2.2.1.2 Superhalogens:

As discussed earlier, the specific superhalogens we used in this study are BF_4, BeF_3, and NO_3. The calculated vertical detachment energies (VDE) of BF_4, BeF_3, and NO_3 are respectively 7.34, 6.64, and 4.04 eV. BeF_3 and BF_4 are conventional superhalogens as they follow the rule MX_{k+1} (discussed earlier in section 3.1.1). NO_3 is an unconventional superhalogen[79] as it neither contains a metal atom nor a halogen atom. The equilibrium geometries and NBO charges of the anions of these molecules are given in Figure 3-8.

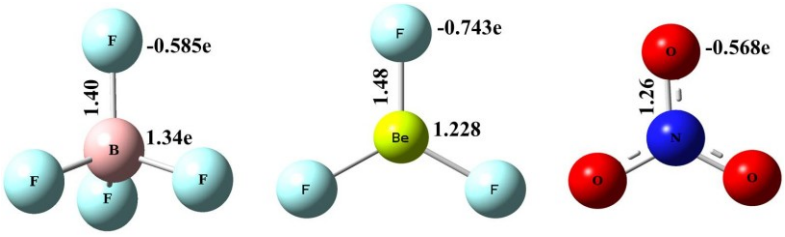

Figure 3-8: Optimized geometries of superhalogens (from left: BF_4^-, BeF_3^-, NO_3^-).

The calculated VDE values given in Table 3-5 are in good agreement with previously reported results[79,82]. It is to be noted that, when the structures of neutral and anionic species are nearly the same, the VDE and EA values do not differ significantly. In such cases, VDE can also be used as a parameter to define super- and hyperhalogen behavior. Now we are in a position to build salts composed of superalkalis and superhalogens as building blocks.

3.2.2.1.3 Supersalts:

In this section we examine whether the superalkali Li_3O can form stable supersalts when interacting with superhalogen moieties such as BF_4, BeF_3 and NO_3. The binding energies of supersalts are calculated using the equation,

$$\Delta E_{supersalt} = \{[E(\text{superalkali cation}) + E(\text{superhalogen anion})] - E(\text{supersalt})\} \quad (1)$$

Details on supersalts using Li_3O superalkalis and various superhalogens are discussed below.

1) **<u>$(Li_3O)(BF_4)$:</u>**

We begin our discussion with $(Li_3O)(BF_4)$. Optimized geometries of the ground state and low lying isomers of neutral $(Li_3O)(BF_4)$ along with bond lengths and NBO charges are given in Figure 3-9. The various isomers are denoted as (a) face-on-face (*f-f*), (b) face on-edge (*f-e*), and (c) edge-on-edge (*e-e*) structures. All the isomers are energetically nearly degenerate. To elucidate the nature of bonding in $(Li_3O)(BF_4)$ cluster, we have computed the NBO charges. We find that in all the three isomers, Li_3O and BF_4 subunits possess charges around +0.9e and −0.9e, respectively. This suggests that the bonding has strong ionic character between the cation and the anionic complexes as BF_4 takes an electron to become BF_4^- (superhalogen) and Li_3O loses an electron to form Li_3O^+ (superalkali).

The binding energies of these isomers as calculated using equation (1) is shown in Table 3-5. These values compare well with previous calculations[83]. Although their binding energies are smaller than that of LiF (which is 8.02 eV measured with respect to dissociation into Li^+ and F^-), they are large and confirm that the $(Li_3O)(BF_4)$ supersalt is indeed stable.

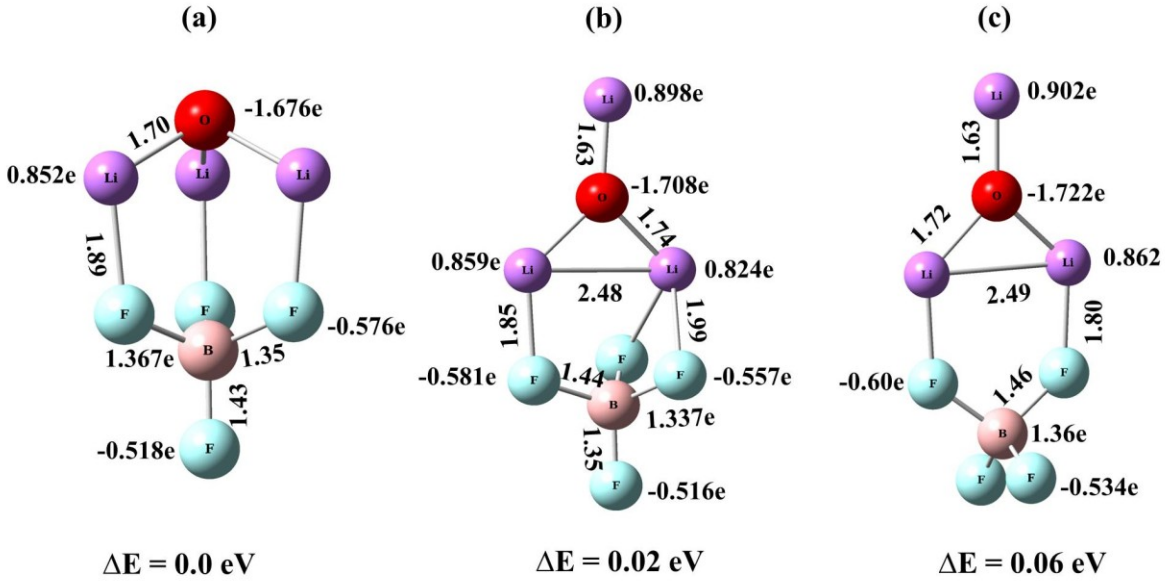

Figure 3-9: Optimized geometries of isomers of $(Li_3O)(BF_4)$ supersalt. The ground state is defined as $\Delta E = 0.0$ eV.

The increase in the relative stability of these isomers in going from *f-f* > *f-e* > *e-e* is consistent with the number of atoms, namely, 6, 5, and 4, involved in bonding between the superalkali cation and superhalogen anion. We also note that in two of the isomers, geometries of Li_3O^+ and BF_4^- remain close to their respective isolated structures, while for the *f-f* structure in Figure 3-9a, the geometry of Li_3O is altered from being planar to non-planar. The Li−O and B−F distances in isolated Li_3O^+ and BF_4^- are 1.69 and 1.40 Å, respectively. These bonds are slightly stretched, once the salt is formed.

2) **$(Li_3O)(BeF_3)$:**

The optimized geometry of the ground state of $(Li_3O)(BeF_3)$ along with the equilibrium bond distances and NBO charges are given in Figure 3-10a. We found only edge-on-edge isomer of $(Li_3O)(BeF_3)$ to have a stable form. Here the Li_3O core almost retains its planar configuration as in Li_3O^+, but the Li−O bond distances are altered from that in Li_3O^+, namely, 1.69 Å. The Li−O bond length, where the Li atom is attached to the F atom in the BeF_3 complex, is 1.73 Å, while the other Li−O bond length is 1.64 Å, same thing happens for the BeF_3 unit as well. This is due to the interaction between Li and F in the $(Li_3O)(BeF_3)$ complex.

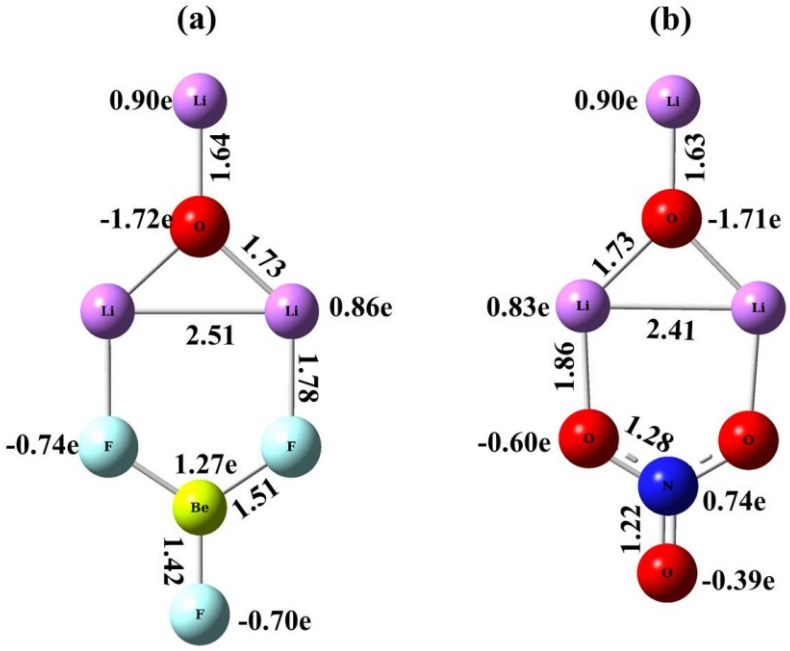

Figure 3-10: Optimized geometries of (a) $(Li_3O)(BeF_3)$ and (b) $(Li_3O)(NO_3)$ supersalts.

The NBO charges on each subunit also reveal that there is strong ionic bonding between Li_3O and BeF_3. The charges on each subunit are approximately ±0.9e showing that the bonding between the two moieties is ionic, and Li_3O behaves as a cation, while BeF_3 behaves as an anion.

However, the individual charges on Li atoms in Li_3O unit and F atoms in BeF_3 unit are different. The binding energy of $(Li_3O)(BeF_3)$ measured against dissociation into Li_3O^+ and BeF_3^- is 5.57 eV indicating that this is a stable salt. The small EA of $(Li_3O)(BeF_3)$ is characteristic of a closed shell configuration.

3) **$(Li_3O)(NO_3)$:**

The ground state geometry of $(Li_3O)(NO_3)$, along with optimized bond lengths and NBO charges, are given in Figure 3-10b. We considered different possible geometries of $(Li_3O)(NO_3)$, but an edge-on-edge isomer was found to have the lowest energy. In $(Li_3O)(NO_3)$ the subunits Li_3O and NO_3, respectively, carry +0.9e and −0.9e charge, confirming that this indeed is a salt. Both subunits also have very similar structures as their isolated charged geometries given in Figures 3-7 and 3-8. However, when they form a salt, the bond distances are changed. There are two different Li−O and N−O bond distances; one is larger and is associated with the Li atoms interacting with the NO_3 subunit. This is also true for N−O distances in the NO_3 subunit. The interacting N−O distance is increased slightly from 1.26 to 1.28 Å, whereas the non-interacting N−O decreases to 1.22 Å. The charge on the Li atoms interacting with NO_3 is decreased from 0.9e to 0.8e, while the charge on the O atom in NO_3 interacting with the O atom of Li_3O changes form −0.57e to −0.60e. The binding energy of $(Li_3O)(NO_3)$ measured with respect to its fragmented charge subunits is 5.51 eV confirming its stability as a salt. This is also complemented by its low EA, namely, 0.64 eV.

Table 3-5: Calculated Vertical Ionization Potential (VIP), Electron Affinity (EA), Vertical Detachment Energy (VDE), and Binding Energy (ΔE) of the studied superalkali, superhalogen, supersalt, and potential hyperhalogen complexes; (a), (b), and (c) represent different isomers for a particular system.

Compounds	***Point group symmerty***	**VIP (*eV*)**	**EA (*eV*)**	**VDE (*eV*)**	**ΔE (*eV*)**
Superalkali					
Li_3O	D_{3h}	3.85			
Cs_2NO_3	C_{2v}	3.12			
Cs_2Cl	$D_{\infty h}$	3.00			
Superhalogen					
BF_4	T_d			7.34	
BeF_3	D_{3h}			6.64	
NO_3	D_{3h}			4.04	
Supersalt					
Li_3O-BF_4 (a)	C_{3v}		0.19		5.16
Li_3O-BF_4 (b)	C_s		0.62		5.14
Li_3O-BF_4 (c)	C_{2v}		0.74		5.10
Li_3O-BeF_3	C_{2v}		0.69		5.57
Li_3O-NO_3	C_{2v}		0.64		5.51
Potential Hyperhalogen					
Li_3O-$(BF_4)_2$ (a)	C_{2v}			5.17	2.00
Li_3O-$(BF_4)_2$ (b)	C_s			4.88	1.26
Li_3O-$(BeF_3)_2$ (a)	C_s			5.35	2.00
Li_3O-$(BeF_3)_2$ (b)	C_1			4.81	2.13
Li_3O-$(NO_3)_2$	C_s			4.55	2.16
$(Li_3O)_2$-$(NO_3)_3$	C_s			4.64	3.16
Cs_2Cl-$(NO_3)_2$	C_1			5.13	5.09
Cs_2NO_3-$(NO_3)_2$	C_{2v}			5.22	5.20

3.2.2.2 Designing Hyperhalogens using Superalkali core:

From our above discussion, we confirmed the existence of supersalts where the superalkali Li_3O act as a cation and superhalogen moieties, BF_4, BeF_3, and NO_3 act as anionic part of the stable salt. In this section, we examine whether superalkali can act a building block of hyperhalogens. This is achieved by adding more superhalogen units to the superalkali core. We describe our results in the following section.

a) **<u>$(Li_3O)(BF_4)_2$:</u>**

To see if the addition of an extra BF_4 unit to the supersalt $(Li_3O)(BF_4)$ can make a hyperhalogen, we first calculated the equilibrium geometry and total energy of $(Li_3O)(BF_4)_2$ anion. Two different $[(Li_3O)(BF_4)_2]^-$ isomers with very similar energy values are found. The geometries of these isomers along with their bond distances and NBO charges are given in Figure 3-11. The binding energy of $(Li_3O)(BF_4)_2$ is calculated using the equation:

$$\Delta E = \{E[(Li_3O)(BF_4)] + E(BF^-_4)\} - E[(Li_3O)(BF_4)_2]^- \quad (2)$$

The VDE and binding energy values are given in Table 3-5. The VDE of these two isomers are 5.17 and 4.88 eV. These values are smaller than the VDE of BF_4 moiety (7.34 eV). We note that hyperhalogen behavior is traditionally confirmed by comparing the electron affinity values. Since the EAs are always less than the corresponding VDEs, we can conclude without computing the energy of the ground state of neutral $(Li_3O)(BF_4)_2$ that, it is not a hyperhalogen. Comparing $(Li_3O)(BF_4)_2$ with $Li(BF_4)_2$ we note that, $Li(BF_4)_2$ with a VDE of 8.64 eV acts as a hyperhalogen. This difference is due to the larger core size of the cation component of $(Li_3O)^-$ $(BF_4)_2$, which results in a larger distance between the cation and anion centers, thus reducing their binding energy. Thus, Li_3O superalkali fails to make a hyperhalogen.

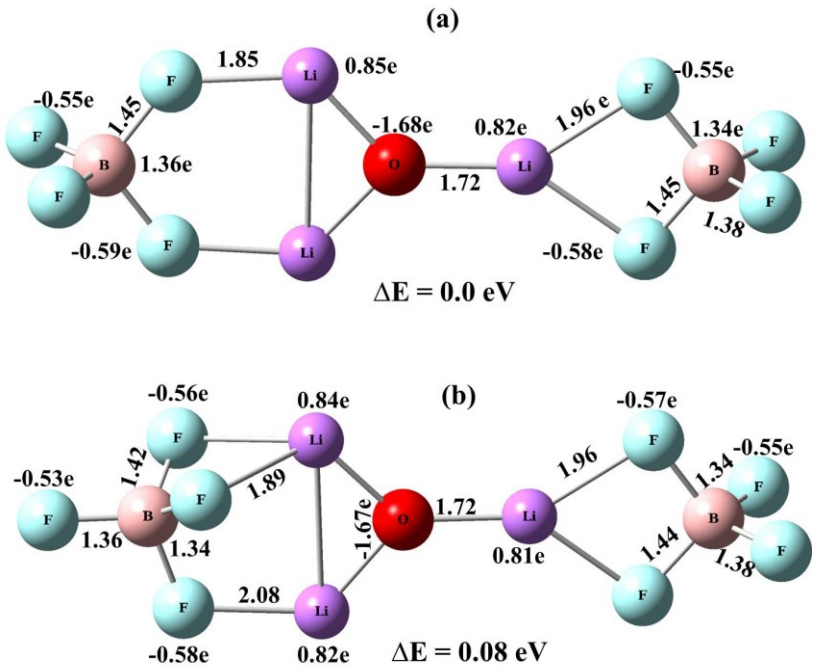

Figure 3-11. Optimized geometries of isomers of $(Li_3O)(BF_4)_2$ molecules. The ground state is defined as ΔE = 0.0 eV.

b) **<u>$(Li_3O)(BeF_3)_2$:</u>**

The potential of superalkali Li_3O to make a hyperhalogen with BeF_3 moieties as ligands was examined by first calculating the geometries and total energies of $[(Li_3O)(BeF_3)_2]^-$ anion. The geometries of these isomers along with their bond distances and NBO charges are given in Figure 3-12. We again found that two possible isomers of $(Li_3O)(BeF_3)_2$ are very close in energy, with the C_1 isomer being slightly more stable than the C_s isomer by 0.14 eV. The stability of these complexes depends on the number of atoms responsible to form the complex. The number of interacting atoms in the C_1 isomer is larger than that in the C_s isomer. The NBO charges on each atomic site have similar trend as in $(Li_3O)BeF_3$ complex.

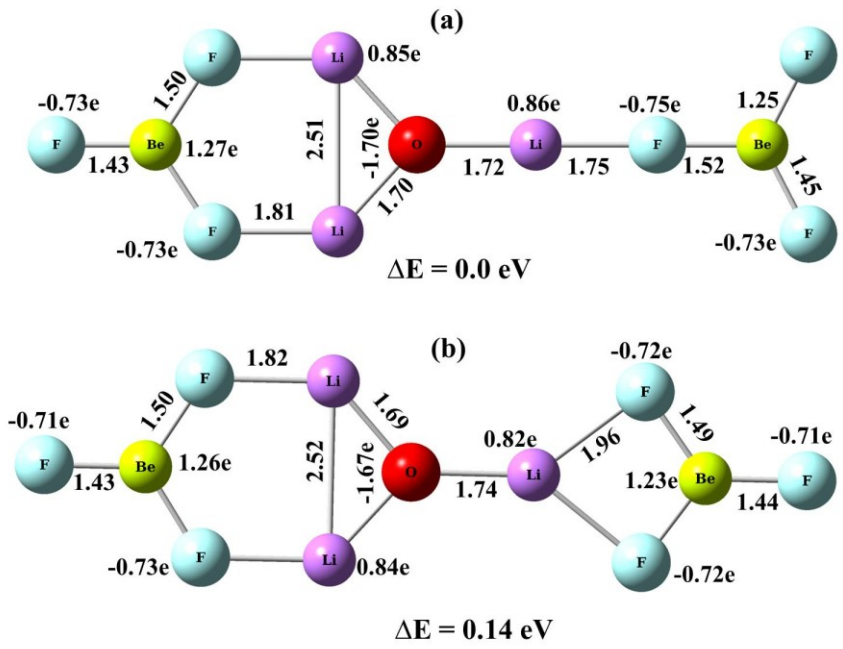

Figure 3-12: Optimized geometries of isomers $(Li_3O)(BeF_3)_2$ molecules. The ground state is defined as $\Delta E = 0.0$ eV.

To check whether these complexes are hyperhalogens, we have computed the VDE values of both the isomers, which are, respectively, 5.35 and 4.81 eV. Once again, while $(Li_3O)(BeF_3)_2$ behaves like a superhalogen, it is not a hyperhalogen as its VDE is less than that of BeF_3, namely, 6.64 eV. The binding energy of $(Li_3O)(BeF_3)_2$ was calculated using the same procedure as described in equation (2), but with appropriate components. The results are given in Table 3-5. The reason for its low binding energy and lack of hyperhalogen behavior is same as that discussed for $(Li_3O)(BF_4)_2$ above.

c) **$(Li_3O)(NO_3)_2$:**

Next we have examined the potential of $(Li_3O)(NO_3)_2$ to become a hyperhalogen. The calculated VDE and equilibrium geometries along with NBO charges are given in Table 3-5 and Figure 3-13, respectively. We found the VDE of $(Li_3O)(NO_3)_2$ to be 4.55 eV, which is larger than that of

its superhalogen building block NO_3, namely, 4.04 eV. This result suggests that $(Li_3O)(NO_3)_2$ is indeed a hyperhalogen. To see whether increasing the number of core and ligand moieties can further increase the VDE, we studied the $(Li_3O)_2(NO_3)_3$ complex. The geometries of $(Li_3O)_2(NO_3)_3$ is also given in Figure 3-13. The VDE indeed increased with an increase in cluster size, but not significantly. Nevertheless, $(Li_3O)_2(NO_3)_3$ can also be classified as a hyperhalogen. We note that the ionization potential of Li_3O is lower than that of Li. On the basis of this fact alone, one would expect that Li_3O can form a compound with stronger hyperhalogen property than Li. However, this is not the case. VDE of $Li(NO_3)_2$, namely, 5.80 eV,[79] is higher than that of $(Li_3O)-(NO_3)_2$ and $(Li_3O)_2(NO_3)_3$. This is again due to the large size of the superalkali core. From the above discussion it can be summarized that although superalkali Li_3O is not a good candidate to replace simple alkali atom to form a hyperhalogen compound, it is possible if suitable ligands like NO_3 are chosen.

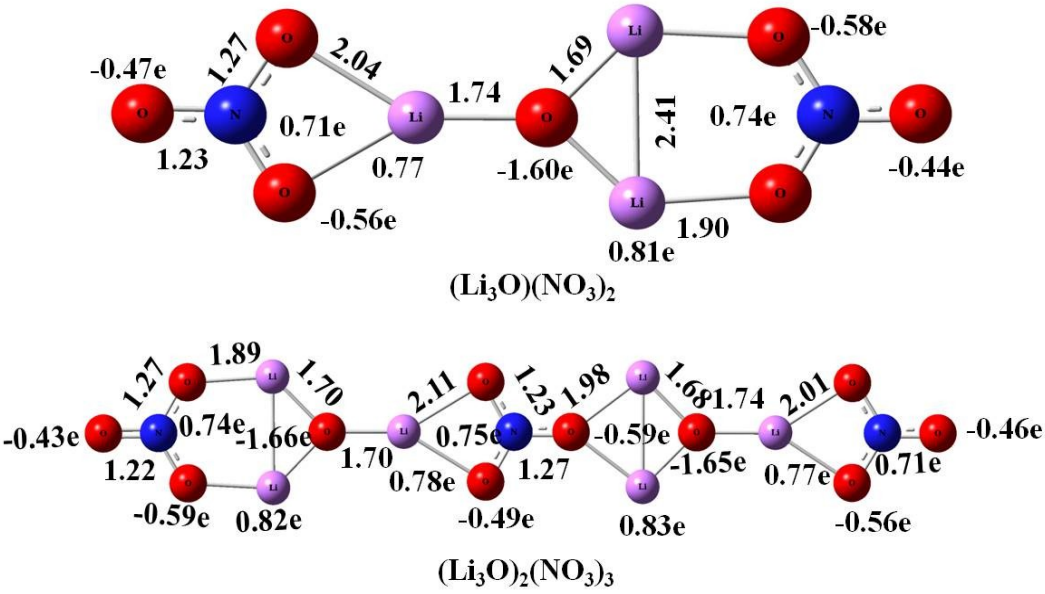

Figure 3-13: Optimized geometries of isomers $(Li_3O)(NO_3)_2$ and $(Li_3O)_2(NO_3)_3$ molecules.

The binding energy of $(Li_3O)(NO_3)_2$ was calculated using the same procedure as described in equation (2), but with appropriate components. The results are given in Table 3-5. Note that the binding energy is slightly higher than those of $(Li_3O)(BF_4)_2$ and $(Li_3O)(BeF_3)_2$.

d) **$(Cs_2Cl)(NO_3)_2$ and $(Cs_2NO_3)(NO_3)_2$:**

From our previous discussion, we found that among all the superhalogens studied here, NO_3 is a suitable ligand to form hyperhalogen complexes with Li_3O. To see if it can produce hyperhalogens with other superalkalis such as Cs_2Cl and Cs_2NO_3 as the core, we have calculated the equilibrium geometries of $(Cs_2Cl)(NO_3)_2$ and $(Cs_2NO_3)(NO_3)_2$ (given in Figure 3-14).

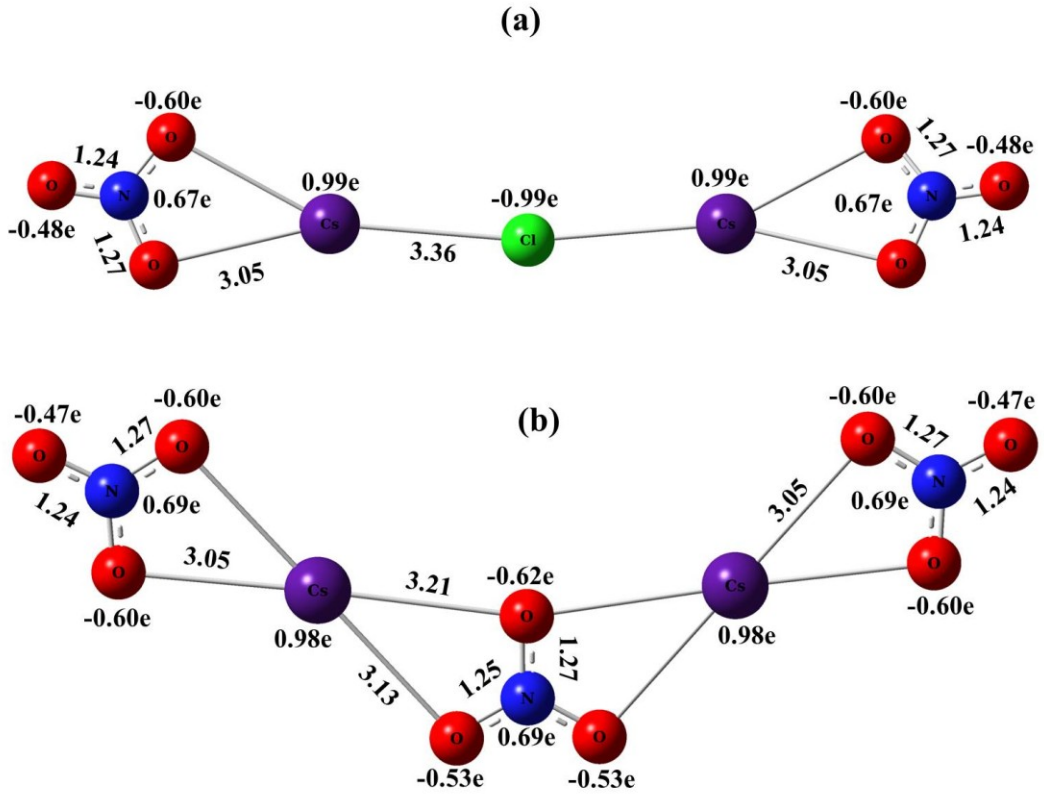

Figure 3-14: Optimized geometries of $(Cs_2Cl)(NO_3)_2$ and $(Cs_2NO_3)(NO_3)_2$ molecules.

The first cluster contains mixed anions such as Cl and NO_3, while the second cluster contains only NO_3 as ligands. From the results given in Table 3-5, it is confirmed that both Cs_2Cl and Cs_2NO_3 with ionization potentials of 3.00 and 3.12 eV, respectively, are superalkalis. We note that the ionization potential of Li_3O, namely, 3.85 eV, is larger than these two superalkali moieties. The bond distance between Cs and Cl in $(Cs_2Cl)(NO_3)_2$ is larger than that between Cs and O in $(Cs_2NO_3)(NO_3)_2$. The NBO charges on each center reveal that while Cs is positively charged (+0.99e) and Cl is negatively charged with −0.99e. In the hyperhalogen complex, $(Cs_2Cl)(NO_3)_2$ the pattern of NBO charge distribution is also the same. Each NO_3 subunit has −0.9e, and Cs_2Cl has +0.9e NBO charge. The Cs−Cl bond distance is increased from 3.24 to 3.36 Å as expected. This is also true for the N−O distance in NO_3 subunits. The interacting N−O distances increased slightly from 1.26 to 1.27 Å, while the non-interacting N−O decreased to 1.24 Å. From the NBO charge distribution on $(Cs_2Cl)(NO_3)_2$ we note that the charge on Cl remains the same as that in the Cs_2Cl subunit. While Cs centers lose their charge, interacting O centers of NO_3 gain charge compared to the individual charge on O in NO_3. This also suggests that the charge distribution takes place during the formation of the complex. All of the above discussion also holds for Cs_2NO_3 and $(Cs_2NO_3)(NO_3)_2$ complexes. In these clusters the bond lengths and NBO charges behave similarly as in Cs_2Cl and $(Cs_2Cl)(NO_3)_2$ complexes. The VDEs of $(Cs_2Cl)(NO_3)_2$ and $(Cs_2NO_3)(NO_3)_2$ (Table 3-5) are, respectively, 5.13 and 5.22 eV, which are larger than the VDE of individual NO_3, namely, 4.04 eV. Thus, $(Cs_2Cl)(NO_3)_2$ and $(Cs_2NO_3)(NO_3)_2$ complexes are hyperhalogens. We note that the VDE of $Cs(NO_3)_2$ is 4.98 eV, which is also larger than the VDE of NO_3. It is interesting that the VDEs of $(Cs_2Cl)(NO_3)_2$ and $(Cs_2NO_3)−(NO_3)_2$ are even larger than that of $Cs(NO_3)_2$, contrary to the results where BeF_3 and BF_4 served as ligands. The binding energies of both $(Cs_2Cl)(NO_3)_2$ and $(Cs_2NO_3)(NO_3)_2$ are

calculated using the same procedure as described in equation (2), but with appropriate components. The results are given in Table 3-5. We note that these binding energies are significantly higher than those of $(Li_3O)(BF_4)_2$, $(Li_3O)(BeF_3)_2$, and $(Li_3O)(NO_3)_2$.

3.2.3 Conclusion

Our systematic study leads to the following conclusions: (1) Superalkalis such as Li_3O, Cs_2Cl, and Cs_2NO_3 can be used as the core to produce superhalogens. (2) The superalkalis when interacting with superhalogens such as BeF_3, BF_4, and NO_3 can form salts where the cationic and anionic nature of the salt components is preserved. (3) However, when the superalkali cores are ligated with superhalogen moieties, they do not always lead to hyperhalogens. The result depends upon the superhalogen ligand used to form hyperhalogens. For example, (Li_3O)-$(BeF_3)_2$ and $(Li_3O)(BF_4)_2$ do not form hyperhalogens, while $(Li_3O)(NO_3)_2$, $(Cs_2Cl)(NO_3)_2$, and $(Cs_2NO_3)(NO_3)_2$ do. Although superalkalis, because of their low ionization potential, are better candidates to release their electron than an alkali atom, the salt they form has a smaller binding energy than conventional salts because their large size increases the distance between the cation and anion centers. This finding can have potential impact on the design of cathodes in batteries where the release of the cation with less energy is desirable.

3.3 Clusters mimicking the chemistry of catalysts

3.3.1 Introduction

Of the 90 elements in the periodic table that occur in nature, some are highly abundant like Si while some others are scarce or expensive. Among the latter category are elements such as Ga, As, Se, Cd, In, and Te that are 4−8 orders of magnitude less abundant than Si. Similarly,

elements such as Pd and Pt that serve as catalysts, and rare earth elements that form the essential components of magnets, are expensive. Since these elements are critical to technology and society, it will be ideal to find ways in which they can be replaced by earth-abundant elements. This is where atomic clusters may be useful if they can be designed, with suitable size and composition, to mimic the chemistry of scarce or expensive elements.

Recently Castleman and coworkers[84] have expanded this concept to more technologically relevant transition metal elements. Carrying out photoelectron spectroscopy experiment of negatively charged ions of group 10 elements, namely, Ni^-, Pd^-, and Pt^- which are well known for their catalytic properties, the above authors showed that the electronic properties of these atoms are very similar to diatomic molecules, TiO^-, ZrO^- and WC^-, respectively. To illustrate this result, we note that the electronic configurations of Pd, Zr and O are [Kr] $4d^{10}$, [Kr] $5s^2$ $4d^2$ and [He] $2s^2$ $2p^4$, respectively. Thus, Pd is isoelectronic with ZrO. In a similar vein Ni and Pt are isoelectronic with TiO and WC, respectively. Note that in an earlier work, Boudart and coworkers[85] had reported that the surface of WC exhibited similar catalytic behavior as that of Pt. Thus, ZrO could be considered as a superatom mimicking the chemistry of Pd. This is an important result if this analogy could persist in clusters since reduction of extremely active NO by CO is known to take place[86] in the presence of highly dispersed Pd clusters supported on alumina. In a later perspective article, Castleman[87] has reiterated this point. A recent study[88] of the interaction of hydrocarbons such as ethane and propane with Pd^+ cation shows some encouraging results − the reactivity pattern between positively charged Pd and ZrO diatomic species is found to be similar.

We note that the properties of bulk ZrO are very different from that of Pd; while the former is a semiconductor the latter is a metal. However, one knows that at the nano-scale matter

does behave differently than from its bulk. Is this the case with ZrO and Pd nano-clusters? Since catalysts are rarely single atoms and are usually supported on a substrate, fundamental questions that now need to be answered are whether Pd_n clusters react the same way as $(ZrO)_n$ clusters do with simple gas molecules such as H_2, O_2, and CO. How do the reactions with gas molecules differ when these clusters are supported on different substrates?

In the present study, we have attempted to answer these questions. First, we have calculated the atomic structures of Pd_n and $(ZrO)_n$ clusters for $n = 1 - 5$ in neutral, cationic, and anionic forms. The electronic structures of these clusters were analyzed by computing their ionization potentials, electron affinities, binding energies, and hardness. Reactions of H_2, O_2, and CO with these clusters both in neutral and charged forms were carried out to determine their adsorption energies, atomic, and electronic structures. We realize that when clusters are supported on a substrate, charge exchange may occur, leaving the supported clusters in positively or negatively charged state. Thus, studies of the reaction of charged clusters may illustrate qualitatively the role of the support. For a quantitative understanding of the catalytic properties of supported clusters, however, explicit account of the substrate needs to be taken into account. This is a goal of future projects. The choice of the above gas molecules for exploring the catalytic properties of Pd_n and isoelectronic $(ZrO)_n$ clusters is dictated by the importance of chemical reactions such as hydrogenation and dehydrogenation[89, 90] and CO-oxidation[91]. For example, an anode material formed by combining Pd with Pt has been found to be resistant to CO poisoning[92, 93] in fuel cell applications.

The computational details used in this study are described in section 2.9 of Chapter 2. Results are presented in Section 3.3.2 which is divided into two parts. First, the structural and electronic properties of Pd_n and $(ZrO)_n$ (for $n = 1 - 5$) are presented. Second, the interactions

of the gas molecules (H_2, O_2 and CO) with small neutral and charged clusters of Pd_n and $(ZrO)_n$ ($n = 1 - 3$) are discussed. Section 3.3.3 provides a summary of our conclusions.

3.3.2 Results and Discussions

3.3.2.1 Comparison between Pd_n and $(ZrO)_n$ clusters ($n = 1 - 5$):

We begin with a discussion of the geometries and electronic structure of bare Pd_n and $(ZrO)_n$ ($n = 2 - 5$) clusters to see whether they both exhibit similar chemistry. To gain this insight, we have calculated electron affinity (EA), vertical ionization potential (IP), hardness (η), and binding energy (E_b) of these clusters. We defined these parameters (i.e EA, IP, η) in section 2.9 of Chapter 2. The binding energies, E_b of the bare clusters are calculated as:

$$E_b(X_n) = [nE(X) - E(X_n)], \quad (1)$$

where $E(X)$ and $E(X_n)$ (X=Pd, ZrO) represent the total energies of X and X_n species .
In Figure 3-15, we compare their ground state geometries. Corresponding values of EA, IP, η, and E_b are given in Table 3-6 and compared with available experimental data.

The geometries of Pd_n clusters become three-dimensional at $n = 4$ and agree with earlier work[94,95,96]. $(ZrO)_n$ clusters, on the other hand, become three-dimensional from $n = 2$. In addition, geometries of $(ZrO)_n$ clusters are marked by both Zr−O and Zr −Zr bonds. We note that the ground state spin multiplicities of all Pd_n clusters studied are triplet. The EAs of Pd_n clusters, with the exception of Pd_3, agree with experiment within 0.3 eV. This sets the limit on the accuracy of the DFT/B3LYP level of theory. The ionization potentials and hardness of Pd_n clusters decrease steadily with cluster size, reaching a value of respectively 6.81 eV, and 5.09 eV for Pd_5. The results for $(ZrO)_n$ clusters are rather different, both in magnitude as well as in trend. The geometries of $(ZrO)_n$ clusters show no O−O bonds and each O atom is bound to two Zr

atoms. This is because the binding energy of ZrO is 7.4 eV while that of O_2 is 5.21 eV. Unlike Pd_n clusters, the spin multiplicities are singlet for $(ZrO)_n$ ($n = 4, 5$) and triplet for $n = 2, 3$. The electron affinities of $(ZrO)_n$ clusters quantitatively differ from those of Pd_n clusters. The variation with size, however, does not differ significantly. Similar to the Pd_n clusters, the hardness of $(ZrO)_n$ clusters decrease with cluster size, but their magnitudes are significantly smaller. Since EA, IP, and η all influence the interaction of clusters with gas molecules, it would appear that these two sets of clusters will not exhibit similar chemical properties as their size grows. This is indeed the case as we will see in the next section where we discuss the actual reactions with gas molecules.

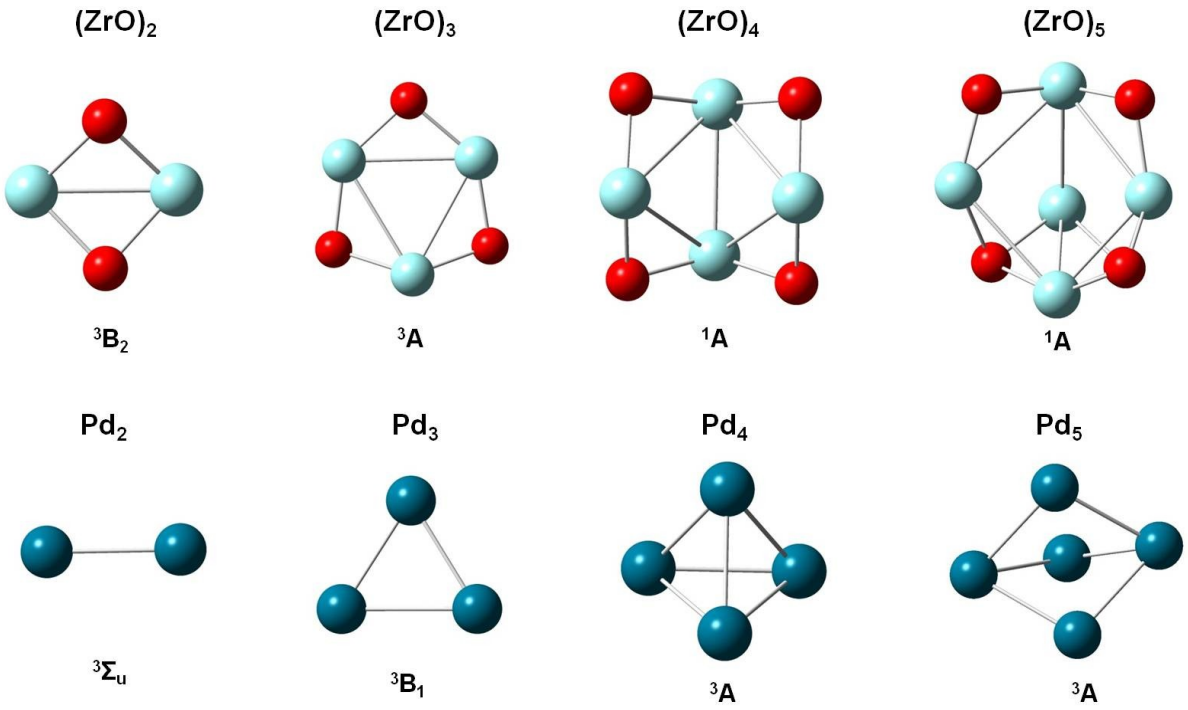

Figure 3-15: Ground state geometries with electronic state of neutral $(ZrO)_n$ and Pd_n (n = 2-5) clusters.

Table 3-6: Electron Affinity (EA), Vertical Ionization Potential (IP), Hardness (η) and Binding Energy (E_b) of $(ZrO)_n$ and Pd_n clusters where $n = 1 - 5$. Available experimental results are given in parentheses.

Cluster	EA(eV)	IP(eV)	η = IP-EA(eV)	E_b (eV)
ZrO	1.29 (expt:1.3±0.3)[97]	7.49	6.20	
$(ZrO)_2$ ***C_{2v}***	1.18	5.70	4.52	3.17
$(ZrO)_3$ ***C_1***	1.20	5.52	4.32	7.38
$(ZrO)_4$ ***C_1***	1.33	5.64	4.31	12.31
$(ZrO)_5$ ***C_1***	1.76	4.96	3.20	15.91
Pd	0.78 (expt: 0.562±0.005, 0.557±0.008)[98]	8.70 (exp: 8.3365±0.0001, 8.3369±0.0001)[99,100]	7.92	
Pd_2 ***D_{infv}***	1.53 (expt:1.685±0.008, 1.30±0.15)[101,102]	7.63 (exp: 7.7±0.3)[99,100]	6.10	0.90 (expt:0.74±0.26)[103]
Pd_3 ***C_{2v}***	2.13 (expt: 1.35±0.10, 1.50±0.10)[100,104]	7.67	5.54	2.45
Pd_4 ***C_1***	1.51 (expt:1.35±0.10)[100]	6.91	5.40	4.83
Pd_5 ***C_1***	1.72 (expt: 1.45±0.10)[100]	6.81	5.09	6.34

3.3.2.2 Interaction of gas molecules (H_2, O_2 and CO) with neutral Pd_n and $(ZrO)_n$ clusters ($n= 1-3$)

In this section we study the reactivity of simple gas molecules such as H_2, O_2 and CO with neutral Pd_n and $(ZrO)_n$ (for $n = 1 - 3$) clusters in order to compare the chemical behavior of these systems. Different initial geometries are considered where the gas molecules binding to Pd_n and $(ZrO)_n$ (where $n = 1 - 3$) are taken in both molecular and dissociated form.

The adsorption energy E_{ads} of a gas molecule is calculated as:

$$E_{ads} = -\{ E[X_nY]^q - [E(X_n^q) + E(Y)]\}, \quad (2)$$

where Y= H_2, O_2, CO and $q = 0, -1, +1$ represent the neutral, anionic and cationic clusters of X_n, respectively. Note that the energies in equation (2) correspond to the preferred spin multiplicities of the parent and the products.

These energies are given in Table 3−7. The reactivity of these gas molecules with the anionic and cationic Pd_n and $(ZrO)_n$ clusters will be discussed in subsequent sections. To assess the accuracy of our computational approach we have calculated the binding energies (bond lengths) of H_2, O_2, and CO which are, respectively, 4.77 eV (0.74 Å), 5.21 eV (1.21 Å), and 12.73 eV (1.13 Å). These agree well with corresponding experimental values, namely 4.48 eV[105] (0.73 Å[105]), 5.12[106] eV (1.21 Å [107]), and 11.10 eV[108] (1.128 Å[109]).

(i) Interaction with H_2

The calculated ground state geometries of H_2 interacting with neutral Pd_n and $(ZrO)_n$ clusters are given in Figure 3-16. We note that hydrogen binds to Pd in quasi-molecular form with a H-H bond length of 0.86 Å which is slightly larger than the corresponding bond length of 0.74 Å in isolated H_2 molecule. H atoms remain almost neutral with a charge of $-0.02e$ on each. The adsorption energy of H_2 to Pd atom is 0.75 eV (see Table 3−7). Our computed

structure of PdH_2 and adsorption energy of H_2 agrees well with previous theoretical calculations[110,111].

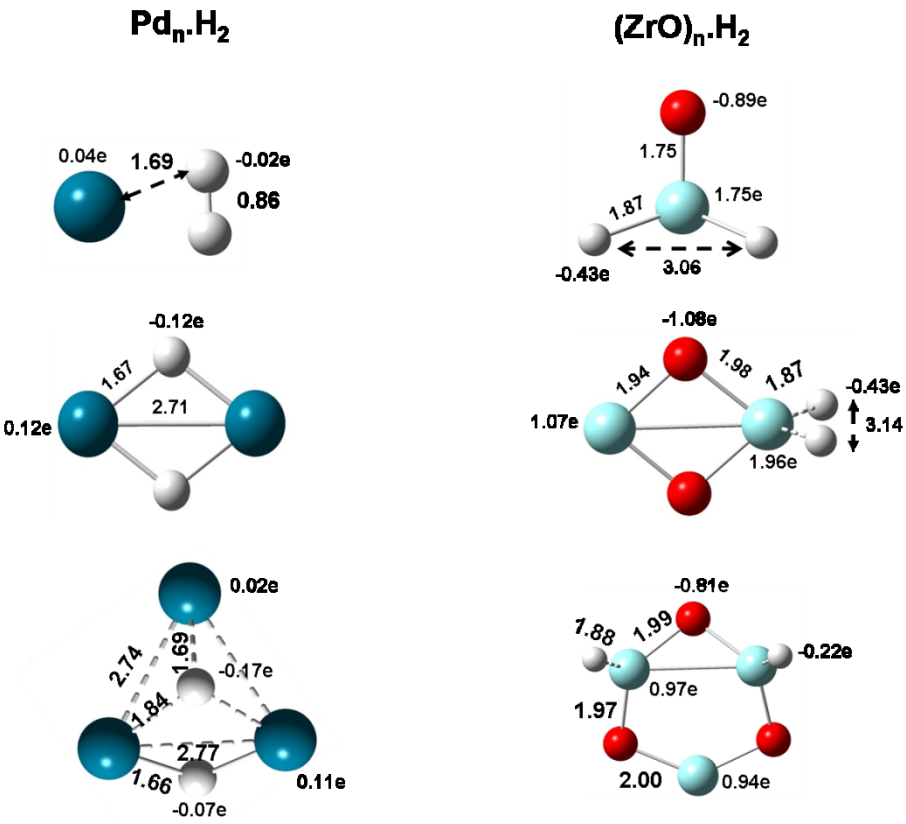

Figure 3-16: Ground state geometries of H_2 interacting with neutral Pd_n and $(ZrO)_n$ clusters. The bond lengths are given in Å and the NBO charges are given in units of electron charge, e.

We note that the above adsorption energy is significantly larger than the physisorption energy of H_2, namely, 0.21 eV/H_2 on Pd(111)[112]. The interaction of H_2 with ZrO is qualitatively different. Here the H-H bond breaks and both the H atoms bind to Zr with each carrying a charge of $-0.43e$. The corresponding adsorption energy is 1.28 eV. This result at first may seem surprising since the adsorption energies of PdH and ZrH are 2.51 eV and 2.37 eV, respectively.

The difference originates from the electronic structure of Pd and Zr atom. Pd atom has outer electronic configuration of $d^{10}s^0$ while that of Zr is $d^2\ s^2$. Since both H_2 and Pd atom have closed electronic shells, the interaction between them is weak and H_2 binds quasi-molecularly. This kind of bonding of H_2 with transition metal atoms has also been demonstrated by Kubas[113,114]. The structure of $ZrOH_2$ where H_2 binds molecularly to the Zr-site is 1.14 eV higher in energy (see Figure II2 in the Appendix). In the Pd_2H_2 cluster, the H-H bond breaks and the adsorption energy more than doubles to 1.64 eV. This result agrees well with that of Zeng *et al*[105] and Efremenko *et al*[115]. However, Cui *et al*[116] reported a ground state structure with a H-Pd-Pd-H dihedral angle of 168.5^0. We found this structure to have an imaginary frequency and automatically led to the structure given in Figure 3-16. The structure of the anioinic Pd_2H_2 shown later in Figure 3-22 is, however, similar to the one reported by Cui *et al* for neutral Pd_2H_2. In $(ZrO)_2H_2$ cluster, the H−H bond also breaks, but both the H atoms remain bound to only one of the Zr atoms. The geometry of $(ZrO)_2H_2$, where the H-atoms bound to two different Zr atoms, is 0.19 eV higher in energy (as shown in Figure II4 in the Appendix) than the ground state (as shown in Figure 3-16).The corresponding adsorption energy increases from 1.28 eV in $(ZrO)H_2$ to 2.09 eV in $(ZrO)_2H_2$. In Pd_3H_2, the H_2 molecule dissociates with one H atom being bridge bonded to two Pd atoms while the other binds on the hollow site formed by three Pd atoms. Zeng *et al*[105] and Cui *et al*[117] had found that in the ground state of Pd_3H_2 each H-atom prefers to bind to the bridge sites. We find this isomer to be nearly degenerate (~0.02 eV) in energy (see Figure II5 in the Appendix) with the one shown in Figure 3-16. In the $(ZrO)_3H_2$, the H atoms bind to separate Zr atoms. The H-atoms binding to single Zr atom is found to be nearly degenerate (~0.06 eV) in energy, which is shown in Figure II6 in the Appendix. The difference between adsorption energies of H_2 to Pd_3 and $(ZrO)_3$ narrows to 0.31 eV, with binding to $(ZrO)_3$

being stronger than that to Pd_3. We note that in $(ZrO)_n$ clusters, the H atom always prefers to bind to Zr and not to O atoms, even though the O-H binding energy is 4.59 eV while that of Zr−H is 2.37 eV. This is because the Zr−O binding energy, as mentioned before, is substantially large, namely 7.4 eV. Thus, ZrO binding will be compromised if H atoms were to bind to O.

(ii) Interaction with O_2

The interaction of O_2 with Pd_n is very different from that to $(ZrO)_n$ clusters. In Figure 3-17, we plot these geometries for $n = 1 - 3$.

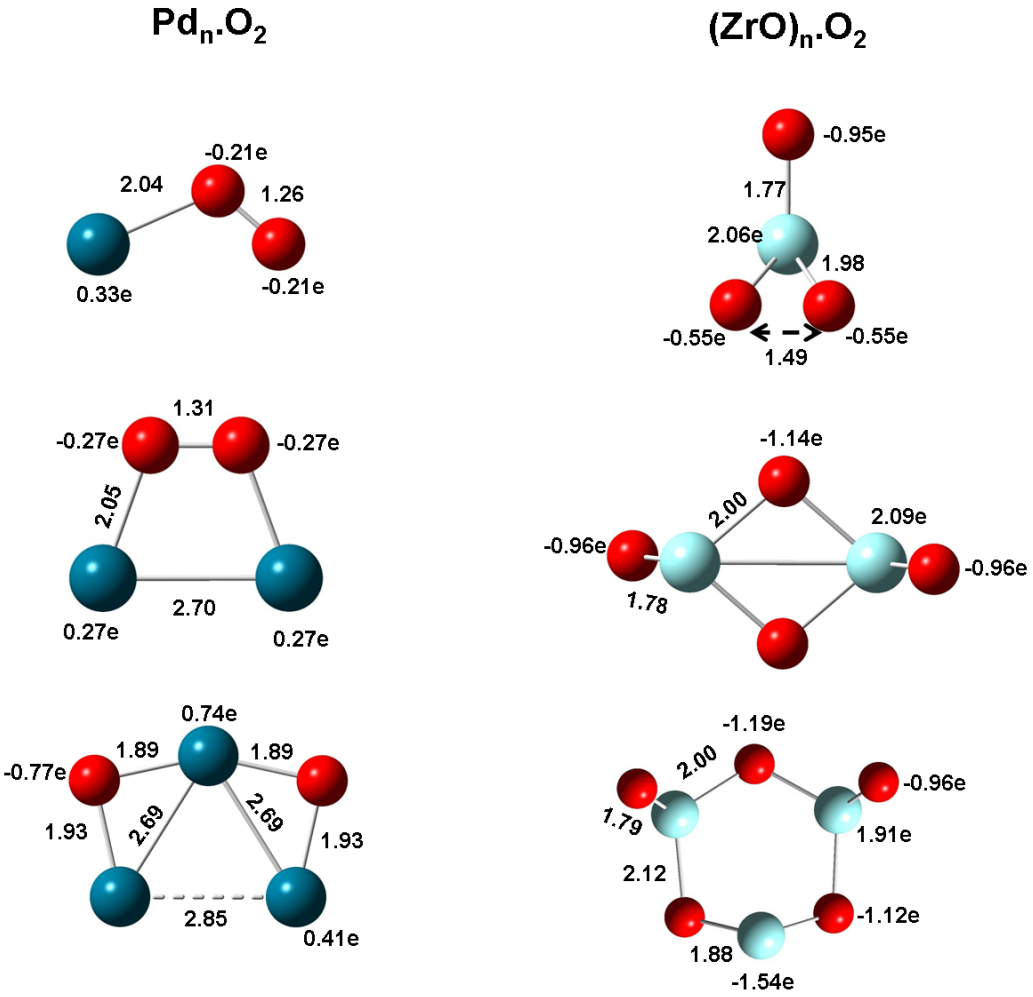

Figure 3-17: Ground state geometries of O_2 interacting with neutral Pd_n and $(ZrO)_n$ clusters. The bond lengths are given in Å and the NBO charges are given in units of electron charge, e.

The corresponding adsorption energies of O_2 as well as spin multiplicities are given in Table 3−7. Oxygen binds quasi-molecularly to Pd in *superoxo* form. The O-O bond in PdO_2 is 1.26 Å which is slightly elongated compared to that in isolated O_2 molecule, namely 1.21 Å. The charge on each of the O atom is −0.21e. Our computed structure and adsorption energy of PdO_2 agree well with previous theoretical calculations[118]. The structure of PdO_2 where the O−O bond breaks is found to be 1.33 eV higher in energy (see Figure II1 in Appendix). The reason O−O bond remains nearly molecular can be seen by comparing the binding energy of PdO and O_2 dimers which are 2.35 eV and 5.21 eV, respectively. However, in $(ZrO)O_2$, oxygen binds in the *peroxo* form with the O-O bond stretched to 1.49 Å with each O atom carrying a charge of -0.55e. This is because of the large binding energy of ZrO, as pointed out before. The adsorption energies of O_2 to Pd and ZrO are, respectively, 0.64 eV and 3.76 eV. In addition, while PdO_2 is a spin triplet, $(ZrO)O_2$ is a spin singlet. The difference in the interaction with O_2 persists in larger Pd_n and $(ZrO)_n$ clusters. In Pd_2O_2 cluster, oxygen continues to bind in a quasi−molecular form where the two O atoms are 1.31 Å apart and the charge on each of the O atom is -0.27e. The ground state reported by Huber *et al*[118] has the O-atoms sitting on the Pd-Pd bridge-sites. We find this structure to be ~0.57 eV higher in energy than the geometry given in Figure 3-17 (see Figure II3 in Appendix). In the $(ZrO)_2O_2$ cluster, on the other hand, the O_2 molecule dissociates and the O atoms, with each carrying a charge of −0.96e, bind to the two Zr atoms. This result is also reflected in their adsorption energies. While O_2 is bound to Pd_2 with 1.07 eV, it is substantially larger in $(ZrO)_2$, namely, 9.20 eV. In both Pd_3O_2 and $(ZrO)_3O_2$ clusters, the O_2 molecule breaks. However, the difference in adsorption energy persists. The adsorption energy of O_2 to Pd_3 is 1.57 eV while that to $(ZrO)_3$ is 8.77 eV. The reason why O_2 is bound much more strongly on $(ZrO)_n$

than Pd_n is because the binding energy of ZrO, namely, 7.4 eV is much higher than that of PdO, namely 2.35 eV.

(iii) Interaction with CO

The equilibrium geometries of Pd_n and $(ZrO)_n$ clusters interacting with CO are given in Figure 3-17. The corresponding adsorption energies are given in Table 3-7.

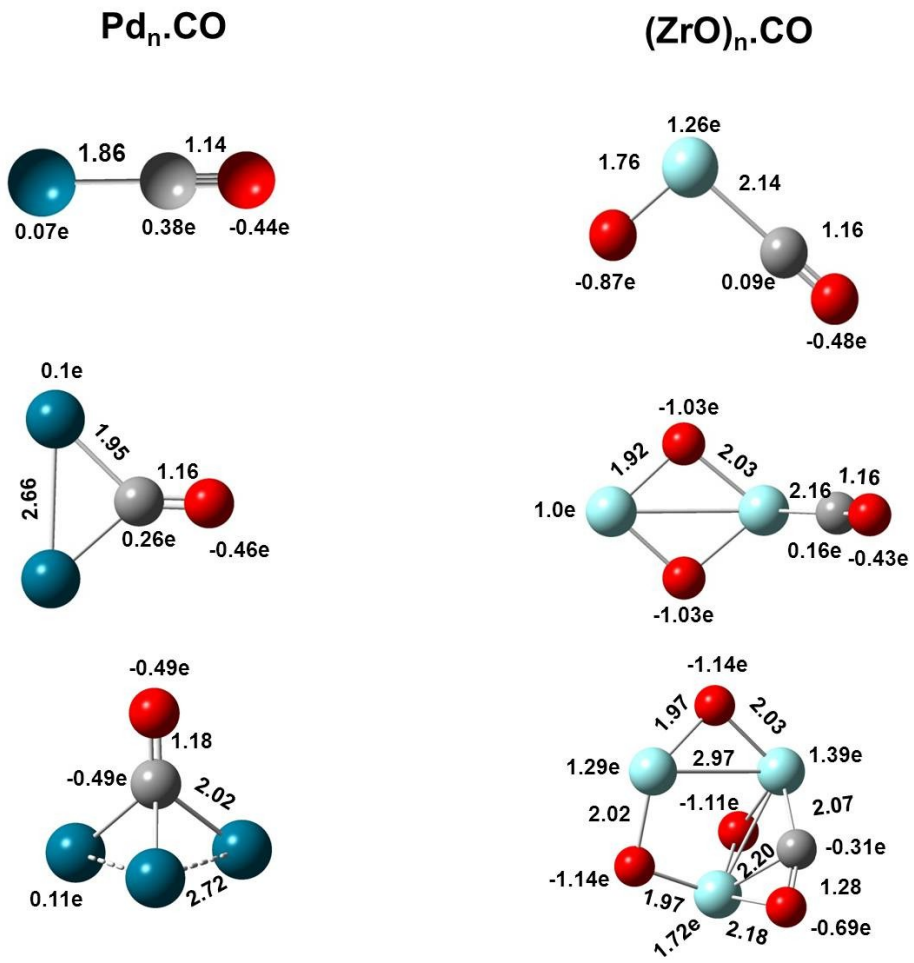

Figure 3-18: Ground state geometries of CO interacting with neutral Pd_n and $(ZrO)_n$ clusters. The bond lengths are given in Å and the NBO charges are given in units of electron charge, e.

Table 3-7: Adsorption energies (E_{ads}) in eV and electronic states in parentheses of neutral Pd_n and $(ZrO)_n$ $(n = 1 - 3)$ clusters interacting with H_2, O_2 and CO.

Cluster	E_{ads} (eV)		
	H_2	**O_2**	**CO**
ZrO	1.28 (^{1}A)	3.76 (^{1}A)	0.50 (^{1}A)
Pd	0.75 (^{1}A')	0.64 (^{3}A")	1.79 (^{1}A)
$(ZrO)_2$	2.09 (^{1}A)	9.20 (^{1}A)	1.27 (^{3}A)
$(Pd)_2$	1.64 (^{1}A')	1.07 (^{3}A)	2.53 (^{1}A)
$(ZrO)_3$	1.78 (^{3}A)	8.77 (^{1}A)	2.00 (^{3}A)
$(Pd)_3$	1.47 (^{1}A)	1.57 ($^3A_2$)	2.51 (^{1}A')

In the case of Pd and ZrO, the CO binds molecularly with the C atom attached to the metal atom. Unlike the case with H_2 or O_2, the adsorption energy of CO to Pd_n is higher than that to $(ZrO)_n$. In Pd_2CO, the CO binds molecularly with C atom attached to both the Pd atoms. The geometry where C−O bond breaks is energetically unfavorable (see Appendix II). Our computed structures and adsorption energies of PdCO and Pd_2CO agree well with previous theoretical calculations[119,120]. In $(ZrO)_2CO$, however, the CO binds to one of the Zr atoms. The adsorption energies of CO to Pd and Pd_2 are about 1.29 eV and 1.26 eV larger than those of ZrO and $(ZrO)_2$, respectively. In Pd_3CO, only the C atom of CO binds to all the Pd atoms, while both the C and O atoms of CO bind to two different Zr atoms in $(ZrO)_3$ cluster. This makes the C-O bond stretch significantly, thereby increasing the adsorption energy of CO to $(ZrO)_3$. The structure where CO binds molecularly to single Zr−site is found to be 0.68 eV higher in energy (see Figure II6 in the Appendix). The adsorption energy of CO to Pd_3 is also 0.51 eV higher than that to $(ZrO)_3$. The reason why CO remains molecular in all the Pd_n and $(ZrO)_n$ clusters is due to the very large

binding energy of CO mentioned earlier, namely, 12.73 eV. The binding energies of CO to Pd_n clusters are larger than those of $(ZrO)_n$ clusters because C binds more to Pd atoms than Zr atoms. In a similar vein, the reason for C in CO preferring to bind to Zr instead of O is not to disrupt the very significant ZrO bonding.

3.3.2.3 Interaction of gas molecules (H_2, O_2 and CO) with cationic Pd_n and $(ZrO)_n$ clusters ($n = 1 - 3$)

We now present the results of Pd^+_n and $(ZrO)^+_n$ clusters interacting with H_2, O_2, and CO.

(i) Interaction with H_2

The equlibrium geometries of Pd^+_n and $(ZrO)^+_n$ clusters interacting with H_2 are plotted in Figure 3-19. The corresponding adsorption energies are given in Table 3-8. H-atoms bind quasi-molecularly with both Pd^+ and ZrO^+ clusters with adsorption energies that are rather similar. Note that these results are consistent with the polarization model described by Niu *et al*[121] where the electric field produced by a metal cation polarizes the H_2 molecule and no charge transfer takes places between H and the parent atoms. The bonding patterns of H_2 to both the cationic clusters of Pd_n and $(ZrO)_n$ for $n = 2, 3$ are very similar. Except for $(ZrO)_3^+$, the adsorption energies of H_2 to $(ZrO)_n^+$ are higher than that to Pd_n^+.

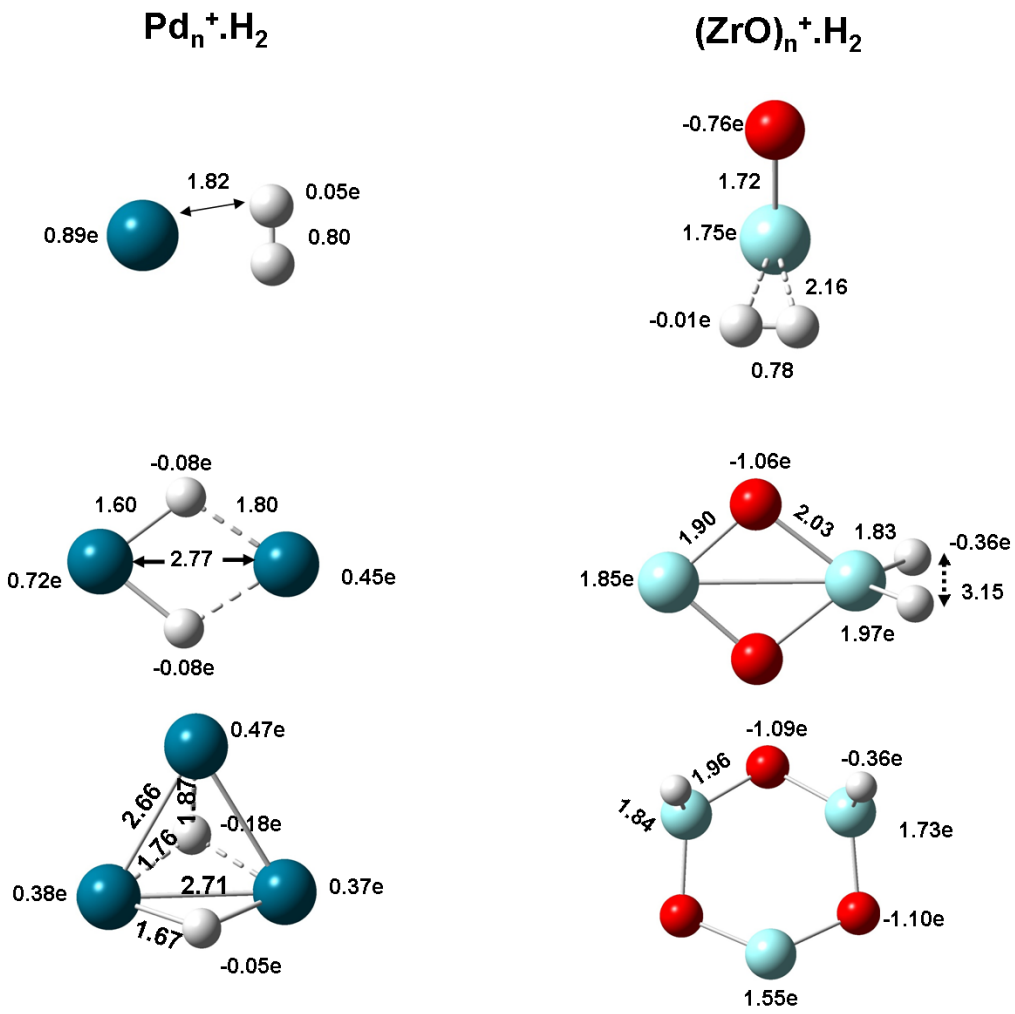

Figure 3-19: Ground state geometries of H_2 interacting with cationic Pd_n and $(ZrO)_n$ clusters. The bond lengths are given in Å and the NBO charges are given in units of electron charge, e.

(ii) Interaction with O_2

In Figure 3-20, we plot the equlibrium geometries of Pd_n^+ and $(ZrO)_n^+$ clusters interacting with O_2. In both Pd^+ and ZrO^+ clusters, O_2 binds molecularly, although the O-O bond in $(ZrO)^+O_2$ is stretched more than that in Pd^+O_2. In addition, O_2 binds in *superoxo* form to Pd^+ while it binds in *peroxo* form to ZrO^+, as seen in the case of corresponding neutral counterparts.

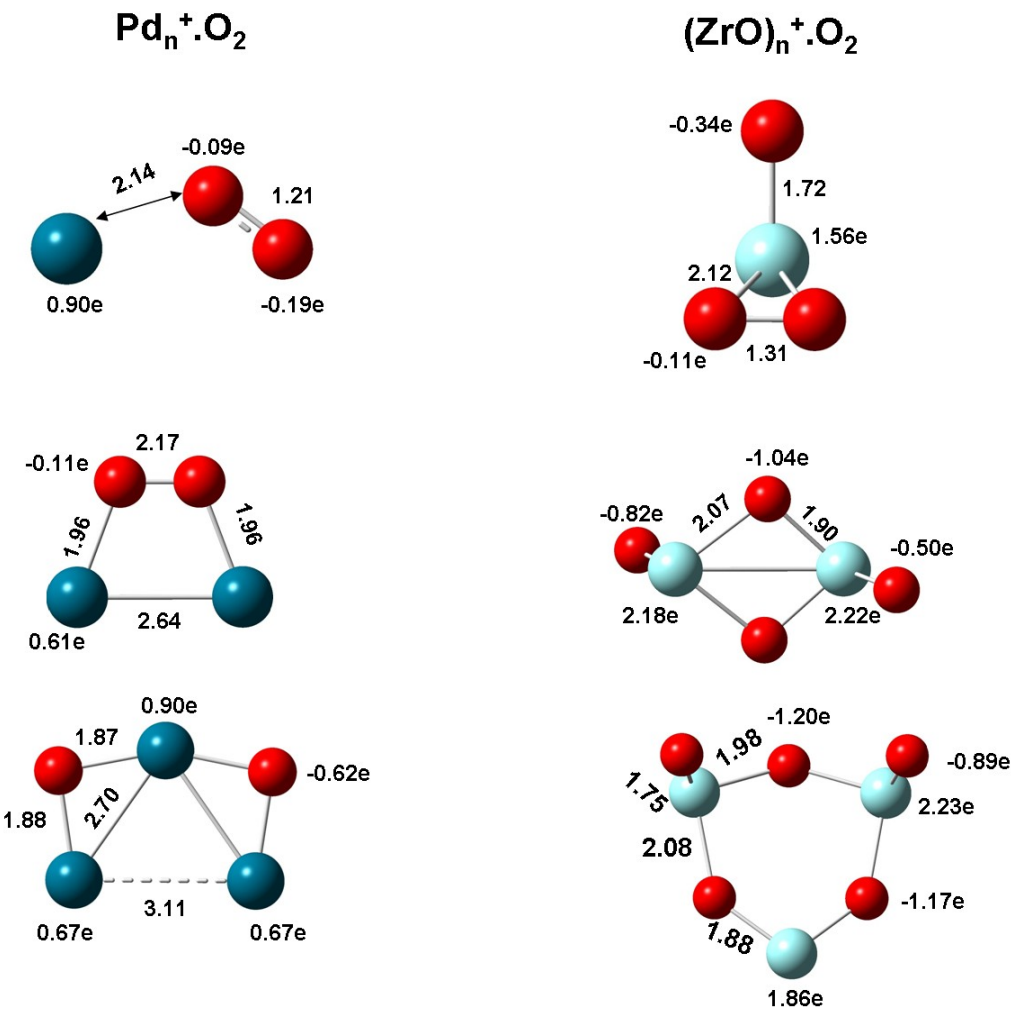

Figure 3-20: Ground state geometries of O_2 interacting with cationic Pd_n and $(ZrO)_n$ clusters. The bond lengths are given in Å and the NBO charges are given in units of electron charge, e.

The adsorption energies of O_2 to $(ZrO)^+$ and $Pd^+$are significantly different; binding to ZrO^+ being about four times larger than that to Pd^+. The bonding pattern of O_2 to Pd_2^+ and $(ZrO)_2^+$ are also different. In $Pd_2^+O_2$, there is significant interaction between the two O atoms, whereas in $(ZrO)_2^+O_2$ both the O-atoms binding to each Zr-site are in the *trans* form. The adsorption energies between O_2 and $(ZrO)_2^+$ is six times larger than that between O_2 and Pd_2^+. The O atoms in $Pd_3^+O_2$ and $(ZrO)_3^+O_2$ are bound dissociatively. However, they are bridge

bonded in $Pd_3^+O_2$ and radially bonded in $(ZrO)_3^+O_2$. The adsorption energy of O_2 to $(ZrO)_3^+$ is about eight times larger than to Pd_3^+.

(iii) Interaction with CO

In Figure 3-21, we plot the equlibrium geometries of Pd_n^+ and $(ZrO)_n^+$ clusters interacting with CO. The adsorption energies of the gas molecules are given in Table 3-8.

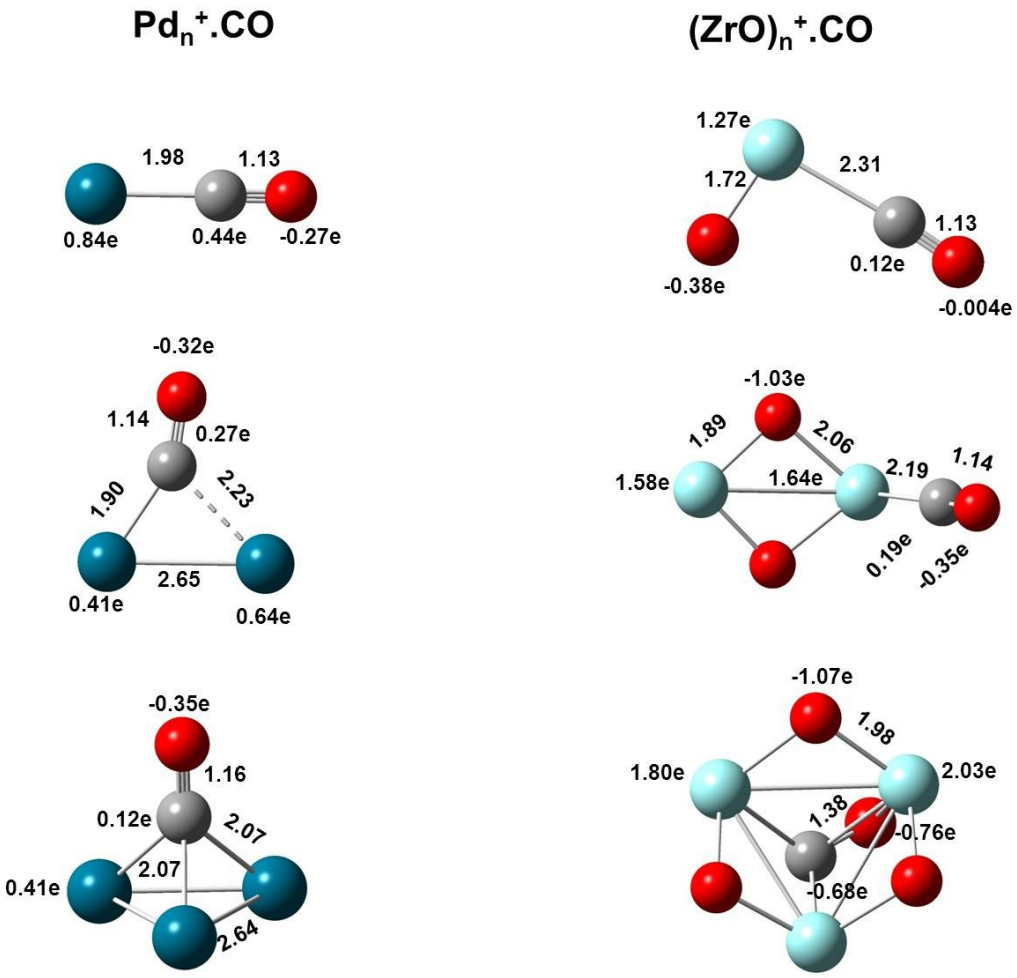

Figure 3-21: Ground state geometries of CO interacting with cationic Pd_n and $(ZrO)_n$ clusters. The bond lengths are given in Å and the NBO charges are given in units of electron charge, e.

In all clusters, CO binds molecularly with the C-atom attached to the metal atom, except for $(ZrO)_3^+$ where both C and O of CO bind to two different Zr atoms (similar to the neutral

counterpart). Here, the C-O bond is stretched by ~0.3 Å. The adsorption energies of CO to Pd_n^+ and $(ZrO)_n^+$ are similar for $n = 1$, but are different for $n = 2, 3$. The spin multiplicities of all these clusters, however, are same.

Table 3-8: Adsorption energies (E_{ads}) in eV and electronic states in parentheses of Pd_n^+ and $(ZrO)_n^+$ ($n = 1 - 3$) clusters interacting with H_2, O_2 and CO.

Cluster	**E_{ads} (eV)**		
	H_2	**O_2**	**CO**
ZrO^+ **Pd^+**	1.02 (^{2}A) 0.85 (^{2}A')	2.93 (^{2}A) 0.72 (^{2}A")	1.75 (^{2}A") 1.76 ($^2\Sigma$)
$(ZrO)_2^+$ **$(Pd)_2^+$**	1.53 (^{2}A) 0.94 ($^2A_1$)	5.98 (^{2}A) 0.99 ($^2A_2$)	1.32 (^{2}A) 1.81 (^{2}A)
$(ZrO)_3^+$ **$(Pd)_3^+$**	1.60 (^{2}A) 1.84 (^{2}A)	8.19 (^{2}A) 1.19 (^{2}A)	2.31(^{2}A) 2.70 (^{2}A)

3.3.2.4 Interaction of gas molecules (H_2, O_2 and CO) with anionic Pd_n and $(ZrO)_n$ clusters ($n = 1 - 3$)

In this section, we present the results of Pd_n^- and $(ZrO)_n^-$ clusters interacting with H_2, O_2, and CO.

(i) Interaction with H_2

The equilibrium geometries of Pd_n^- interacting with H_2 are given in Figure 3-22. H_2 binds dissociatively to both Pd^- and ZrO^-. This is in contrast to H_2 bound to neutral Pd and Pd^+ cation where H_2 binds in quasi-molecular form. In the case of Pd^-, the extra electron can be donated to the antibonding orbital of the H_2 molecule, breaking the H-H bond.

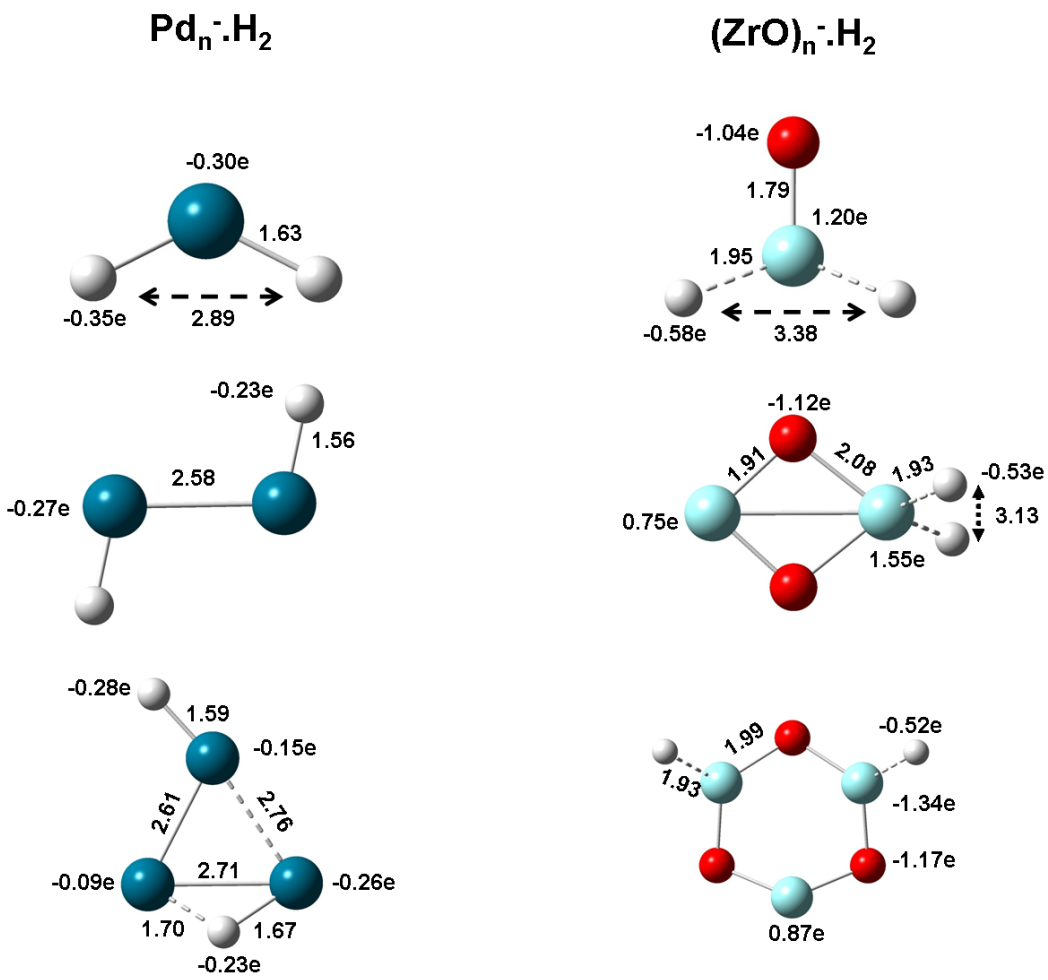

Figure 3-22: Ground state geometries of H_2 interacting with anionic Pd_n and $(ZrO)_n$ clusters. The bond lengths are given in Å and the NBO charges are given in units of electron charge, e.

The adsorption energies of the gas molecules are given in Table 3−9. In Pd_2^- and $(ZrO)_2^-$, H-atoms again bind dissociatively, but they are radially bonded to both the Pd atoms while they bind to a single Zr atom. In Pd_3^- and $(ZrO)_3^-$, hydrogen atoms also bind dissociatively. In $(ZrO)_3^-$ both hydrogen atoms bind radially to the two of the Zr atoms. However, in Pd_3^- one H atom is bridge bonded while the other is radially bonded. In all these clusters, the adsorption

energies of H_2 to $(ZrO)_n^-$ are larger than that to Pd_n^- clusters. Note that the adsorption of H_2 to Pd_3^- is the lowest as compared to its neutral and cationic counterparts.

(ii) Interaction with O_2

The equlibrium geometries and adsorption energies of O_2 to Pd_n^- and $(ZrO)_n^-$ clusters are given in Figure 3-22 and Table 3-9, respectively.

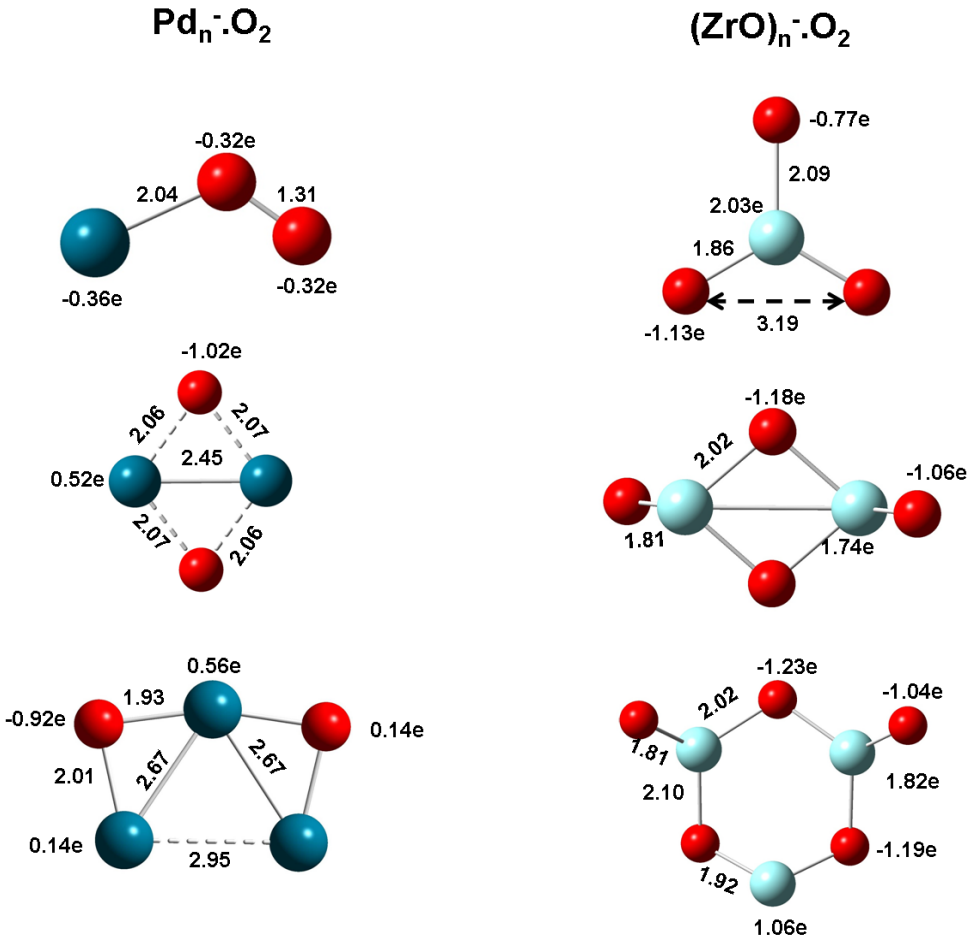

Figure 3-23: Ground state geometries of O_2 interacting with anionic Pd_n and $(ZrO)_n$ clusters. The bond lengths are given in Å and the NBO charges are given in units of electron charge, e.

While O_2 binds in *superoxo* form to Pd^-, it binds dissociatively to ZrO^-. The NBO charge on the O atoms in the *superoxo* form in Pd atom is (−0.32e) while in ZrO, it is (−1.13e) in the

dissociated form. The adsorption energy of O_2 to Pd^- is a factor of four smaller than that to ZrO^-. In Pd_2^- and $(ZrO)_2^-$, the O atoms bind dissociatively, but they are bridge bonded to Pd while they are radially bonded to Zr. The adsorption energy of O_2 to $(ZrO)_2^-$ is more than six times as large as it is to Pd_2^-. In Pd_3^- and $(ZrO)_3^-$, O atoms again bind dissociatively, but they are bridge bonded in Pd_3^- while they are radially bonded in $(ZrO)_3^-$, just as seen in the previous case.

(iii) Interaction with CO

Geometries and adsorption energies of CO interacting with Pd_n^- and $(ZrO)_n^-$ clusters are given in Figure 3-24 and Table 3-9, respectively.

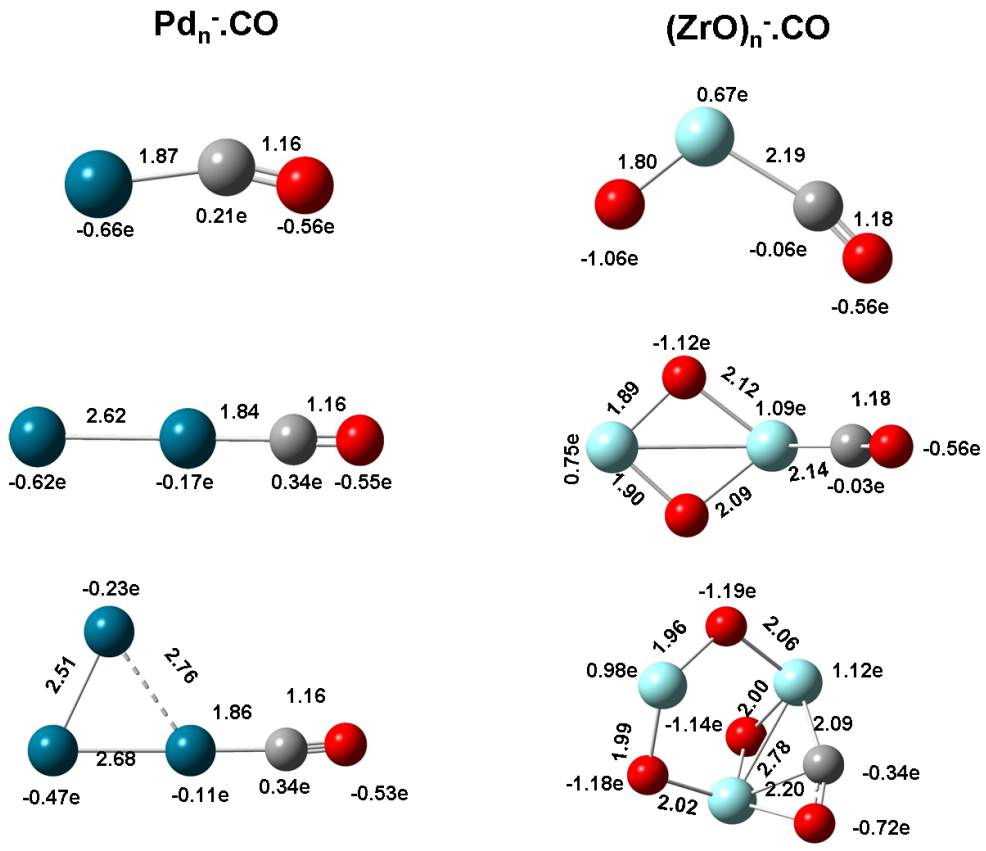

Figure 3-24: Ground state geometries of CO interacting with anionic Pd_n and $(ZrO)_n$ clusters. The bond lengths are given in Å and the NBO charges are given in units of electron charge, e.

In all cases, CO binds molecularly. With the exception of $(ZrO)_3^-$ the C atom is attached to a single metal atom in all clusters. In $(ZrO)_3^-$, the C atom binds to two Zr atoms. The adsorption energies of CO to Pd_n^- are about a factor of two larger than that of $(ZrO)_n^-$ for $n = 1, 2$. However, its adsorption energy to Pd_3^- is smaller than that to $(ZrO)_3^-$.

Table 3-9: Adsorption energies (E_{ads}) in eV and electronic states in parentheses of Pd_n^- and $(ZrO)_n^-$ $(n = 1 - 3)$ clusters interacting with H_2, O_2 and CO.

Cluster	**E_{ads} (eV)**		
	H_2	**O_2**	**CO**
ZrO^-	1.46 (^{2}A)	5.82 (^{2}A)	0.84 (^{4}A''')
Pd^-	0.57 (^{2}A')	1.28 (^{2}A')	1.61 (^{2}A')
$(ZrO)_2^-$	2.08 (^{2}A)	9.71 (^{2}A)	1.29 (^{2}A)
$(Pd)_2^-$	1.19 (^{2}A)	1.54 (^4A_g)	2.40 (^{2}A')
$(ZrO)_3^-$	2.22 (^{4}A)	9.59 (^{2}A')	2.18 (^{2}A)
$(Pd)_3^-$	0.69 (^{2}A)	2.01 (^{4}A)	1.70 (^{2}A)

3.3.3 Conclusion

Using density functional theory, we have calculated the equlibrium geometries, electronic structure, and binding affinity of neutral, cationic, and anionic Pd_n and $(ZrO)_n$ $(n = 1 - 5)$ clusters and their interaction with H_2, O_2, and CO molecules. Our objective was to examine to what extent the chemistry of Pd clusters mimics that of their isoelectronic ZrO clusters. The electronic structure was probed by calculating the ionization potential as well as the electron affinity while the reaction of the gas molecules was studied by examining the nature of their adsorption and corresponding adsorption energies. In general, neither the electronic structure nor the interaction of gas molecules were found to be similar with few exceptions dealing with the

interaction of hydrogen. In particular, we found the interaction of Pd_n with O_2 to be qualitatively different from that between $(ZrO)_n$ and O_2. Thus, our calculations do not support the ansatz put forward by Castleman[84,87,88] and coworkers that ZrO can replace Pd in its function as a catalyst.

References:

[1] Khanna, S. & Jena, P. Atomic Clusters - Building-Blocks for a Class of Solids. *Phys. Rev. B* **51,** 13705–13716 (1995).

[2] Knight, W. *et al.* Electronic Shell Structure and Abundances of Sodium Clusters. *Phys. Rev. Lett.* **52,** 2141–2143 (1984).

[3] R Leuchtner, R., Harms, A. & Castleman, A. Aluminum Cluster Reactions. *J. Chem. Phys.* **94,** 1093–1101 (1991).

[4] Li, X., Wu, H. B., Wang, X. B. & Wang, L. S. s-p hybridization and electron shell structures in aluminum clusters: A photoelectron spectroscopy study. *Phys. Rev. Lett.* **81,** 1909–1912 (1998).

[5] S Khanna, S. & Jena, P. Designing Ionic Solids from Metallic Clusters. *Chem. Phys. Lett.* **219,** 479–483 (1994).

[6] Zheng, W. J., Thomas, O. C., Lippa, T. P., Xu, S. J. & Bowen, K. H. The ionic KAl_{13} molecule: A stepping stone to cluster-assembled materials. *J. Chem. Phys.* **124,** 144304 (2006).

[7] Reveles, J. U., Khanna, S. N., Roach, P. J. & Castleman, A. W. Multiple valence superatoms. *Proc. Natl. Acad. Sci. U. S. A.* **103,** 18405–18410 (2006).

[8] Bergeron, D. E. *et al.* Reactions of $Al_nI_x^-$ with methyl iodide: The enhanced stability of Al_7I and the chemical significance of active centers. *J. Am. Chem. Soc.* **127,** 16048–16053 (2005).

[9] Jena, P., Khanna, S. N. & Rao, B. K. Designing clusters as superelements. *Surf. Rev. Lett.* **3,** 993–999 (1996).

[10] Ashman, C. *et al.* $(BAl_{12})Cs$: A cluster-assembled solid. *Phys. Rev. B* **55,** 15868–15873 (1997).

[11] Rao, B. K., Khanna, S. N. & Jena, P. Designing new materials using atomic clusters. *J. Clust. Sci.* **10,** 477–491 (1999).

[12] Rao, B. K., Khanna, S. N. & Jena, P. Isomers of Al_{13} clusters and their interaction with alkali atoms. *Phys. Rev. B* **62,** 4666–4671 (2000).

[13] Khanna, S. N., Rao, B. K. & Jena, P. Electronic signature of the magicity and ionic bonding in $Al_{13}X$ (X=Li-K) clusters. *Phys. Rev. B* **65,** 125105 (2002).

[14] Ashman, C., Khanna, S. N. & Pederson, M. R. Electron attachment and dynamics of alkali atoms in $Al_{13}X$ (X=Li-Cs) clusters. *Phys. Rev. B* **66,** 193408 (2002).

[15] Castleman, A. W. *et al.* From designer clusters to synthetic crystalline nanoassemblies. *Nano Lett.* **7,** 2734–2741 (2007).

[16] Jadzinsky, P. D., Calero, G., Ackerson, C. J., Bushnell, D. A. & Kornberg, R. D. Structure of a thiol monolayer-protected gold nanoparticle at 1.1 angstrom resolution. *Science* **318,** 430–433 (2007).

[17] Gutsev, G. & Boldyrev, A. Dvm-X-Alpha Calculations on the Ionization-Potentials of $MX^-_{(k+1)}$ Complex Anions and the Electron-Affinities of Mxk+1 Superhalogens. *Chem. Phys.* **56,** 277–283 (1981).

[18] Pyykko, P. & Runeberg, N. Icosahedral WAu_{12}: A predicted closed-shell species, stabilized by aurophilic attraction and relativity and in accord with the 18-electron rule. *Angew. Chem.-Int. Edit.* **41,** 2174–2176 (2002).

[19] Li, X. *et al.* Unexpected stability of Al_4H_6: A borane analog? *Science* **315,** 356–358 (2007).

[20] Knight, D. A. *et al.* Synthesis, Characterization, and Atomistic Modeling of Stabilized Highly Pyrophoric $Al(BH_4)_3$ via the Formation of the Hypersalt $K[Al(BH_4)_4]$. *J. Phys. Chem. C* **117,** 19905–19915 (2013).

[21] Reber, A. C., Khanna, S. N. & Castleman, A. W. Superatom compounds, clusters, and assemblies: Ultra alkali motifs and architectures. *J. Am. Chem. Soc.* **129,** 10189–10194 (2007).

[22] Bartlett, N., Lohmann, D. H. Dioxygenyl Hexafluoroplatinate (V), $O_2^+[PtF_6]^-$. *Proc. Chem. Soc., London.* **3**, 115−116 (1962).

[23] Bartlett, N. Xenon Hexafluoroplatinate (V) $Xe^+[PtF_6]^-$. *Proc. Chem. Soc., London*. **6**, 218 (1962).

[24] Wang, X.-B., Ding, C.-F., Wang, L.-S., Boldyrev, A. I., Simons, J. First Experimental Photoelectron Spectra of Superhalogens and Their Theoretical Interpretations. *J. Chem. Phys.*, **110**, 4763−4771 (1999).

[25] Freza, S. & Skurski, P. Enormously large (approaching 14 eV!) electron binding energies of $[H_nF_{n+1}]^-$ (n=1-5, 7, 9, 12) anions. *Chem. Phys. Lett.* **487,** 19–23 (2010).

[26] Sikorska, C., Skurski, P. The Saturation of the Excess Electron Binding Energy in $Al_nF_{3n+1}^-$ (n=1−5) Anions. *Chem. Phys. Lett.* **536**, 34−38 (2012).

[27] Gutsev, G., Boldyrev, A. The Way to Systems with the Highest Possible Electron Affinity. *Chem. Phys. Lett.* **108**, 250−254 (1984).

[28] Gutsev, G. L., Khanna, S. N., Rao, B. K., and Jena, P., FeO_4: A unique example of a closed-shell cluster mimicking a superhalogen, *Phys. Rev. A* **59**, 3681 (1999).

[29] Gutsev, G. L., Jena, P., Zhai, H. J., Wang, L. S. Electronic Structure of Chromium Oxides, CrO_n^- and CrO_n (n=1−5) from Photoelectron Spectroscopy and Density Functional Theory Calculations. *J. Chem. Phys.* **115**, 7935−7944 (2001).

[30] Boldyrev, A., Simons, J. Vertical and Adiabatical Ionization Potentials of MH_{k+1}^- Anions - Ab-Initio Study of the Structure and Stability of Hypervalent MH_{k+1} Molecules. *J. Chem. Phys.* **99**, 4628−4637 (1993).

[31] Swierszcz, I., Anusiewicz, I. Neutral and Anionic Superhalogen Hydroxides. *Chem. Phys.* **383**, 93−100 (2011).

[32] Smuczynska, S., Skurski, P. Halogenoids as Ligands in Superhalogen Anions. *Inorg. Chem.* **48**, 10231−10238 (2009).

[33] Anusiewicz, I. Electrophilic Substituents as Ligands in Superhalogen Anions. *J. Phys. Chem. A*. **113**, 6511−6516 (2009).

[34] Goetz, M., Willis, M., Kandalam, A. K., Gantefoer, G. F., Jena, P. Origin of the Unusual properties of $Au_n(BO_2)$ Clusters, *ChemPhysChem* **11**, 853−858 (2010).

[35] Pathak, B., Samanta, D., Ahuja, R., Jena, P. Borane Derivatives: A New Class of Super- and Hyperhalogens. *ChemPhysChem* **12**, 2422−2427 (2011).

[36] Marchaj, M., Freza, S., Rybacka, O., Skurski, P. Superhalogen Oxidizers Capable of Ionizing Water Molecules. *Chem. Phys. Lett*. **574**, 13−17(2013).

[37] Sikorska, C., Skurski, P. Moderately Reactive Molecules Forming Stable Ionic Compounds with Superhalogens. *Inorg. Chem*. **50**, 6384−6391 (2011).

[38] Willis, M., Goetz, M., Kandalam, A. K., Gantefoer, G. F., Jena, P. Hyperhalogens: Discovery of a New Class of Highly Electronegative Species. *Angew. Chem., Int. Ed.* 49, 8966−8970 (2010).

[39] Zhai, H.-J., Wang, L.-M., Li, S.-D. & Wang, L.-S. Vibrationally resolved photoelectron spectroscopy of BO^- and BO_2^-: A joint experimental and theoretical study. *J. Phys. Chem. A* **111,** 1030–1035 (2007).

[40] Feng, Y. *et al.* Structures and photoelectron spectroscopy of $Cu^-_n(BO_2)_m^-$ (n, m=1, 2) clusters: Observation of hyperhalogen behavior. *J. Chem. Phys.* **134,** 094309 (2011).

[41] Chen, H. *et al.* Anomalous Property of $Ag(BO_2)_2$ Hyperhalogen: Does Spin-Orbit Coupling Matter? *ChemPhysChem* **14,** 3303–3308 (2013).

[42] Nöth, H., Rurländer, R. Metal Tetrahydridoborates and (Tetrahydroborato)metalates. 10. NMR Study of the Systems AlH/BH/THF and $LiAlH_4/BH_3$/THF. *Inorg. Chem.* **20**, 1062−1072 (1981).

[43] Paduani, C., Wu, M. M., Willis, M., Jena, P. Theoretical Study of the Stability and Electronic Structure of $Al(BH_4)_{n=1\rightarrow4}$ and $Al(BF_4)_{n=1\rightarrow4}$ and Their Hyperhalogen Behavior. *J. Phys. Chem. A* **115**, 10237−10243 (2011).

[44] Farragher, A. L., Page, F. M., Wheeler, R. C. Electron Affinities of the Nitrogen Oxides. Discuss. Faraday Soc. **37**, 203, (1964).

[45] Travers, M., Cowles, D., Ellison, G. Reinvestigation of the Electron Affinities of O^-_2 and NO. *Chem. Phys. Lett.* 164, 449−455 (1989).

[46] Ervin, K.; Ho, J., Lineberger, W. Ultraviolet Photoelectron Spectrum of NO_2^-. *J. Phys. Chem.* **92**, 5405−5412 (1988).

[47] Richards, J. H., Stephens, L. M., Brauman, J. Photodetachment of NO^-_2: Experimental Evidence for a New Isomer. *Chem. Phys. Lett.* **25**, 318−320 (1974).

[48] Hughes, B., Lifshitz, C., Tiernan, T. Electron Affinities from Endothermic Negative-Ion Charge-Transfer Reactions. III. NO, NO_2, SO_2, CS_2, Cl_2, Br_2, I_2, and C_2H. *J. Chem. Phys.* 59, 3162−3181 (1973).

[49] Weaver, A., Arnold, D., Bradforth, S., Neumark, D. Examination of the 2a2′ and 2e″ States of NO_3 by Ultraviolet Photoelectron Spectroscopy of NO_3^-. *J. Chem. Phys.* **94**, 1740−1751 (1991).

[50] Davidson, J., Fehsenfeld, F., Howard, C. Heats of Formation of NO_3^- and NO_3− Association Complexes with HNO_3 and HBR. Int. *J.Chem. Kinet.* **9**, 17−29 (1977).

[51] Andersen, E., Simons, J. Calculation of Electron Detachment Energy of NO_2^-. *J. Chem. Phys.* **66**, 2427−2430 (1977).

[52] Arrington, C. A., Dunning, T. H., Woon, D. E. Electron Affinity of NO. *J. Phys. Chem. A.* **111**, 11185−11188 (2007).

[53] Ko, Y. J., Wang, H.; Pradhan, K., Koirala, P., Kandalam, A. K., Bowen, K. H., Jena, P. Superhalogen Properties of Cu_mCl_n Clusters: Theory and Experiment. *J. Chem. Phys.* **135**, 244312 (2011).

[54] Ko, Y. J. Shakya, A., Wang, H., Grubisic, A., Zheng, W., Goetz, M., Gantefoer, G., Bowen, K. H., Jena, P., Kiran, B. Electronic Structure and Properties of Isoelectronic Magic Clusters: $Al_{13}X$ (X=H, Au, Li, Na, K, Rb, Cs). *J. Chem. Phys.* **133**, 124308 (2010).

[55] Joseph, J., Pradhan, K., Jena, P., Wang, H., Zhang, X., Ko, Y. J., Bowen, K. H. Evolution of Superhalogen Properties in $PtCl_n$ Clusters. *J. Chem. Phys*. **136**, 194305 (2012).

[56] Samanta, D., Wu, M. M., Jena, P. $Au(CN)_n$ Complexes: Superhalogens with Pseudohalogen as Building Blocks. *Inorg. Chem.* **50**, 8918−8925 (2011).

[57] Behera, S., Jena, P. Stability and Spectroscopic Properties of Singly and Doubly Charged Anions. *J. Phys. Chem. A.* **116**, 5604−5617 (2012).

[58] Xu, K. C., Chen, Y. Structural Features of the Congruently Melting Compounds $MLi(NO_3)_2$ (M = K, Rb, Cs) Inferred from Their Raman Spectra. *J. Phys. Chem. Solids* **60**, 317−324 (1999).

[59] Berseth, P. A., Harter, A. G., Zidan, R., Blomqvist, A., Araujo, C. M., Scheicher, R. H., Ahuja, R., Jena, P. Carbon Nanomaterials as Catalysts for Hydrogen Uptake and Release in $NaAlH_4$. *Nano Lett.* **9**, 1501−1505 (2009).

[60] Li, S., Ahuja, R., Araujo, C. M., Johansson, B., Jena, P. Dehydrogenation Associated with Ti Catalyst in Sodium Alanate. *J. Phys. Chem. Solids.* **71**, 1073−1076 (2010).

[61] Gutsev, G. L., Boldyrev, A. I. $DVM X_\alpha$ Calculations on the Electronic Structure of "Superalkali" Cations. *Chem. Phys. Lett.* **92**, 262−266 (1982).

[62] Bengtsson, L., Holmberg, B., Ulvenlund, S. *Inorg. Chem.* **29**, 3615−3618 (1990).

[63] Yokoyama, K., Haketa, N., Tanaka, H., Furukawa, K., Kudo, H. *Chem. Phys. Lett* **330**, 339−346 (2000).

[64] Neskovic, O. M., Veljkovic, M. V., Velickovic, S. R., Petkovska, L. T., Peric-Grujic, A. A. *Rapid Commun. Mass Spectrom*. **17**, 212−214 (2003).

[65] Velickovic, S., Djordjevic, V., Cveticanin, J., Djustebek, J., Veljkovic, M., Neskovic, O. *Rapid Commun. Mass Spectrom.* **20**, 3151−3153 (2006).

[66] Velickovic, S. R., Koteski, V. J., Cavor, J. N. B., Djordjevic, V. R., Cveticanin, J. M., Djustebek, J. B., Veljkovic, M. V., Neskovic, O. M. *Chem. Phys. Lett.* **448**, 151−155 (2007).

[67] Dao, P. D., Peterson, K. I., Castleman, A. W., Jr. *J. Chem. Phys.* **80**, 563−564 (1984).

[68] Goldbach, A., Hensel, F., Rademan, K. *Int. J. Mass Spectrom. Ion Processes* **148**, L5−L9 (1995).

[69] Hampe, O., Koretsky, G. M., Gegenheimer, M., Huber, C., Kappes, M. M., Gauss, J. J. *Chem. Phys.* **107**, 7085−7095 (1997).

[70] Rehm, E., Boldyrev, A. I., Schleyer, P. v. R. *Inorg. Chem.* **31**, 4834−4842 (1992).

[71] Li, Y., Wu, D., Li, Z. R., Sun, C. C. *J. Comput. Chem.* **28**, 1677−1684 (2007).

[72] Tong, J., Li, Y., Wu, D., Wu, Z.-J. Theoretical Study on Polynuclear Superalkali Cations with Various Functional Groups as the Central Core. *Inorg. Chem.* **51**, 6081−6088 (2012).

[73] Hou, N., Li, Y.,Wu, D., Li, Z.-R. Do Nonmetallic Superalkali Cations Exist? *Chem. Phys. Lett.* **575**, 32−35 (2013).

[74] Graudejus, O., Elder, S. H., Lucier, G. M., Shen, C., Bartlett, N. Room Temperature Syntheses of AuF_6^- and PtF_6^- Salts, $Ag^+AuF_6^-$, $Ag_2^+PtF_6^{2-}$, and $Ag_2^+PdF_6^{2-}$, and An Estimate for

E(MF_6^-) [M = Pt, Pd]. *Inorg. Chem*. **38**, 2503−2509 (1999).

[75] Gutsev, G. L., Rao, B. K., Jena, P., Wang, X. B., Wang, L. S. Origin of the Unusual Stability of MnO_4^-. *Chem. Phys. Lett*. **312**, 598−605 (1999).

[76] Gurewitz, E., Melamud, M., Horowitz, A., Shaked, H. Polytypism in $KMnCl_3$, Neutron-Diffraction Study of the Distorted-Perovskite-Structure Compound. *Phys. Rev. B.* **25**, 5220−5229 (1982).

[77] Zintl, E., Morawietz, W. Orthosalze Von Sauerstoffsäuren. *Z. Anorg. Allg. Chem*. **236**, 372−410 (1938).

[78] Jansen, M. Neue Untersuchungen an Na_3NO_3. *Z. Anorg. Allg. Chem.* **435**, 13−20 (1977).

[79] Behera, S., Samanta, D., Jena, P. Nitrate Superhalogens as Building Blocks of Hypersalts. *J. Phys. Chem. A.* **117**, 5428−5434 (2013).

[80] Wang, D., Graham, J. D., Buytendyk, A. M., Bowen, K. H. Photoelectron Spectroscopy of the Molecular Anions Li_3O^- and Na_3O^-. *J. Chem. Phys.* **135**, 164308 (2011).

[81] (a) Rehm, E., Boldyrev, A. I., Schleyer, P. v. R. Ab Initio Study of Superalkalis. First Ionization Potentials and Thermodynamic Stability. *Inorg. Chem.* **31**, 4834−4842 (1992).
(b) Gutsev, G. L., Boldyrev, A. I. The Theoretical Investigation of the Electron Affinity of Chemical Compounds. *Adv. Chem. Phys.* **51**, 169−175 (1985).
(c) Wang, D., Graham, J. D., Buytendyk, A. M.; Bowen, K. H. Photoelectron Spectroscopy of the Molecular Anions Li_3O^- and Na_3O^-. *J. Chem. Phys.* **135**, 164308 (2011).

[82] Paduani, C., Jena, P. A Recipe for Designing Molecules with Ever-Increasing Electron Affinities. *J. Phys. Chem. A*. **116**, 1469−1474 (2012).

[83] Yang, H., Li, Y.; Wu, D., Li, Z.-R. Structural Properties and Nonlinear Optical Responses of Superatom Compounds BF_4^-M (M = Li, FLi_2, OLi_3, NLi_4). *Int. J. Quantum Chem.* **112**, 770−778 (2012).

[84] Peppernick, S.J., Gunaratne, K.D.D., and Castleman, A.W. *Proc. Natl. Acad. Sci.* **107**, 975 (2010).

[85] Levy R. and Boudart, M. *Science* **181**, 547 (1973).

[86] Valden, M., Aaltonen, J., Kuusisto, E., Pessa, M., and Barnes, C. *Surf. Sci*. **307**, 193 (1994).

[87] Castleman, A.W. *J. Phys. Chem. Lett.* **2**, 1062 (2011).

[88] Tyo, E.C. , Castleman, A.W. , Reber, A.C. and Khanna, S.N. *, J. Phys. Chem. C* **115**, 16797 (2011).

[89] Che M. and Bennett, C. *Adv. Catal.* **36**, 55 (1989).

[90] Rather, S., Zacharia, R., Hwang, S.W., Naik, M., and Nahm, K.S., *Chem. Phys. Lett.* **438**, 78 (2007).

[91] Ertl, G. *Adv. Catal.* **213,** 37 (1990).

[92] Carrette, L., Friedrich, K.A. and Stimming, U., *ChemPhysChem* **1**, 162 (2000).

[93] Zhou, W.J., Li, W.Z., Song, S.Q., Zhou, Z.H., Jiang, L.H., Sun, G.Q., Xin, Q., Poulianitis, K., Kontou, S., and Tsiakaras, P., *J. Power Sources* **131**, 217 (2004).

[94] Kalita B. and Deka, R.C. *J. Chem. Phys.* **127**, 244306 (2007).

[95] Rogan, J., Garcia, G., Valdivia, J.A., Orellana, W., Romero, A.H., Ramirez, R., and Kiwi, M. *Phys. Rev. B* **72**, 115421 (2005).

[96] Efremenko I. and Sheintuch, M. *J. Mol. Catal. A-Chem*. **160**, 445 (2000).

[97] Thomas, O.C., Xu, S.J., Lippa, T.P., and Bowen, J K.H. *Clust. Sci.* **10**, 525 (1999).

[98] Hotop H. and Lineberger, W. *J. Phys.* Chem. Ref. Data **14**, 731 (1985).

[99] Lide, D. R. Handbook of Chemistry and Physics, 74th ed. CRC, Boca Raton, FL, 1994.

[100] Gingeric.ka, *Naturwissenschaften* **54**, 43 (1967).

[101] Ho, J., Ervin, K., Polak, M., Gilles, M., and Lineberger, W. *J. Chem. Phys.* **95**, 4845 (1991).

[102] Gantefor, G., Gausa, M., Meiwesbroer, K., and Lutz, H. *J. Chem. Soc.-Faraday Trans*. **86**, 2483 (1990).

[103] Lide, D. R., Handbook of Chemistry and Physics, 76th ed., Ed.; CRC Press: Boca Raton, FL, 1995.

[104] Ervin, K., Ho, J., and Lineberger, W., *J. Chem. Phys*. **89**, 4514 (1988).

[105] Ni M. and Zeng, Z. *Theochem-J. Mol. Struct*. **910**, 14 (2009).

[106] Chase, M. W. NIST-JANAF Thermochemical Tables (American Chemical Society, New York, 1998).

[107] Chieh, C. Bond Lengths and Energies (University of Waterloo, 2007).

[108] deB Darwent, B. Bond dissociation energies in simple molecules (NSRDS-NBS) (Washington, D.C, 1970).

[109] Huber , K.P., Herzberg, G. Molecular Spectra and Molecular Structure, Constants of Diatomic Molecules, vol IV, (Van Nostrand, New York, 1979) p. 154.

[110] Ni M. and Zeng, Z. *Theochem-J. Mol. Struct*. **910**, 14 (2009).

[111] Efremenko, I., German, E.D. and Sheintuch, M. *J. Phys. Chem. A* **104**, 8089 (2000).

[112] Dong W. and Hafner, J. *Phys. Rev. B* **56**, 15396 (1997).

[113] Kubas, G.J. *J. Organomet. Chem*. **635**, 37 (2001).

[114] Kubas, G.J. *J. Organomet. Chem*. **694**, 2648 (2009).

[115] Efremenko, I., German, E.D. and Sheintuch, M., *J. Phys. Chem. A* **104**, 8089 (2000).

[116] Cui, Q., Musaev, D.G. and Morokuma, K. *J. Chem. Phys*. **108**, 8418 (1998).

[117] Cui, Q., Musaev, D.G. and Morokuma, K. *J. Phys. Chem. A* **102**, 6373 (1998).

[118] Huber, B., Hakkinen, H., Landman, U., and Moseler, M. *Comput. Mater. Sci*. **35**, 371 (2006).

[119] Zanti G. and Peeters, D. *Eur. J. Inorg. Chem*. **2009,** 3904 (2009).

[120] Schultz, N.E., Gherman, B.F., Cramer, C.J. and Truhlar, D.G. *Journal of Physical Chemistry B* **110**, 24030 (2006).

[121] Niu, J., Rao, B., and Jena, P. *Phys. Rev. Lett.* **68**, 2277 (1992).

Chapter 4

REACTION OF HYDROGEN WITH COINAGE METAL CLUSTERS

Studies of the interaction of clusters with gas atoms are important for understanding of reaction mechanisms and hence of heterogeneous catalysis[1,2,3]. In recent years, there has been considerable interest in the properties of nanosized coinage metal clusters since they serve as building blocks of novel nanostructured materials[4,5,6,7]. The coinage metal atoms, Cu, Ag and Au occupy a special place at the end of the *3d*, *4d* and *5d* periods, respectively. The *d* shell is filled with 10 electrons and the valence shell contains a single *s*-electron *i.e.*, $nd^{10}ns^{1}$. They are monovalent like alkali metals and possess nearly free-electron character. Many interesting properties of coinage metal clusters arise due to *s-d* hybridization, which is caused by destabilization of the *d* orbitals, leading to a reduction of the *s-d* energy gap and their unique cluster size effects. Although extensive studies have been performed on coinage metals clusters, the mechanisms of various reactions are not fully understood. This is partly due to the absence of spectroscopic evidence in understanding important elementary steps. To shed light on their reaction mechanisms, the gas-phase coinage metal clusters are suitable model systems.

This chapter deals with the interaction of small Cu and Ag clusters with single H-atom forming respective monohydrides. It involves a synergistic study between photoelectron spectroscopy (PES) and density functional theory (DFT). The purpose of this study is to understand their interaction mechanism and to see whether or not by replacing a metal atom by H-atom can change the structural and electronic properties of the bare clusters.

4.1 Interaction mechanism of hydrogen with Cu_n and Ag_n clusters (n=1-5)

4.1.1 Introduction

Fundamental understanding of hydrogen interaction with materials – from clusters and nanostructures to bulk materials is an important topic of considerable current interest[8,9,10]. Depending on the host material hydrogen bonding pattern can change from covalent or ionic[11,12,13] to metallic[14,15,16] or weak. Consequently, H can bind molecularly and become physisorbed or bind dissociatively and get chemisorbed. In bulk metals or on metal surfaces, H_2 molecules usually dissociate and chemisorb. In most of these cases, H draws electrons from the conduction band and remains in an ‘‘anionic’’ form; this in turn creates states several electron volts below the Fermi energy[17,18,19]. The only example of a “cationic” (*proton-like*) hydrogen has been observed in small Au clusters in the gas phase where H mimics an Au atom by donating its *1s* electron to the cluster valence shell[19]. Consequently, the electronic structure of Au_n^- is similar to that of $Au_{n-1}H^-$. This finding fits very well with the gold-hydrogen analogy where the chemical behavior of a H atom corresponds to that of an Au atom[20,21]. The cationic nature of H interacting with Au may be due to the exceptionally large electron affinity of Au, namely 2.3 eV[19], which is the highest among all metals in the periodic table. We note that the other two coinage metals Cu and Ag have electron affinities of 1.2 eV and 1.3 eV, respectively[22]. The

question then arises: Does H interact with Cu and Ag as it does with Au even though their electron affinities are significantly less than that of Au? If so, this would open the door to expanding the gold-hydrogen analogy to coinage metals in general. From a practical point of view, it might offer possibilities for the design of new oxidation catalysts. Theoretically, it has been pointed out that the replacement of an Au atom by H can lead to considerable enhancement in the reactivity of the cluster by lowering the reaction barrier for CO oxidation[23]. Thus, broadening the scope of the gold-hydrogen analogy to coinage metals may help in developing new strategies for replacing expensive noble metal CO oxidation catalysts[24,25] by cheaper and more readily available Cu and Ag catalysts.

In this study, we carried out the computational study of the interactions of an H-atom with Cu_n and Ag_n clusters as a function of *n* (where n=1-5) and compared the results with the photoelectron spectroscopy (PES) experiments performed in Professor Gantefor's group in University of Konstanz, Germany. The computational details (described briefly in section 2.9 of Chapter 2) involves a density functional theory (DFT) study of the equilibrium geometries, electron affinities (EAs) and vertical detachment energies (VDEs) of neutral and anionic clusters. Results of this study are discussed in section 4.1.2, which is divided into two subsections. The first section includes bare Cu clusters and their respective monohydrides, and the second section deals with bare Ag clusters and their respective monohydrides. The final conclusion of this study is summarized in section 4.1.3.

4.1.2 Results and discussions

4.1.2.1 Cu_n and $Cu_{n-1}H$ clusters

In Figure 4-1, we present the PES spectra of Cu^-, Cu_n^-, and $Cu_{n-1}H^-$ (n = 2–5) obtained from experiment. The experimental and calculated VDEs and theoretical EAs are given in Table 4-1.

We note that the agreement between theory and experiment is very good, establishing the accuracy of our computational approach. We begin with the results of Cu^-, CuH^- and Cu_2^- given in Figure 4-1 (left column). Note that the peak A representing the VDE is shifted from 1.3 eV in Cu^- to 0.97 eV in Cu_2^-. If one of the Cu atoms in Cu_2^- is replaced by an H atom and H is assumed to mimic the chemistry of Cu, one would expect the VDE of CuH^- not to change from that of Cu_2^-. This is not the case. As is seen from Figure 4-1 (left column, middle), the VDE of CuH^- is 0.44 eV.

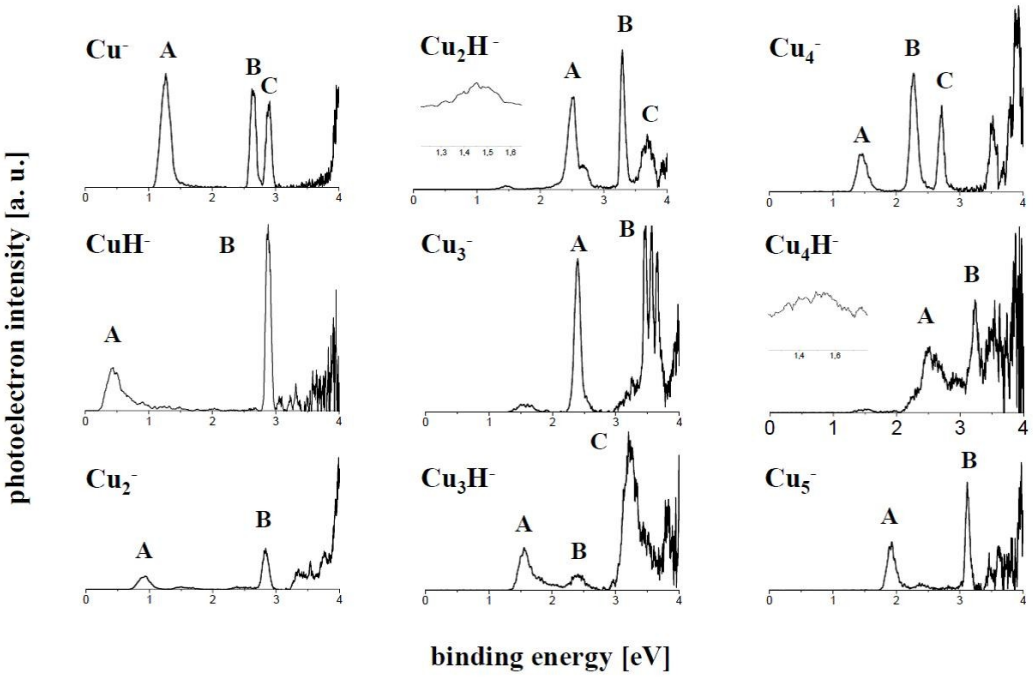

Figure 4-1: Photoelectron spectra of Cu^-, Cu_n^-, and $Cu_{n-1}H^-$ (n = 2–5). The insets in the spectra of Cu_2H^- and Cu_4H^- are an expanded version of the peak found at 1.46 eV and 1.51 eV, respectively.

The corresponding optimized geometries of CuH and Cu_2 along with the bond length and NBO charges are given in Figure 4-2. The extra electron in Cu_2^- is evenly distributed between

two Cu atoms while in CuH^-, two-thirds of the extra electron goes to H. This is a typical behavior of H interacting with metals where H draws electrons from the metal.

Table 4-1: Experimental and theoretical results of vertical detachment energies (VDEs) and theoretical electron affinities (EAs) in eV of Cu_n and $Cu_{n-1}H$.

Cluster	**Expt. VDE of Cu_n^-, $Cu_{n-1}H^-$ (eV)**	**Theo.VDE of Cu_n^-, $Cu_{n-1}H^-$ (eV)**	**Theo. EA of Cu_n, $Cu_{n-1}H$ (eV)**
Cu	1.3	1.21	1.21
Cu_2	0.97	0.89	0.84
CuH	0.44	0.50	0.46
Cu_3	1.56[a]	-	-
	2.40	2.16[c]	2.07
Cu_2H	1.46[a]	1.26[b]	-
	2.52	2.37[c]	2.17
Cu_4	1.45	1.49	1.42
Cu_3H	1.55	1.55	1.51
Cu_5	1.92	1.88	1.83
Cu_4H	1.51[a]	1.73[b]	-
	2.50	2.86[c]	1.97

[a] The maximum of a very flat peak turning up before the first pronounced maximum
[b] The structure corresponding to the neutral species and the anion having nearly similar geometries
[c] The structure corresponding to the ground state of neutral and anion geometries

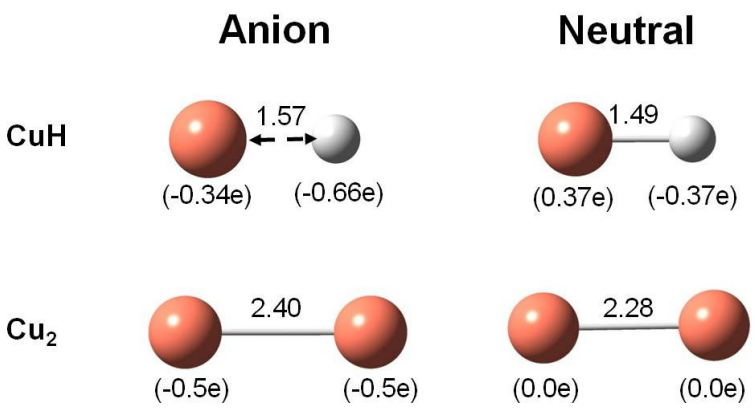

Figure 4-2: Optimized anionic and neutral geometries of CuH and Cu_2. Bond lengths (in Å) and NBO charges (in brackets) are given.

The situation changes in larger clusters. The PE spectrum of Cu_2H^- is compared to that of Cu_3^- in Figure 4-1 (middle row). A small but broad peak is seen around 1.5 eV in both Cu_2H^- and Cu_3^-. Similarly, peak A in Cu_3^- occurring at 2.40 eV nearly coincides with that of Cu_2H^- occurring at 2.52 eV. This similarity shows that the electronic structure of Cu_3^- is not significantly affected by substituting a Cu atom with H, analogous to that observed in the Au–H system. The optimized geometries of the neutral and anionic clusters of Cu_2H and Cu_3 and a higher energy isomer of anionic Cu_2H are given in Figure 4-3. The ground state geometries of neutral Cu_3 and Cu_2H are triangular, although the Cu–Cu bond length in Cu_2H is significantly larger than the corresponding distance in Cu_3. The H atom in neutral Cu_2H bridges the two Cu atoms. The ground state geometries of the anions of these clusters, however, are linear. In Cu_2H^-, the H atom forms a terminal bond with one of the Cu atoms.

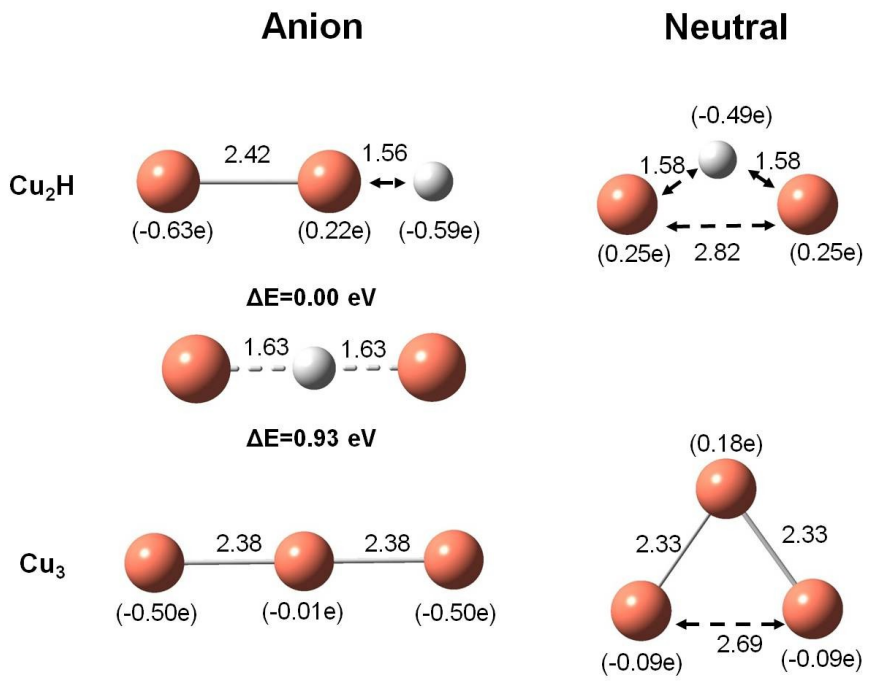

Figure 4-3: Optimized anionic and neutral geometries of Cu_2H and Cu_3. Bond lengths (in Å) and NBO charges (in brackets) are given.

The calculated VDEs associated with the ground state of Cu_3^- and Cu_2H^- are, respectively, 2.16 and 2.37 eV. These agree well with the experimental VDEs of 2.4 and 2.52 eV given in Table 4-1, which corresponds to peak A in Figure 4-1. A linear higher energy isomer with the H-atom inserted between two Cu atoms was found for the Cu_2H^- cluster as shown in Figure 4-3. This isomer lies 0.93 eV higher in energy than its corresponding ground state geometry. The VDE corresponding to this higher energy isomer is 1.26 eV which agrees well with the experimental value of 1.46 eV given in Table 4-1. This peak corresponds to the small broad peak shown in Figure 4-1. The fact that the peak in the PES of Cu_2H^- at 1.46 eV is rather weak compared to the dominant peak A suggests that, this high energy isomer is much less likely to form compared to the ground state structure. No higher energy isomer for Cu_3^- was found. As a matter of fact, the geometry optimization of Cu_3^- always led to the linear structure irrespective of the starting

geometry. Thus, the broad peak at 1.56 eV observed in the PES experiment for Cu_3^- remains unresolved. In the neutral Cu_2H, the charge on the H atom is -0.49e while that on the Cu atom at the apex is +0.18e. This is typical of H in metals. As an extra electron is added, the charge on the H atom remains essentially unchanged, while the Cu atoms share the added electron. The charge distribution among atoms in Cu_3^- and Cu_2H^- is rather similar and based upon the agreement between the PES in Figure 4-1 and from the NBO charge distribution one can argue that the electronic structure is not significantly affected by replacing a Cu atom with H. However, this is not the case in the neutral clusters.

The PE spectra and the equilibrium geometries of Cu_3H^- and Cu_4^- are shown in Figure 4-1 (middle and right column) and Figure 4-4, respectively.

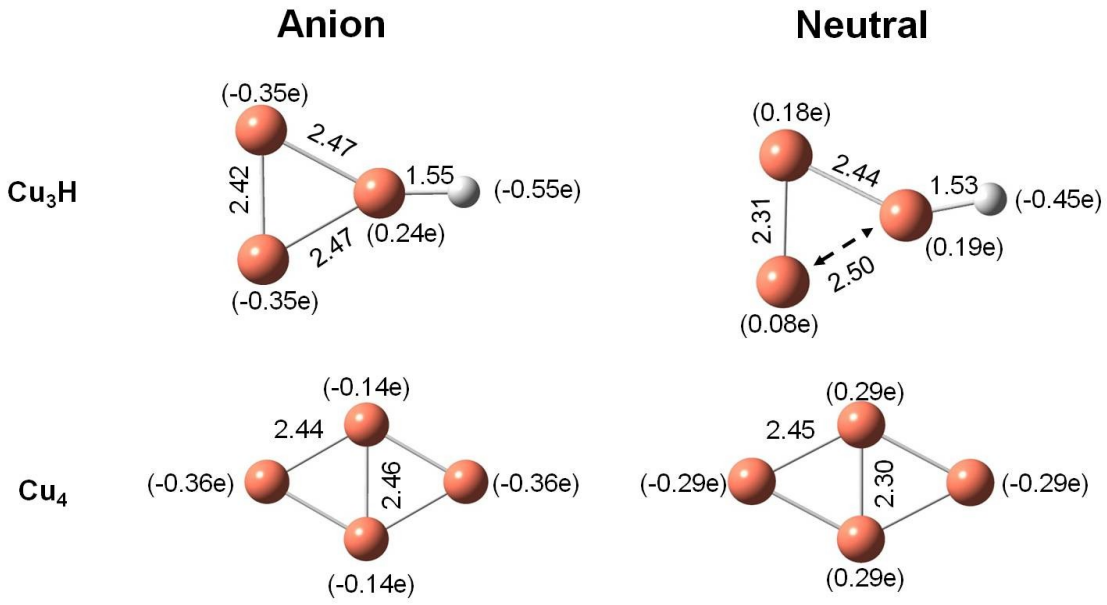

Figure 4-4: Optimized anionic and neutral geometries of Cu_3H and Cu_4. Bond lengths (in Å) and NBO charges (in brackets) are given.

The PE spectra of these two clusters are rather similar with VDEs of Cu_4^- and Cu_3H^- occurring at 1.45 eV and 1.55 eV, respectively. Our calculated values given in Table 4-1 agree well with these values. However, the geometries of both neutral and anionic clusters of Cu_4 are different from those of Cu_3H (see Figure 4-4). In Cu_3H, H-atom is terminally bonded while the corresponding Cu atom in Cu_4 is two-fold coordinated. The structures remain relatively unchanged as an electron is attached. Similar is the case with charge distribution, although the charge on the H atom is more negative than that on Cu atoms. In neutral and anionic Cu_3H clusters the charges on H atom are, respectively, −0.45e and −0.55e. The charges on the corresponding Cu atom in neutral and anionic Cu_4 clusters are −0.29e and −0.36e, respectively.

The PE spectra and the equilibrium geometries of Cu_4H and Cu_5 are shown in Figure 4-1 (right column) and Figure 4-5, respectively. In Cu_5^-, peak A in the PES occurs at 1.92 eV, while in Cu_4H^-, it is shifted to 2.50 eV. In addition to this peak, a small but broad peak is observed at 1.51 eV in Cu_4H^-, which does not exist in the PES of Cu_5^-. As we will show in the following, this is due to the existence of a higher energy isomer in Cu_4H. As seen in Figure 4-5, the ground state geometries of neutral Cu_4H and anionic Cu_4H^- are different, while they are very similar in the case of Cu_5. In neutral Cu_4H, the H atom is bridge bonded to two Cu atoms, and significant bonding exists between various Cu atoms. In anionic Cu_4H^-, the added electron is distributed among Cu atoms, thus breaking Cu–Cu bonds. An isomer of Cu_4H^-, lying 0.3 eV above the ground state, has geometry very much like its ground state neutral. This isomer is responsible for the 1.51 eV peak in Figure 4-1. Our calculated value of 1.73 eV agrees well with this experimental peak. The calculated VDE of 2.86 eV agrees well with the dominant experimental peak A occurring at 2.50 eV. The charges on the H atom in both neutral Cu_4H and anionic Cu_4H^-

are similar, namely about −0.5e, and are more negative than on the Cu atoms in Cu_5, which vary between +0.10e to −0.32e.

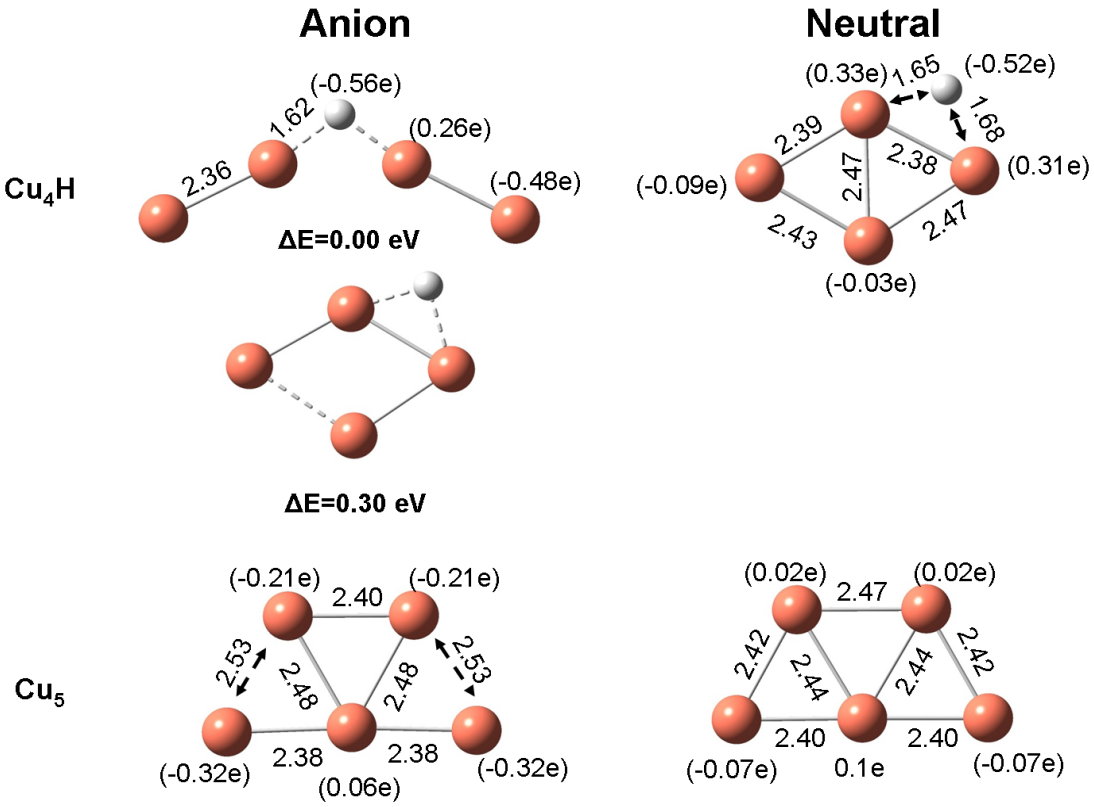

Figure 4-5: Optimized anionic and neutral geometries of Cu_4H and Cu_5. Bond lengths (in Å) and NBO charges (in brackets) are given.

In order to understand the nature of chemical bonding in Cu_n^- and $Cu_{n-1}H^-$ (for $n \geq 3$) systems, the spatial orientation of the highest occupied molecular orbitals (HOMO) are given in Figure 4-6. We recall that $Cu_2H^-$and Cu_4H^- have two isomers (see Figure 4-3 and 4-5), which correspond to two different peaks in the PES in Figure 4-1. The HOMOs of $Cu_{n-1}H^-$ are similar to those of Cu_n^- for n = 3, 4, and 5. This further shows that the electronic structure of Cu_n^- is not affected by replacing one Cu atom by H.

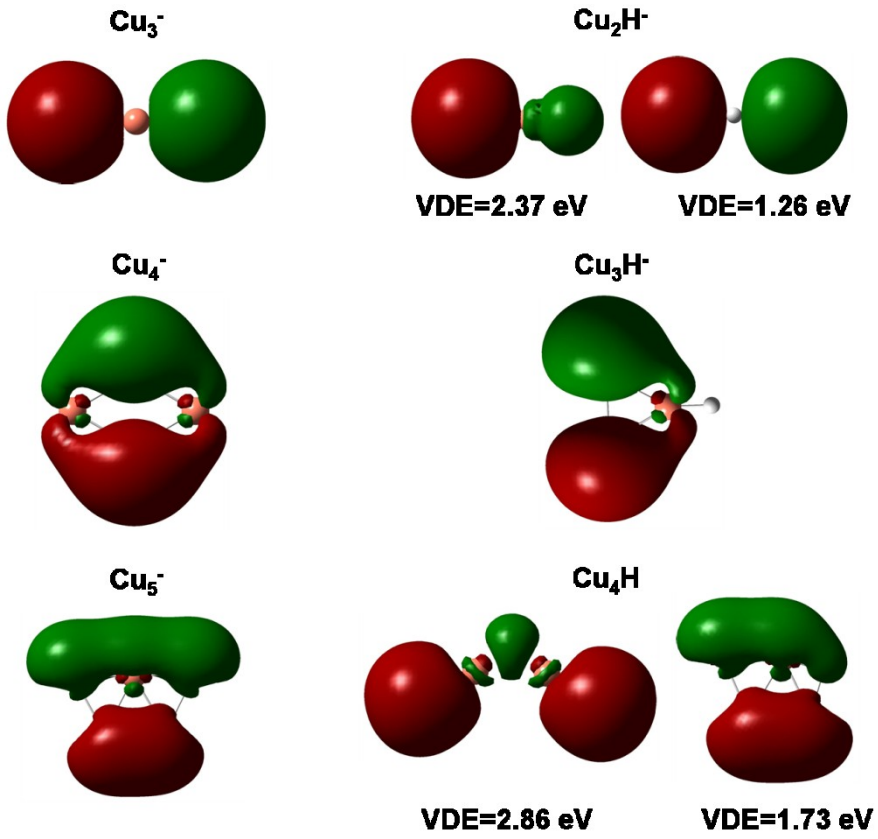

Figure 4-6: Plots of the highest occupied molecular orbitals (HOMOs) of Cu_n^- and $Cu_{n-1}H^-$ for $n \geq 3$ (isovalue 0.02 Å $^{-3}$).

In summary, we see that the electronic structures seen through PES of $Cu_{n-1}H^-$ clusters, as well as through HOMOs, are similar to those of Cu_n^- for n = 3–5. In neutral clusters the H atom remains negatively charged. However, in the anionic clusters the extra added electron preferentially goes to the metal atoms rather than to H. We note that the charge on a given atom is not a uniquely determined quantity as it depends upon the method used to compute the charge. For example, the charges calculated using the Mulliken population analysis are not always the same as those computed from the NBO analysis. Thus, charge on ions should only be used as a qualitative measure of the electronic structure and nature of bonding. Whether the electronic structure of Cu_n^- is similar to that of $Cu_{n-1}H^-$ can be unambiguously determined by comparing

the PES data. In this sense, we can conclude that H mimics the chemistry of the Cu atom in anionic $Cu_{n-1}H^-$ clusters for $n \geq 3$.

4.1.2.2 Ag_n and $Ag_{n-1}H$ clusters

The PE spectra of Ag^-, $Ag_{n-1}H^-$, and Ag_n^- (n = 2–5) are plotted in Figure 4-7. We begin with the PE spectra of Ag^-, AgH^-, and Ag_2^- in Figure 4-7 (left column). The VDEs of Ag^- and Ag_2^- are 1.3 eV and 1.09 eV, respectively. As an Ag atom is replaced by H, the VDE shifts to 0.59 eV.

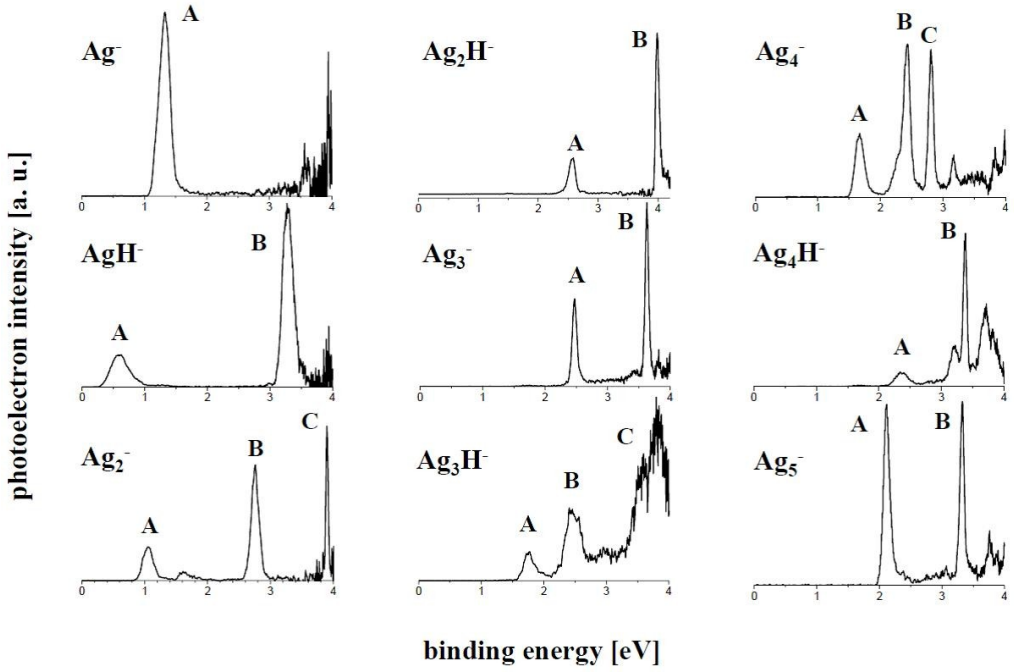

Figure 4-7: Photoelectron spectra of Ag^-, Ag_n^-, and $Ag_{n-1}H^-$ (n = 2–5).

From the equilibrium geometries and charge distribution of neutral and anionic AgH and Ag_2 clusters as shown in Figure 4-8, we see that while the charge on the H atom in anionic AgH is similar to that of an Ag atom in Ag_2, they are different for the neutral cluster. These results are similar to those seen in CuH and Cu_2 clusters. The computed VDEs of AgH^- and Ag_2^-, given in Table 4-2, agree well with experiment.

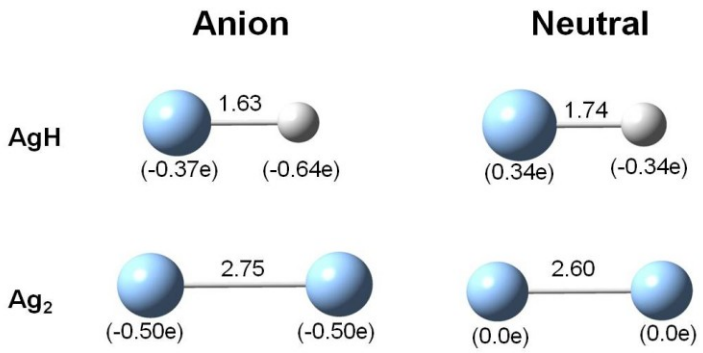

Figure 4-8: Optimized anionic and neutral geometries of AgH and Ag_2. Bond lengths (in Å) and NBO charges (in brackets) are given.

Table 4-2: Experimental and theoretical results of Vertical Detachment Energies (VDEs) and theoretical Electron Affinities (EAs) in eV of Ag_n and $Ag_{n-1}H$.

Cluster	**Expt. VDE of Ag_n^-, $Ag_{n-1}H^-$ (eV)**	**Theo.VDE of Ag_n^-, $Ag_{n-1}H^-$ (eV)**	**Theo. EA of Ag_n, $Ag_{n-1}H$ (eV)**
Ag	1.3	1.38	1.38
Ag_2	1.09	1.19	1.12
AgH	0.59	0.72	0.67
Ag_3	2.47	2.39	2.38
Ag_2H	2.45	2.60	2.39
Ag_4	1.66	2.31[a] 1.80[b]	1.83[a] 1.71[b]
Ag_3H	1.75	1.85	1.79
Ag_5	2.22	2.17	2.10
Ag_4H	2.36	3.07[a] 2.67[b]	2.53[a] 2.19[b]

[a] The structure corresponding to the ground state of neutral and anion geometries.
[b] The structure corresponding to the neutral species and the anion having nearly similar geometries.

The experimental photoelectron spectra of Ag_2H^- and Ag_3^- are shown in Figure 4-7 (middle column). The corresponding calculated equilibrium geometries with bond lengths and charge distributions are given in Figure 4-9.

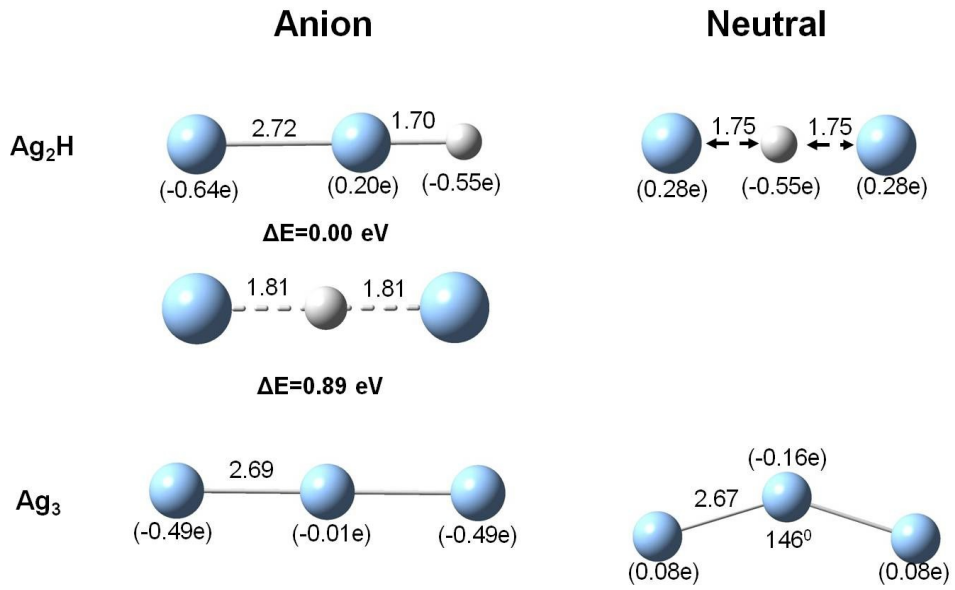

Figure 4-9: Optimized anionic and neutral geometries of Ag_2H and Ag_3. Bond lengths (in Å) and NBO charges (in brackets) are given.

The PES data of Ag_3^- agree well with those of Ag_2H^-. This is similar to that seen in the case of Cu_3 and Cu_2H where the prominent peaks A are nearly similar for both Cu_3 and Cu_2H clusters. Peak A of Ag_3^-, corresponding to a VDE of 2.47 eV, coincides with peak A of Ag_2H^- occurring at 2.45 eV. The geometries and charge distributions in Figure 4-9 are also similar between Ag_3^- and Ag_2H^-. The anionic clusters of Ag_3 and Ag_2H have linear geometry, where the charges on the terminal Ag atom in Ag_3^- and H-atom in Ag_2H^- are nearly the same. The geometry of neutral Ag_2H is linear with the H atom inserted between the Ag atoms. The geometry of neutral Ag_3, on the other hand, is close to being linear with an apex angle of 146º. The charges on the H atom in neutral Ag_2H and the corresponding Ag atom in neutral Ag_3 are different, the former being

significantly more negative than the latter. The isomer of Ag_2H^- where the H atom is inserted between the Ag atoms is 0.89 eV above the ground state geometry where H is terminally bonded. The PES of Ag_3H^- is compared with that of Ag_4^- in Figure 4-7 (middle and right column). We note that once again the peaks marked A coincide, implying that the electronic structure of Ag_4^- does not change much as one Ag atom is replaced by H. The equilibrium geometries of these clusters are shown in Figure 4-10 and the VDEs and EAs are given in Table 4-2.

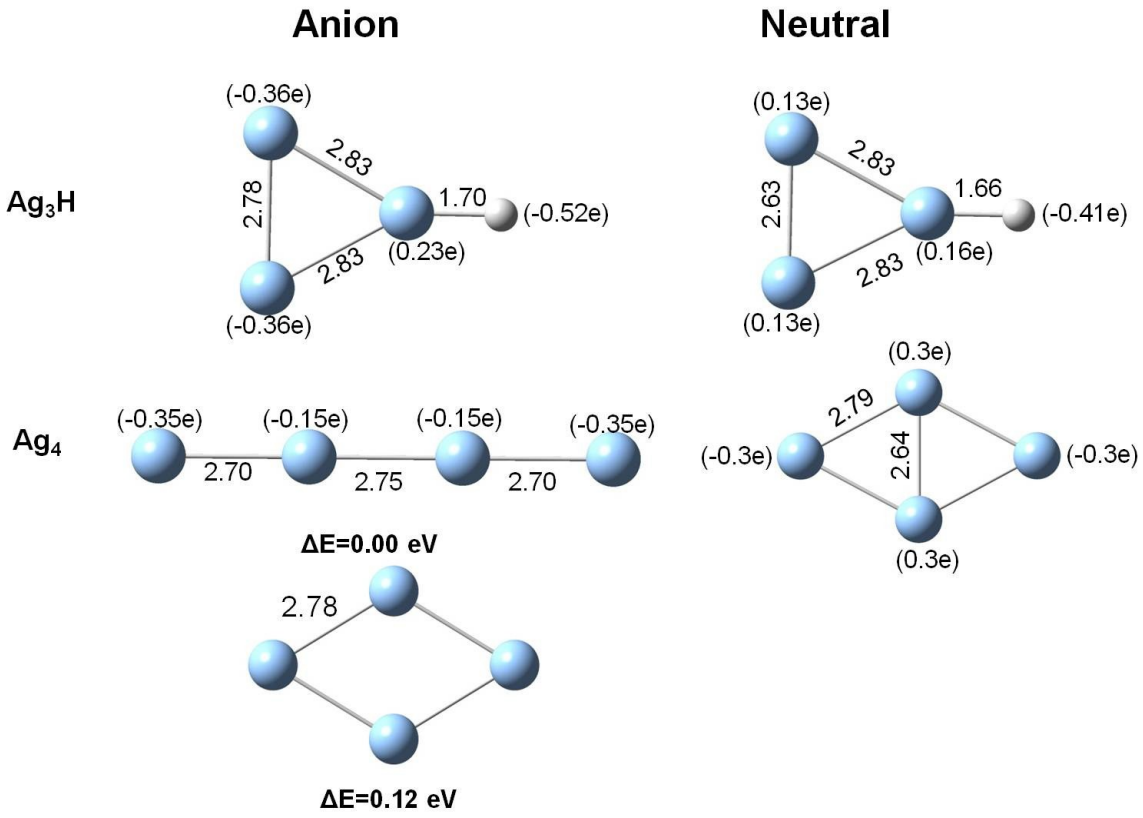

Figure 4-10: Optimized anionic and neutral geometries of Ag_3H and Ag_4. Bond lengths (in Å) and NBO charges (in brackets) are given.

The equilibrium geometries of neutral and anionic Ag_3H clusters are similar but they are different for Ag_4. While the ground state of neutral Ag_4 is planar, its anion is a linear chain.

The planar Ag_4^- isomer is 0.12 eV higher in energy than its ground state. The VDE corresponding to this higher energy isomer of Ag_4^- agrees well with the experiment. In both neutral and anionic Ag_3H and Ag_4 clusters, the charge on the H atom and the corresponding Ag atom it replaces are rather similar.

The PES of Ag_5^- and Ag_4H^- are compared in Figure 4-7 (right column). We note that the VDE of Ag_4H^- is 2.36 eV which agrees well with that of Ag_5^-, namely 2.22 eV. The peaks corresponding to higher binding energies are also in agreement. The equilibrium geometries and charge distributions are shown in Figure 4-11.

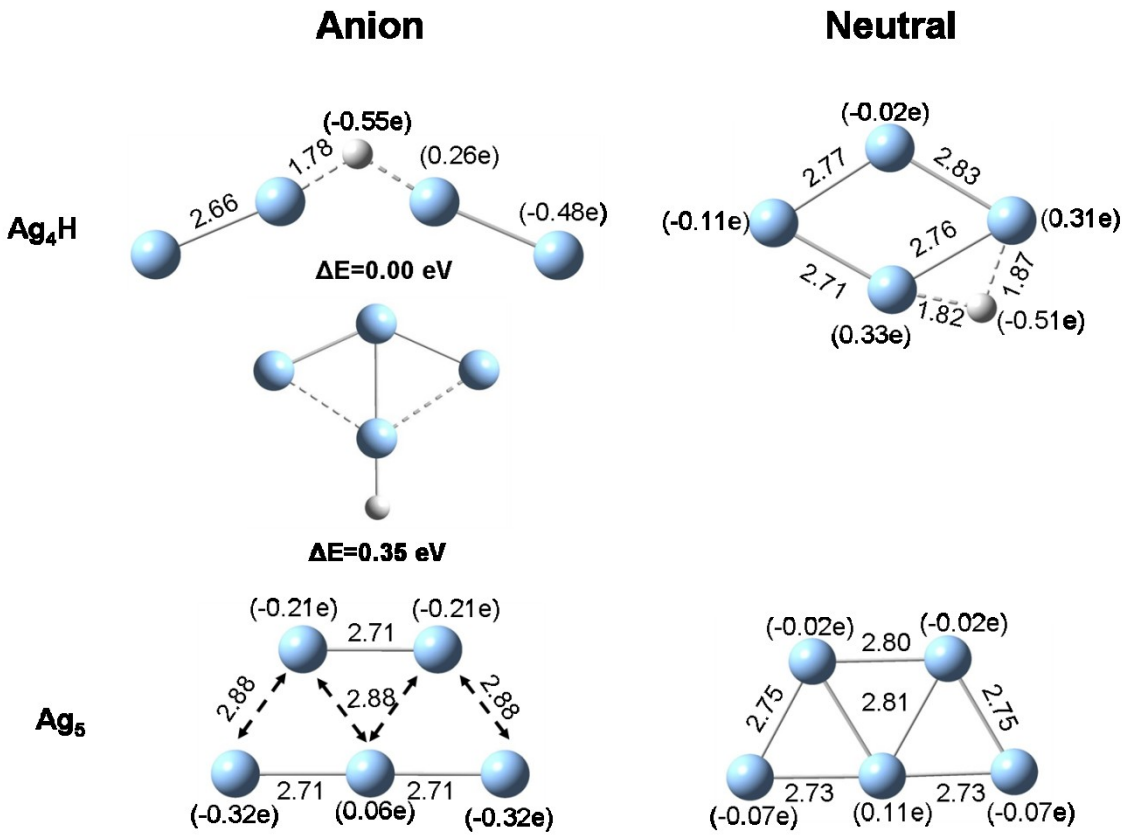

Figure 4-11: Optimized anionic and neutral geometries of Ag_4H and Ag_5. Bond lengths (in Å) and NBO charges (in brackets) are given.

The geometries of neutral and anionic Ag_5 and Ag_4H clusters are similar to those of neutral Cu_5 and Cu_4H. An isomer of Ag_4H^- lying 0.35 eV above the ground state has a radially bonded H and its structure is similar to that of neutral Ag_4H in the sense that the four Ag atoms maintain a rhombus structure. The computed VDE and EA of these clusters are compared with experiment in Table 4-2. The theoretically calculated VDE for Ag_5^- agrees very well with the experiment. The VDE corresponding to the ground state of the Ag_4H anion is 3.07 eV and that of the higher energy state is 2.67 eV. Note that it is the VDE associated with this higher energy isomer that agrees better with the experimental value of 2.36 eV. Peak B at 3.3 eV, on the other hand, corresponds to the ground state of the anion.

In order to understand the nature of chemical bonding in Ag_n^- and $Ag_{n-1}H^-$ (for $n \geq 3$) clusters, the spatial orientation of the highest occupied molecular orbitals (HOMO) are given in Figure 4-12. The HOMOs of Ag_3^- and Ag_2H^- are similar. Theoretically we found two isomers for Ag_4^- and Ag_4H^-. The HOMOs of the higher energy isomer of Ag_4^- and Ag_4H^- which correspond to a VDE of 1.80 eV and 2.67 eV, respectively, are similar to the HOMOs of Ag_3H^- and Ag_5^-. This further shows that the electronic structure of Ag_n^- is not affected by replacing one Ag atom by H.

In summary, the electronic structures of $Ag_{n-1}H^-$ clusters seen from PES are similar to those of Ag_n^- for n = 3–5 leading us to conclude that H mimics the chemistry of the Ag atom in these clusters as is the case with Cu_nH systems.

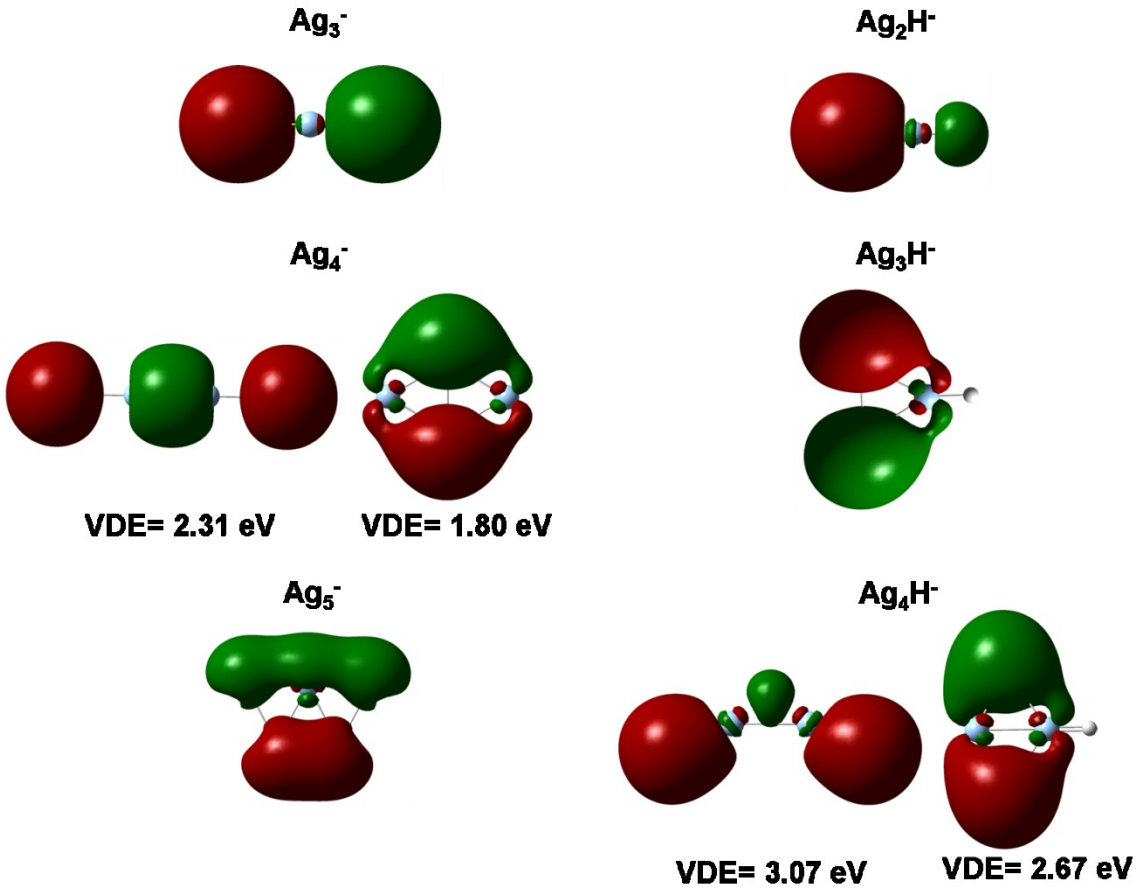

Figure 4-12: Plots of the highest occupied molecular orbitals (HOMOs) of Ag_n^- and $Ag_{n-1}H^-$ for $n \geq 3$ (isovalue 0.02 $Å^{-3}$).

4.1.3 Conclusion

A synergistic study involving PES experiments and DFT calculations of the electronic structure and equilibrium geometries of neutral and anionic Cu_n, $Cu_{n-1}H$, Ag_n, and $Ag_{n-1}H$ (n = 2–5) clusters show that,

(1) H mimics the properties of coinage metal atoms in anionic clusters for $n \geq 3$. This is evidenced by the similarity between the photoelectron spectra and highest molecular orbitals of $M_{n-1}H^-$ and M_n^- (M = Cu, Ag; $n \geq 3$) clusters as well as by the agreement between the calculated and measured vertical detachment energies.

(2) The charge on the H atom is negative irrespective of whether the cluster is neutral or anionic. This is similar to the general behavior of H in metals. The charges on the Cu atoms, on the other hand, vary over a wide margin, but in anionic clusters, the added electron is shared between the Cu atoms, thus bringing the charge on the H atom close to that of the corresponding Cu atom.

(3) In $Ag_{n-1}H$ clusters the charge on the H atom is similar to that on the Ag atom it replaces in Ag_n clusters.

(4) The existence of higher energy isomers in the $Cu_{n-1}H^-$ clusters accounts for the weak peaks in the photoelectron spectra. It will be interesting to see if the reactivity of the clusters is affected by H substitution. This will form the basis of our future studies.

References:

[1] (a) Bell, R. C. & Castleman, A. W. Reactions of vanadium oxide cluster ions with 1,3-butadiene and isomers of butene. *J. Phys. Chem. A* **106,** 9893–9899 (2002).
(b) Bell, R. C., Zemski, K. A., Justes, D. R. & Castleman, A. W. Formation, structure and bond dissociation thresholds of gas-phase vanadium oxide cluster ions. *J. Chem. Phys.* **114,** 798–811 (2001).

[2] Reilly, N. M. *et al.* Experimental and theoretical study of the structure and reactivity of Fe_mO_n+ (m=1, 2; n=1-5) with CO. *J. Phys. Chem. C* **111,** 19086–19097 (2007).

[3] Zemski, K. A., Justes, D. R. & Castleman, A. W. Studies of metal oxide clusters: Elucidating reactive sites responsible for the activity of transition metal oxide catalysts. *J. Phys. Chem. B* **106,** 6136–6148 (2002).

[4] Landman, U., Luedtke, W., Burnham, N. & Colton, R. Atomistic Mechanisms and Dynamics of Adhesion, Nanoindentation, and Fracture. *Science* **248,** 454–461 (1990).

[5] Hakkinen, H., Barnett, R. N., Scherbakov, A. G. & Landman, U. Nanowire gold chains: Formation mechanisms and conductance. *J. Phys. Chem. B* **104,** 9063–9066 (2000).

[6] Cleveland, C. L. *et al.* Structural evolution of smaller gold nanocrystals: The truncated decahedral motif. *Phys. Rev. Lett.* **79,** 1873–1876 (1997).

[7] Hakkinen, H., Barnett, R. N. & Landman, U. Electronic structure of passivated $Au_{38}(SCH_3)_{24}$ nanocrystal. *Phys. Rev. Lett.* **82,** 3264–3267 (1999).

[8] Jena, P. Materials for Hydrogen Storage: Past, Present, and Future. *J. Phys. Chem. Lett.* **2,** 206–211 (2011).

[9] Schlapbach, L. & Zuttel, A. Hydrogen-storage materials for mobile applications. *Nature* **414,** 353–358 (2001).

[10] Chen, X., Li, C., Graetzel, M., Kostecki, R. & Mao, S. S. Nanomaterials for renewable energy production and storage. *Chem. Soc. Rev.* **41,** 7909–7937 (2012).

[11] Sorte, E. G. *et al.* Mobile Species in $NaAlH_4$. *J. Phys. Chem. C* **117,** 8105–8113 (2013).

[12] Teprovich, J. A., Motyka, T. & Zidan, R. Hydrogen system using novel additives to catalyze hydrogen release from the hydrolysis of alane and activated aluminum. *Int. J. Hydrog. Energy* **37,** 1594–1603 (2012).

[13] Govender, M. G. & Ford, T. A. Hydrogen bonds, improper hydrogen bonds and dihydrogen bonds. *Theochem-J. Mol. Struct.* **630,** 11–16 (2003).

[14] Ivanovic, N., Novakovic, N., Colognesi, D., Radisavljevic, I. & Ostojic, S. Electronic Principles of Some Trends in Properties of Metallic Hydrides. *Int. J. Mod. Phys. B* **24,** 703–710 (2010).

[15] Latroche, M. & Percheron-Guegan, A. Hydrogen storage properties of metallic hydrides. *Ann. Chim.-Sci. Mat.* **30,** 471–482 (2005).

[16] Akiba, E. & Okada, M. Metallic hydrides III: Body-centered-cubic solid-solution alloys. *MRS Bull.* **27,** 699–703 (2002).

[17] P Jena, P., Fradin, F. & Ellis, D. Models of Electronic-Structure of Hydrogen in Metals: Pd-H. *Phys. Rev. B* **20,** 3543–3551 (1979).

[18] Hydrogen in Metals: Topics in Applied Physics, ed. G. Alefeld and J. Volk, Springer, Berlin, 1978, vol. 28.

[19] Buckart, S., Gantefor, G., Kim, Y. D. & Jena, P. Anomalous behavior of atomic hydrogen interacting with gold clusters. *J. Am. Chem. Soc.* **125,** 14205–14209 (2003).

[20] Zhai, H. J., Kiran, B. & Wang, L. S. Observation of Au_2H^- impurity in pure gold clusters and implications for the anomalous Au-Au distances in gold nanowires. *J. Chem. Phys.* **121,** 8231–8236 (2004).

[21] Zubarev, D. Y., Li, J., Wang, L. S. & Boldyrev, A. I. Theoretical probing of deltahedral closo-AuroBoranes $B_xAu_x^{2-}$(x=5-12). *Inorg. Chem.* **45,** 5269–5271 (2006).

[22] Chen, E. & Wentworth, W. Experimental Values of Atomic Electron Affinities - Their Selection and Periodic Behavior. *J. Chem. Educ.* **52,** 486–489 (1975).

[23] Jena, N. K., Chandrakumar, K. R. S. & Ghosh, S. K. Beyond the Gold-Hydrogen Analogy: Doping Gold Cluster with H-atom-O_2 Activation and Reduction of the Reaction Barrier for CO Oxidation. *J. Phys. Chem. Lett.* **2,** 1476–1480 (2011).

[24] Haruta, M., Kobayashi, T., Sano, H. & Yamada, N. Novel Gold Catalysts for the Oxidation of Carbon-Monoxide at a Temperature Far Below 0ºC. *Chem. Lett.* 405–408 (1987). doi:10.1246/cl.1987.405

[25] Lee, S., Fan, C. Y., Wu, T. P. & Anderson, S. L. Cluster size effects on CO oxidation activity, adsorbate affinity, and temporal behavior of model Au_n/TiO_2 catalysts. *J. Chem. Phys.* **123,** 124710 (2005).

Chapter 5

GAS STORAGE AND SEQUESTRATION – A CLUSTER APPROACH

Although majority of world's energy consumption at present comes from fossil fuels (ca. 87%), it has a negative impact on the environment. A significant amount of gases such as CO_2 and SO_2 are released from fossil fuel combustion at power plants and other industrial facilities. The former is responsible for global warming and climate change[1], and the later, leads to acid rain and is responsible for deforestation as well as threatening people and living animals[2]. Carbon dioxide (CO_2) capture and sequestration (CCS) plays an important role in reducing greenhouse gas emissions into the environment. On the other hand, existing methods, such as limestone scrubbing[3], ammonia scrubbing, and organic solvents absorption, are useful for selective SO_2 capture. Development of viable technologies for CCS and the selective removal of SO_2 from flue gas or methane (CH_4) reach gases are highly desirable. Moreover, as the world's population continues to grow and the limited amount of fossil fuels begins to diminish, one has to look for alternative sources of energy, which should be clean and environmentally friendly. Hydrogen and methane have emerged as some possible sources[4]. However, they often get contaminated by CO_2, which poses a significant obstacle, since its presence can hinder the

efficiency of using these gases as an energy source[5]. Therefore, storage of such gases and separating them from CO_2 has also become a growing interest in the scientific community.

Among the emerging methods for addressing such challenges is the use of highly porous architectures with a predefined pore structure and functionality as in the case of porous organic polymers (POPs)[6], zeolitic imidazolate frameworks (ZIFs)[7], covalent-organic framework (COFs)[8] and metal–organic frameworks (MOFs)[9]. Porous polymers, in general, facilitate gas separation by their preferential adsorptive properties that can be accessed through pore functionalization. The linkage by strong covalent bonds and usual composition of light elements (H, C, N, B, O) in these polymers lead to many tantalizing properties such as low density, high porosity, and physical stability as in the case of microcrystalline COFs [8]. In addition to that, incorporation of polarizable building blocks into the backbone of such materials has shown to enhance gas uptake[10]. For example, fluorinated polymers, with their highly polar C–F bonds, remain among the best performing organic membranes in CO_2 separation as a result of their high hydrophobicity, high fractional free volume, and the dipole–quadrupole interaction between C–F and CO_2[11].

Along these lines, two new class of porous polymers, termed as borazine-linked polymers (BLPs) and benzimidazole-linked polymers (BILPs), have been synthesized by Dr. El Kaderi's group at Virginia Commonwealth University, and the storage and separation of gases such as CO_2, H_2, and CH_4 for the BLPs and SO_2 for the BILPs have been investigated. To understand the reason behind the efficient storage capacity of these polymers and the mechanism with which the gas molecules interact, it is important to gain insight into the electronic nature of the polymeric system. This can be achieved by theoretical study, which has been performed in our lab. These polymers typically include thousands of atoms, which make the application of

standard theoretical methods computationally expensive and even unfeasible. To ease the computational cost, the polymeric systems were simplified to a monomeric unit, which is the building block of these polymers and the dangling bonds of the atoms were saturated with hydrogen. This study will help to understand the interaction mechanism between the polymer and gas molecules, to find the preferential binding sites where the gas molecules interact and to calculate the binding energies of the gases to the polymers that can be compared with the experimental results.

This work is a joint collaboration between experimental and theoretical groups to investigate the gas storage and separation performance of porous polymers, namely BLPs and BILPs. Based upon the type of polymers, this study is divided into two different sections. In the first section, we will discuss the gas uptake capacity of BLPs functionalized with Cl, and in the second, we discuss the gas uptake by two functionalized BILPs, which are designed by integrating imidazole rings into the backbone of the polymers.

5.1 Gas uptake by borazine-linked polymer (BLPs)

5.1.1 Introduction

Borazine ($B_3H_6N_3$) is isostructural and isoelectronic to the boroxine ($B_3O_3H_3$) units found in COFs. The inclusion of borazine ($B_3H_6N_3$) as a functionalized polar building block into porous organic polymers (POPs) has been mainly used for the fabrication of BN-based ceramics or organic optoelectronic materials. However to date, the use of borazine for the preparation of porous polymers for gas storage has not yet been developed. A new BLP, which is functionalized using Cl namely BLP-10(Cl) (also called as chlorinated borazine (CB)), has been synthesized in Dr. El Kaderi's lab, and its performance in small gas storage and separation, such as CO_2, H_2 and CH_4, has been investigated for the first time. It was found that the adsorptive

properties of BLPs were altered by the polarizable nature of the borazine units and the associated substitution on boron seems to be decisive in attaining a very high CO_2/CH_4 selectivity.

A brief description of the theoretical methods is provided in section 5.1.2. Results and discussion are given in section 5.1.3, followed by conclusion in section 5.1.4.

5.1.2 Theoretical methods

Theoretical calculations were performed on the building block of the polymeric unit. The binding energies (E_b) of H_2, CO_2 and CH_4 molecules attached to chlorinated borazine (CB) were calculated by determining the equilibrium geometries and corresponding total energies of these complexes and comparing them with experimental results.

We define E_b as,

$$E_b = -\{E[(CB).x] - E[CB] - E[x]\}$$

where x denotes H_2, CO_2 or CH_4 molecule; E[(CB).x] is the total energy of the chlorinated borazine interacting with H_2, CO_2 or CH_4; and E[CB] and E[x] are, respectively, the total energies of the CB and the x molecule.

To obtain the equilibrium geometries, density functional theory (DFT) calculations were performed with different forms for the exchange-correlation potential. These include the Becke's three parameter hybrid functional for exchange and the Lee-Yang-Parr functional for correlation (B3LYP)[12], the local density approximation (LDA) for exchange-correlation potential prescribed by Vosko-Wilk-Nusair (SVWN)[13] and the Minnesota functional (M06)[14] prescribed by Zhao and Truhlar that includes corrections due to long range dispersive forces. We note that since the interaction of H_2, CO_2 or CH_4 with the CB substrate is expected to be weak, it is necessary to go beyond the generalized gradient functionals that do not include van der Waal's terms and hence underestimate binding energies. While the LDA also does not include long range dispersive

forces, it is known to over-bind. Thus, it is possible that, due to cancellation of errors where it over estimates the exchange energy (E_x) and underestimates the correlation energy (E_c), the LDA may yield binding affinities that are closer to experiment than the GGA functionals. This is found indeed to be the case. We have used the *Gaussian 09* package[15] and 6-311+G*[16,17] basis sets in all our computations.

Several initial geometries were taken where the molecules were allowed to approach different sites of CB including the top of the borazine ring, the bridge sites as well as on top of B and N atoms. The molecules were further allowed to align perpendicular or parallel to the ring surface. The geometries were first optimized without symmetry constraint at the B3LYP level of theory. These geometries were then used as starting configurations with other functionals such as M06 and SVWN and re-optimized. All optimizations are followed by frequency calculations to confirm that the structures belong to genuine minima in the potential energy surface. The atomic charges have been evaluated by applying the Natural Bonding Orbital method (NBO)[18].

5.1.3 Results and Discussions

Figure 5-1 illustrates the optimized geometries obtained from the M06/6-311+G* level of theory. The geometries obtained at the B3LYP and SVWN level of theory are given in the Appendix III. In the case of an H_2 molecule interacting with a chlorinated borazine (CB), the H_2 is bound molecularly with a bond length of 0.75 Å and at a distance of 2.76 Å from the boron site. CO_2 and CH_4, on the other hand, interact with the central ring system of borazine at a distance of 3.12 Å and 3.33 Å respectively. The bond length between the carbon and oxygen atoms of CO_2 is 1.16 Å while the distance between the carbon and hydrogen of CH_4 is 1.10 Å. The binding energies of all gases with the CB rings obtained from M06 calculations (summarized in Table 5-1), agrees well with the experiment.

Table 5-1: Comparison of calculated binding energy of CO_2, H_2 and CH_4 to CB with experimental values[a].

Clusters	Expt (kJ/mol)	M06/6-311+G* (kJ/mol)	SVWN/6-311+G* (kJ/mol)	B3LYP/6-311+G* (kJ/mol)
CB – H_2	7.46	9.05	10.39	-2.33
CB – CO_2	28.28	15.46	25.95	-*
CB – CH_4	20.20	20.22	20.30	-0.22

[a]CB represents the chlorinated-borazine ring.
*Since the B3LYP results for H_2 and CH_4 were unphysical, we did not repeat the calculations for CO_2.

The binding energies calculated at the SVWN level of theory agree best with the experimental results, even though this functional does not take into account van der Waals' interactions. In contrast, the results obtained using B3LYP do not show any binding, which demonstrates the importance of taking into account dispersive forces while dealing with weakly bound systems. The theoretical investigations indicate that all of the gas molecules preferentially interact with the borazine ring rather than the phenyl substituent of the nitrogen atoms, which highlights the significance of including polarizable building blocks in adsorbent materials. The experimental results are obtained by calculating isosteric heat of adsorption (Q_{st}) for each gas using the virial method[19]. Q_{st} for hydrogen at zero-coverage is found to be 7.5 kJ/mol, which ranks well among the values reported for organic polymers, such as COFs[20] (6.0–7.0 kJ/mol), and is only slightly lower than that for BILPs[21] (7.9 kJ/mol). The zero coverage Q_{st} values for CO_2 and CH_4 were calculated from isotherms collected at 273 and 298 K and found to be 28.3 and 20.2 kJ/mol, respectively, which are surprisingly high for purely organic materials[22]. The expected reason behind higher affinity for CO_2 over CH_4 may result from the non-polar nature of CH_4, whereas

CO_2 possesses a quadrupole moment that contributes positively towards the CO_2/CH_4 selectivity by BLP-10(Cl).

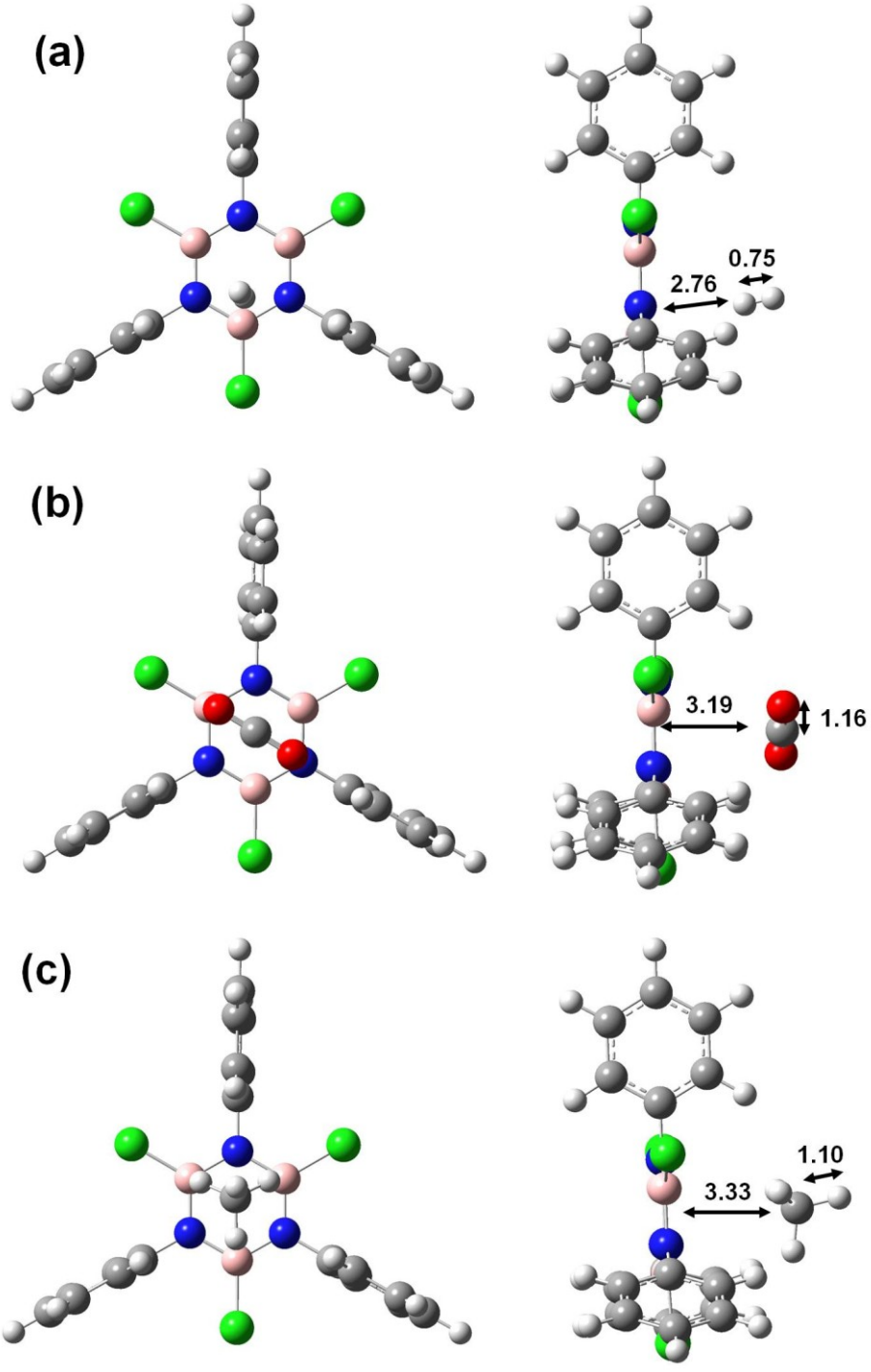

Figure 5-1: Optimized geometries of (a) H_2, (b) CO_2, and (c) CH_4 adsorbed onto chlorinated borazine calculated from the M06/6-311+G* level of theory. Bond lengths are in Å. Front and side views are given on the left and right panel respectively.

5.1.4 Conclusions

A synergistic study involving the one pot synthesis technique and density functional theory calculations of a new class of organic porous polymers namely borazine-linked-polymers (BLPs), was carried out to understand storage and separation of small gas (H_2, CO_2 and CH_4) molecules. The polymer BLP-Cl(10) is found to provide a very high CO_2/CH_4 selectivity. The computational study indicates that the gas molecules interact favorably with the borazine unit, which highlights the significance of including polarizable building blocks in the adsorbent materials.

5.2 Gas uptake by benzimidazole-linked polymers (BILPs)

5.2.1 Introduction

Due to its acidic and reactive nature, SO_2 capture by porous materials has not been widely investigated. However, recent studies involving purely organic structures or MOFs showed great potential. Motivated by this study, in this section we demonstrated the SO_2 uptake by two new representative polymers of benzimidazole-linked polymers (BILPs), namely BILP-3 and BILP-4. By virtue of its high physicochemical stability and exceptionally high uptake capacity, these polymers are found to be well-suited for selective SO_2 capture and are among the highest for all known materials reported to date including organic and inorganic-organic hybrid structures. Moreover, the electronic nature of BILPs plays a central role in attaining such high SO_2 uptake, which is evidenced from gas uptake studies and DFT calculations. The imidazole-functionalized pore walls and the subnano pore dimensions of these polymers are found to facilitate selective SO_2 uptake.

A brief description of the theoretical calculations is given in section 5.2.2, the results are discussed in section 5.2.3, followed by conclusion in section 5.2.4.

5.2.2 Theoretical methods

For simplification, theoretical calculations were performed using DFT for BILP-4 and BILP-3 segments containing two and three imidazole rings, respectively, similar to the one mentioned in section 5.1.2. Since the B3LYP level of theory showed unphysical results, here we only perform the calculations using LDA and the M06 level of theory.

We define the binding energy (E_b) for BILP interacting with SO_2 as,

$$E_b = -\{E[\text{BILP-4}@n\text{SO}_2] - E[\text{BILP-4}] - n*E[\text{SO}_2]\}/n; \text{ where } n = 2,4$$

$$E_b = -\{E[\text{BILP-3}@n\text{SO}_2] - E[\text{BILP-3}] - n*E[\text{SO}_2]\}/n; \text{ where } n = 3,6$$

where E[BILP-4@nSO$_2$] and E[BILP-3@nSO$_2$] are the total energies of BILP-4 and BILP-3 interacting with n number of SO_2 molecules. E[BILP-4], E[BILP-3] and E[SO_2] are the total energies of BILP-4 and BILP-3 and the SO_2 molecules, respectively.

From the Natural Bonding Orbital method (NBO)[18], we found that the electronegative regions appear around the double-bonded nitrogen atoms rather than N-H site. The aromatic cores also have significant negative charge. This kind of charge localization makes the benzimidazole derived porous surface more favorable to site selective adsorption of small gas molecules, particularly polar gas molecules. More details on their interaction are discussed below.

5.2.3 Results and Discussions

Figure 5-2 illustrates the fully optimized geometries of BILP-4@nSO$_2$ obtained from the M06/6-311+G* level of theory. Geometries were also optimized using SVWN/6-311+G* level

of theory (as shown in Appendix III), which yielded similar spatial orientations of SO_2 molecules as they were observed in M06/6-311+G* level of theory, but closer proximity to the adsorption sites. This difference may be due to the overestimation of binding in LDA method.

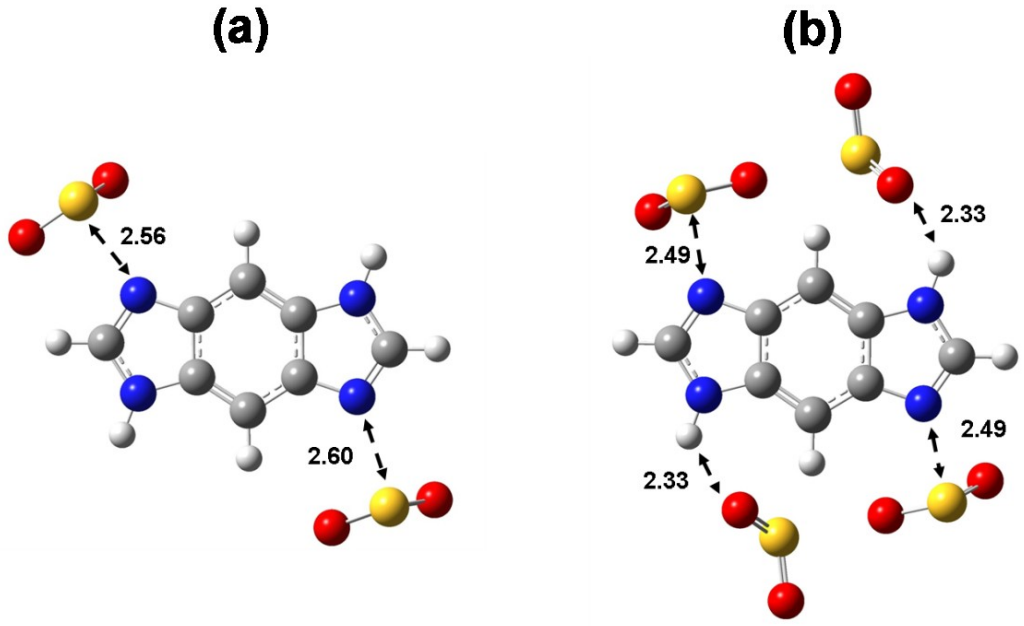

Figure 5-2: Fully optimized geometries of (a) BILP-4@2SO_2 and (b) BILP-4@4SO_2. The bond lengths are in Å.

In case of BILP-4@*n*SO_2, when the two SO_2 molecules were allowed to interact with different binding sites of BILP-4, the minimum energy structure was obtained when the SO_2 molecules (referred to as SO_2 (I)) bind to the N-site of BILP-4 at a bond length of 2.56 and 2.60 Å, respectively, on the double bonded N-sites of imidazole rings (as shown in Figure 5-2(a)). On the other hand, when two more SO_2 molecules (referred to as SO_2(II)) are added, they prefer to bind close to the double bonded N-sites of imidazole rings at a bond length of 2.49 Å while the other two prefer to bind in between the benzene H and NH of imidazole rings at a bond length of 2.33 Å (shown in Figure 5-2(b)). These SO_2 molecules (i.e SO_2(II)) are tilted in such a way that S is directed towards the benzene ring and O atom of the first SO_2, while the O is directed

towards H of NH-site. The bonding preference can be explained by examining the NBO charges. The NBO charge on the S-atom of SO_2 and the N-atom of BILP-4 are +1.62e and -0.56e, respectively, whereas the charges on the O-atom of SO_2 and the H-atom of BILP-4 are -0.86e and +0.44e, respectively. The electrostatic force of interaction between S-atom of SO_2 and N-atom of BILP-4 and between O-atom of SO_2 and H-atom of BILP-4 can be attributed to dipole-dipole interaction and hydrogen bonding, respectively. In addition to these above interactions, adsorbed SO_2(I) appears to affect the spatial orientation of SO_2(II) resulting in slight displacements of SO_2 from the BILP-plane. This is probably due to the intermolecular attraction between O and S atoms of SO_2(I) and SO_2(II), respectively. This observation appears to support the expected spatial arrangements of SO_2 in real polymeric system in which polymer extends its growth along the plane of each benzimidazole moieties. It should also be noted that benzene ring possesses significant negative charge which may attract positively charged S of SO_2 and leads the second pair of SO_2 molecules to take orientation mentioned in the above.

In Figure 5-3, the partially optimized geometries of BILP-3@$n$$SO_2$ obtained from the M06/6-311+G* level of theory are given, and those obtained using the SVWN/6-311+G* level of theory are given in Appendix III. It should be noted that, in the case of BILP-3@6SO_2, when full optimization was carried out, the strands started bending at both the LDA and M06 level of theory with bending being more pronounced at the LDA level of theory (shown in Appendix III). This is because of the strong dipole-dipole interaction between the two polar moieties *i.e* SO_2 and imidazole rings. Since BILP-3 framework is very rigid, this bending is unphysical and results from our choosing a free standing segment to represent the polymer matrix. However, in polymeric system this kind of distortion may require very high energy and can be neglected. In addition, it is better to compare the binding energies between SO_2 and adsorption sites for a rigid

benzimidazole ring in BILP-3@nSO$_2$ to that of BILP-4@nSO$_2$. To consider these, we have carried out partial optimization of BILP-3@nSO$_2$ where we froze the BILP-3 framework and only allowed optimization of binding sites of the SO$_2$ molecules (Figure 5-3).

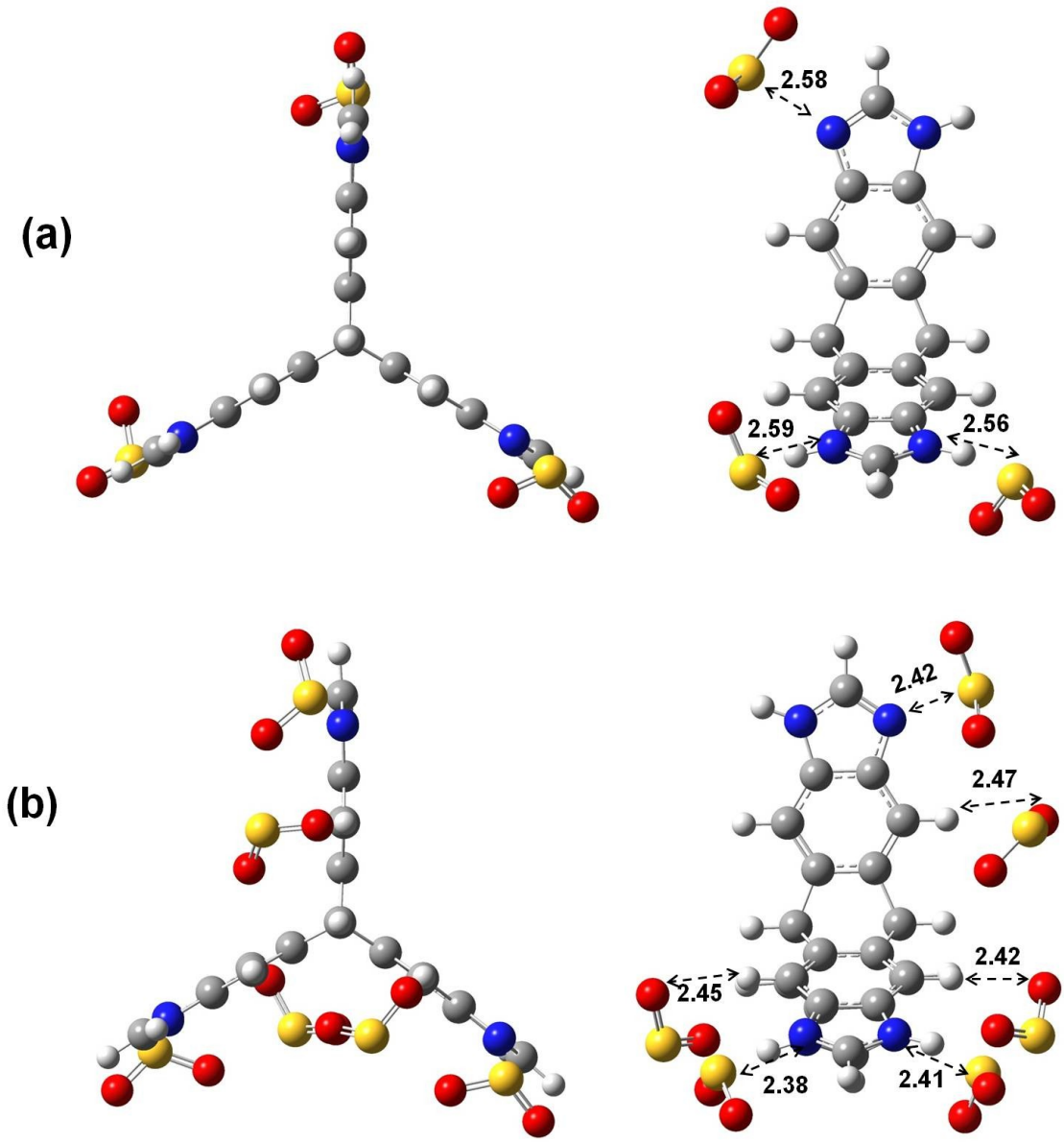

Figure 5-3: Partially optimized geometries of (a) BILP-3@3SO$_2$ and (b) BILP-3@6SO$_2$. The bond lengths are in Å.

Similar to the case of BILP-4, when three molecules of SO_2 (one SO_2 per imidazole ring) are allowed to interact with different sites of BILP-3, the minimum energy structure was obtained when the SO_2 molecules (SO_2(I)) lie in close proximity towards the double bonded N-sites of imodazole rings with a distance that ranges from 2.56 to 2.59 Å (shown in Figure 5-3(a)). On addition of six SO_2 molecules, three of them lie towards the double bonded N-site at a bond distance ranging from 2.38 to 2.42 Å and the other three lie towards the H-atoms of benzene rings rather than NH sites of imidazole moieties (shown in Figure 5-3(b)). This clearly demonstrates that it is the negative charge around the benzene ring, which plays a key role for the site selective adsorption of SO_2(II). The theoretically calculated binding affinities (E_b) using different methods for BILP-4@*n*SO_2 (where *n*=2, 4) and BILP-3@*n*SO_2 (where *n*=3, 6) are given in Table 5-2. The result obtained from M06 method is found to be more reliable.

Table 5-2: Binding energies (E_b) of BILP-4@*n*SO_2 (n=2, 4) and BILP-3@*n*SO_2 (n=3, 6) using different methods.

Cluster	**Binding Energy E_b**	
	M06/6-311+G*	**LDA/6-311+G***
BILP-4@2SO_2	0.44 eV (42.01 kJ/mol)	0.76 eV (73.33 kJ/mol)
BILP-4@4SO_2	0.44 eV (42.31 kJ/mol)	0.75 eV (72.36 kJ/mol)
BILP-3@3SO_2	0.43 eV (41.94 kJ/mol)	0.75 eV (71.91 kJ/mol)
BILP-3@6SO_2	0.42 eV (40.31 kJ/mol)	0.70 eV (67.80 kJ/mol)

Theoretical investigations indicate that SO_2 molecules preferentially interact with the electronegative N-atom of benzimidazole-linked polymers (BILPs) which highlight the significance of including imidazole-based polarizable building blocks in adsorbent materials. The large number of binding sites of these polymers allow uptake of multiple SO_2molecules.

5.2.2 Conclusions

BILPs exhibit exceptionally high SO_2 uptakes at ambient conditions facilitated by benzimidazole $N(\delta^-)\ldots S(\delta^+)O_2$ and aryl-$H(\delta^+)\ldots O(\delta^+)$=S=O bonding as predicted by DFT calculations. BILPs possess very high adsorption selectivity for SO_2 over other gases which highlight their potential in selective SO_2 capture for environmental protection and upgrading of methane-rich gases.

References

[1]Quadrelli, R. & Peterson, S. The energy-climate challenge: Recent trends in CO_2 emissions from fuel combustion. *Energy Policy* **35,** 5938–5952 (2007).

[2]Lelieveld, J. & Heintzenberg, J. Sulfate Cooling Effect on Climate Through in-Cloud Oxidation of Anthropogenic SO_2. *Science* **258,** 117–120 (1992).

[3](a) Kikkawa, H., Nakamoto, T., Morishita, M. & Yamada, K. New wet FGD process using granular limestone. *Ind. Eng. Chem. Res.* **41,** 3028–3036 (2002). (b) Ortiz, F. J. G. *et al.* Pilot-plant technical assessment of wet flue gas desulfurization using limestone. *Ind. Eng. Chem. Res.* **45,** 1466–1477 (2006).

[4]Schlapbach, L. & Zuttel, A. Hydrogen-storage materials for mobile applications. *Nature* **414,** 353–358 (2001).

[5]Ma, S. & Zhou, H.-C. Gas storage in porous metal-organic frameworks for clean energy applications. *Chem. Commun.* **46,** 44–53 (2010).

[6](a) Yang, H. *et al.* Progress in carbon dioxide separation and capture: A review. *J. Environ. Sci.* **20,** 14–27 (2008). (b) McKeown, N. B. & Budd, P. M. Exploitation of Intrinsic Microporosity in Polymer-Based Materials. *Macromolecules* **43,** 5163–5176 (2010).

[7]Phan, A. *et al.* Synthesis, Structure, and Carbon Dioxide Capture Properties of Zeolitic Imidazolate Frameworks. *Accounts Chem. Res.* **43,** 58–67 (2010).

[8]Cote, A. P. *et al.* Porous, crystalline, covalent organic frameworks. *Science* **310,** 1166–1170 (2005). (*b*) El-Kaderi, H. M. *et al.* Designed synthesis of 3D covalent organic frameworks. *Science* **316,** 268–272 (2007). (*c*) Cote, A. P., El-Kaderi, H. M., Furukawa, H., Hunt, J. R. & Yaghi, O. M. Reticular synthesis of microporous and mesoporous 2D covalent organic frameworks. *J. Am. Chem. Soc.* **129,** 12914 (2007). (*d*) Lukose, B., Kuc, A. & Heine, T. The Structure of Layered Covalent-Organic Frameworks. *Chem.-Eur. J.* **17,** 2388–2392 (2011).

[9]Li, J.-R., Sculley, J. & Zhou, H.-C. Metal-Organic Frameworks for Separations. *Chem. Rev.* **112,** 869–932 (2012). (b) Keskin, S., van Heest, T. M. & Sholl, D. S. Can Metal-Organic Framework Materials Play a Useful Role in Large-Scale Carbon Dioxide Separations? *ChemSusChem* **3,** 879–891 (2010). (c) D'Alessandro, D. M., Smit, B. & Long, J. R. Carbon Dioxide Capture: Prospects for New Materials. *Angew. Chem.-Int. Edit.* **49,** 6058–6082 (2010).

[10]Belof, J. L., Stern, A. C., Eddaoudi, M. & Space, B. On the mechanism of hydrogen storage in a metal-organic framework material. *J. Am. Chem. Soc.* **129,** 15202–15210 (2007).

[11]Bernardo, P., Drioli, E. & Golemme, G. Membrane Gas Separation: A Review/State of the Art. *Ind. Eng. Chem. Res.* **48,** 4638–4663 (2009).

[12]Becke, A. Density-Functional Thermochemistry .3. the Role of Exact Exchange. *J. Chem. Phys.* **98,** 5648–5652 (1993).

[13]Vosko, S., Wilk, L. & Nusair, M. Accurate Spin-Dependent Electron Liquid Correlation Energies for Local Spin-Density Calculations - a Critical Analysis. *Can. J. Phys.* **58,** 1200–1211 (1980).

[14]Zhao, Y. & Truhlar, D. G. The M06 suite of density functionals for main group thermochemistry, thermochemical kinetics, noncovalent interactions, excited states, and transition elements: two new functionals and systematic testing of four M06-class functionals and 12 other functionals. *Theor. Chem. Acc.* **120,** 215–241 (2008).

[15]M. J. Frisch, G. N. Trucks, H. B. Schlegel et. al., Gaussian, Inc., Wallingford CT, 2009.

[16]Krishnan, R., Binkley, J., Seeger, R. & Pople, J. Self-Consistent Molecular-Orbital Methods .20. Basis Set for Correlated Wave-Functions. *J. Chem. Phys.* **72,** 650–654 (1980).

[17] Mclean, A. & Chandler, G. Contracted Gaussian-Basis Sets for Molecular Calculations .1. 2nd Row Atoms, Z=11-18. *J. Chem. Phys.* **72,** 5639–5648 (1980).

[18]Reed, A., Weinstock, R. & Weinhold, F. Natural-Population Analysis. *J. Chem. Phys.* **83,** 735–746 (1985).

[19]Rowsell, J. L. C. & Yaghi, O. M. Effects of functionalization, catenation, and variation of the metal oxide and organic linking units on the low-pressure hydrogen adsorption properties of metal-organic frameworks. *J. Am. Chem. Soc.* **128,** 1304–1315 (2006).

[20]Furukawa, H. & Yaghi, O. M. Storage of Hydrogen, Methane, and Carbon Dioxide in Highly Porous Covalent Organic Frameworks for Clean Energy Applications. *J. Am. Chem. Soc.* **131,** 8875–8883 (2009).

[21](a) Rabbani, M. G. & El-Kaderi, H. M. Template-Free Synthesis of a Highly Porous Benzimidazole-Linked Polymer for CO_2 Capture and H_2 Storage. *Chem. Mat.* **23,** 1650–1653 (2011). (b) Rabbani, M. G., Reich, T. E., Kassab, R. M., Jackson, K. T. & El-Kaderi, H. M. High CO2 uptake and selectivity by triptycene-derived benzimidazole-linked polymers. *Chem. Commun.* **48,** 1141–1143 (2012).

[22]Dawson, R., Cooper, A. I. & Adams, D. J. Nanoporous organic polymer networks. *Prog. Polym. Sci.* **37,** 530–563 (2012).

Chapter 6

SUMMARY

6.1 Major findings:

In summary, we have studied three different roles of clusters, namely, clusters as superatoms, clusters for elucidating reaction mechanisms, and clusters as a model of polymers for understanding storage and sequestration of gases. Through these examples we demonstrate that clusters can form a bridge across disciplines, in this case between physics, chemistry, and material sciences.

We have shown that superatoms such as superhalogens and superalkalis can be designed to mimic the chemistry of halogen and alkali atoms, respectively. An entirely new class of salts can be synthesized by using superhalogens and superalkalis as building blocks. Our conclusion is based on following specific examples:

(1) The electron affinity of nitrate (NO_3), namely, 4.03 eV is larger than that of halogen and constitutes an unusual superhalogen that contains neither a metal atom nor a halogen atom. Nitrates act as strong oxidizing agents and can produce a large amount of energy when they react with the appropriate fuels. As a result, materials with increasing nitrates contents can have applications as high energy density materials. To increase the nitrate content we designed hyperhalogens by decorating metal atoms such as Li, Mg and Al with nitrates. The large electron affinity of nitrate-based hyperhalogens was confirmed by calculating the ADEs of $Li(NO_3)_2$,

$Mg(NO_3)_3$, and $Al(NO_3)_4$, which are, respectively, 5.69, 6.64, and 6.42 eV. These hyperhalogens were combined with appropriate metal cations to form salts, such as $KLi(NO_3)_2$, $KMg(NO_3)_3$, and $KAl(NO_3)_4$. Total energy calculations confirmed the stability of these salts against fragmentation.

(2) We showed that a new class of superhalogens can be created if superalkalis instead of alkali metal atoms are used at the core. A new kind of salt can also be formed by using a superalkali as the cationic component and superhalogen as anionic component as long as their individual properties are preserved. However, the binding energy of such salts is weak because of their larger size. This type of binding can be advantageous in making the cathode material in batteries where release of a cation with less energy is desirable. Additionally, we showed that it is not always possible to design hyperhalogens using superalkalis as core and superhalogens as ligands. This specifically depends upon the superhalogen ligand used.

(3) We also examined if traditional catalysts can be replaced by superatoms composed of earth-abundant elements. In a recent paper, it was shown that the electronic structure Pd is similar to that of its isoelectronic ZrO cluster. It was then suggested that ZrO may be a replacement catalyst for Pd. Since, catalysts are seldom single atoms, we studied the likelihood that properties of clusters of $(ZrO)_n$ can be similar to those of Pd_n clusters. We have calculated the equilibrium geometries, electronic structure, and binding energies of neutral, cationic, and anionic Pd_n and $(ZrO)_n$ (n=1-5) clusters. In addition, we also studied the reaction of these clusters with H_2, O_2, and CO molecules to investigate the nature of their adsorption and corresponding adsorption energies. From this study we concluded that, with the exception of a few cases involving the interaction of hydrogen, neither the electronic structure nor the interactions of gas molecules are

similar. In particular, we found the interaction of Pd_n with O_2 to be qulitatively different from that bewteen $(ZrO)_n$ and O_2. Our study did not support the ansatz put forward by previous study.

A synergistic study of the electronic structure and equilibrium geometries of neutral and anionic Cu_n, $Cu_{n-1}H$, Ag_n, and $Ag_{n-1}H$ (n = 2–5) clusters using photoelectron scpoectroscopy experiment and density functional theory-based calculations showed that H can mimic the properties of coinage metal atoms in anionic clusters containing more than 3 atoms. While the charge on H atom is similar to that found for H in metal, the charge on the Cu atoms varies over a wide margin. In anionic clusters, the added electron is shared between the Cu atoms, thus bringing the charge on the H atom close to that of the corresponding Cu atom. In the same manner, in $Ag_{n-1}H$ cluster, the charge on the H atom is similar to that on the Ag atom it replaces in the Ag_n clusters. Since replacement of a metal atom by H-atom retains the property of the cluster, for future studies it will be interesting to see if the reactivity of the clusters is affected by H substitution.

We showed that a cluster model can be effective in accounting for the experimental data on the storage of gas molecules in polymeric materials. We showed that the inclusion of highly polarizable and halogenated building units into the framework of borazine-linked polymers (BLPs) can significantly enhance their performance in gas separation applications, particularly for CO_2 gas. The theoretical calculations also highlight exceptionally high SO_2 uptakes by benzimidazole-linked polymers (BILPs) which is facilitated by benzimidazole $N(\delta^-)\ldots S(\delta^+)O_2$ and aryl-$H(\delta^+)\ldots O(\delta^+)$=S=O bonding.

6.2 Ongoing research:

Currently, we are working on the design of halogen-free electrolytes for lithium ion batteries. Usually, the electrolytes of this cell contain a mixture of organic solvents and Li salts. We found that, the anionic component of most of the commercially available Li salts are superhalogens such as PF_6^-, BH_4^-, $FePO_4^-$, $FeClO_4^-$, $N(SO_2F)_2^-$, $N(SO_2CF_3)_2^-$ etc. Most of these electrolytes contain F and are hygroscopic. We are working on new Li salts which are organic and halogen free. We are also calculating the Li binding energy in these salts and the manner they react with water molecules to improve battery performance.

Another project that is nearly complete is a systematic study of the interaction of small Au clusters with O-atom(s). While our motivation was to understand gold-catalysis, during our study we found that most of these clusters exhibit unusual superhalogen properties. They neither follow the conventional superhalogen rule nor do they satisfy any electron counting rule. Work is also under progress to design unique salts containing zintl inspired superalkali and aliphatic superhalogens as building blocks.

Appendix I

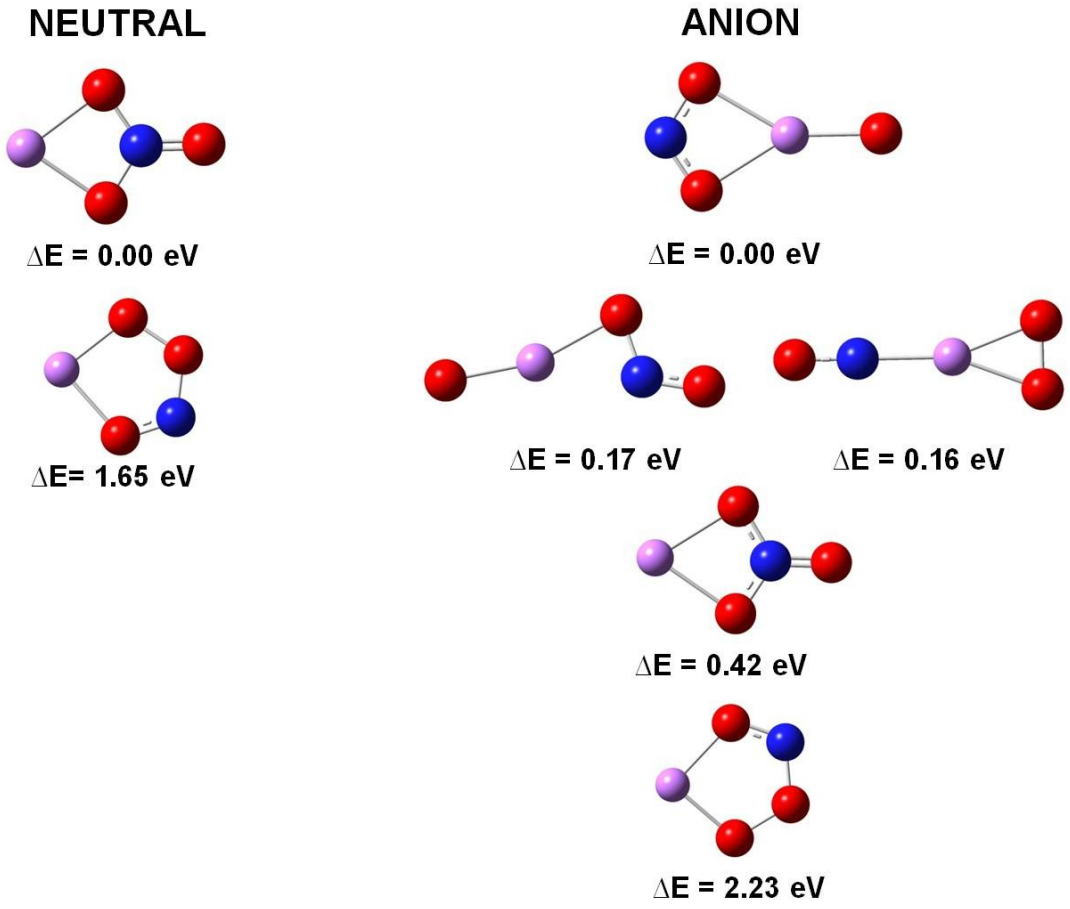

Figure I1: Isomers of neutral and anionic clusters of $LiNO_3$ optimized using B3LYP/6-311++G** showing the energy difference (ΔE) measured with respect to its ground state counterpart.

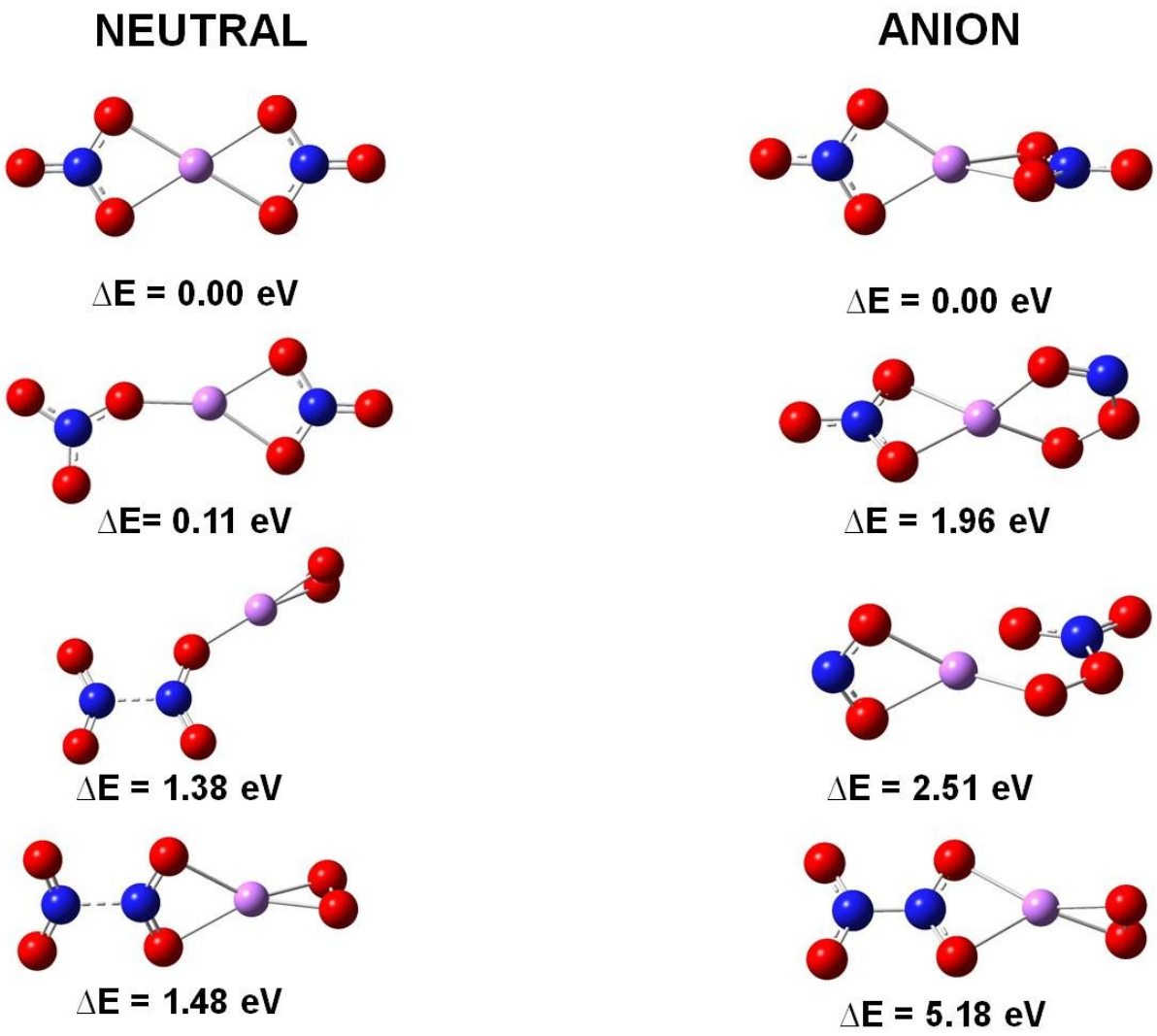

Figure I2: Isomers of neutral and anionic clusters of $Li(NO_3)_2$ optimized using B3LYP/6-311++G** showing the energy difference (ΔE) measured with respect to its ground state counterpart.

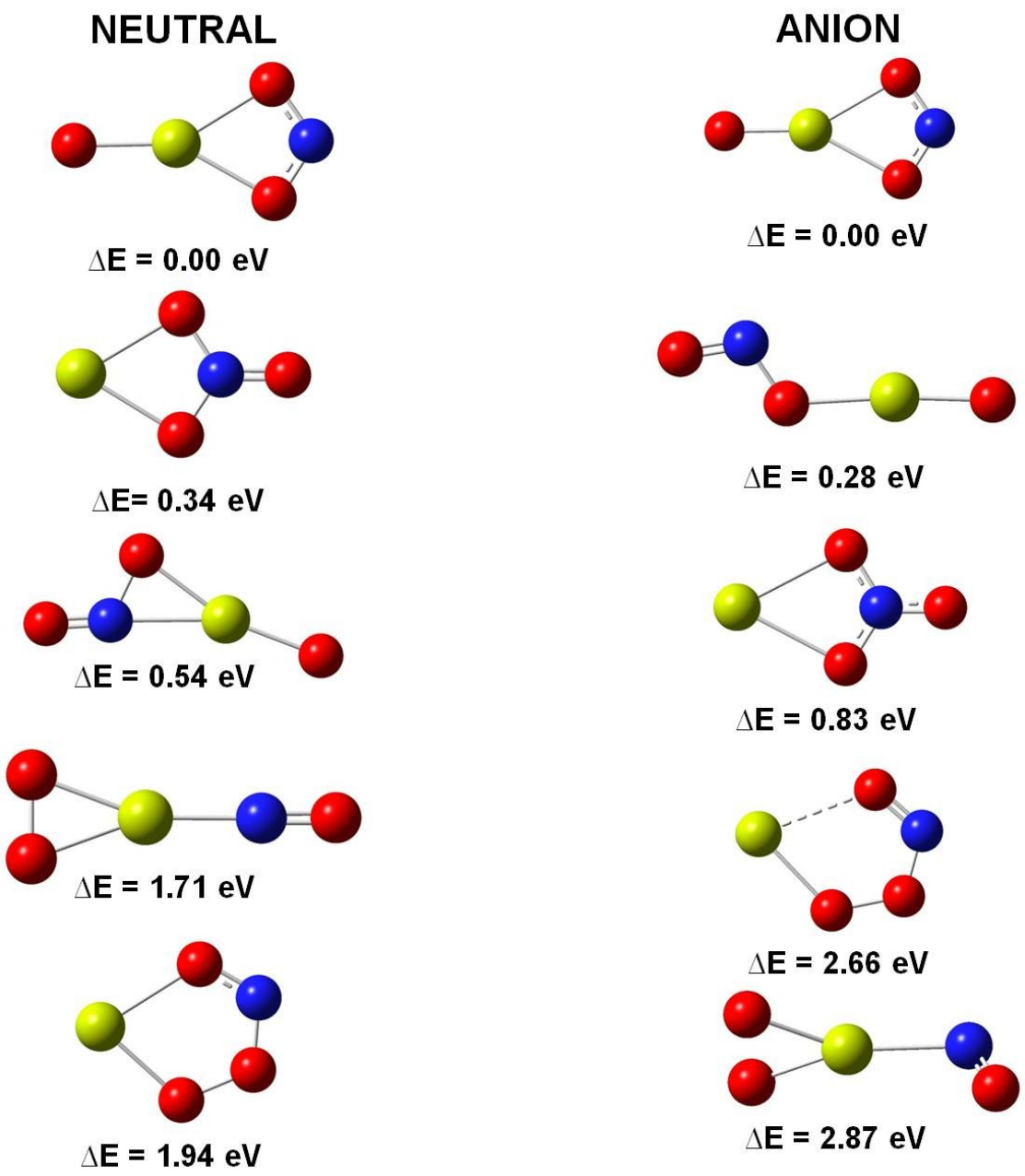

Figure I3: Isomers of neutral and anionic clusters of $MgNO_3$ optimized using B3LYP/6-311++G** showing the energy difference (ΔE) measured with respect to its ground state counterpart.

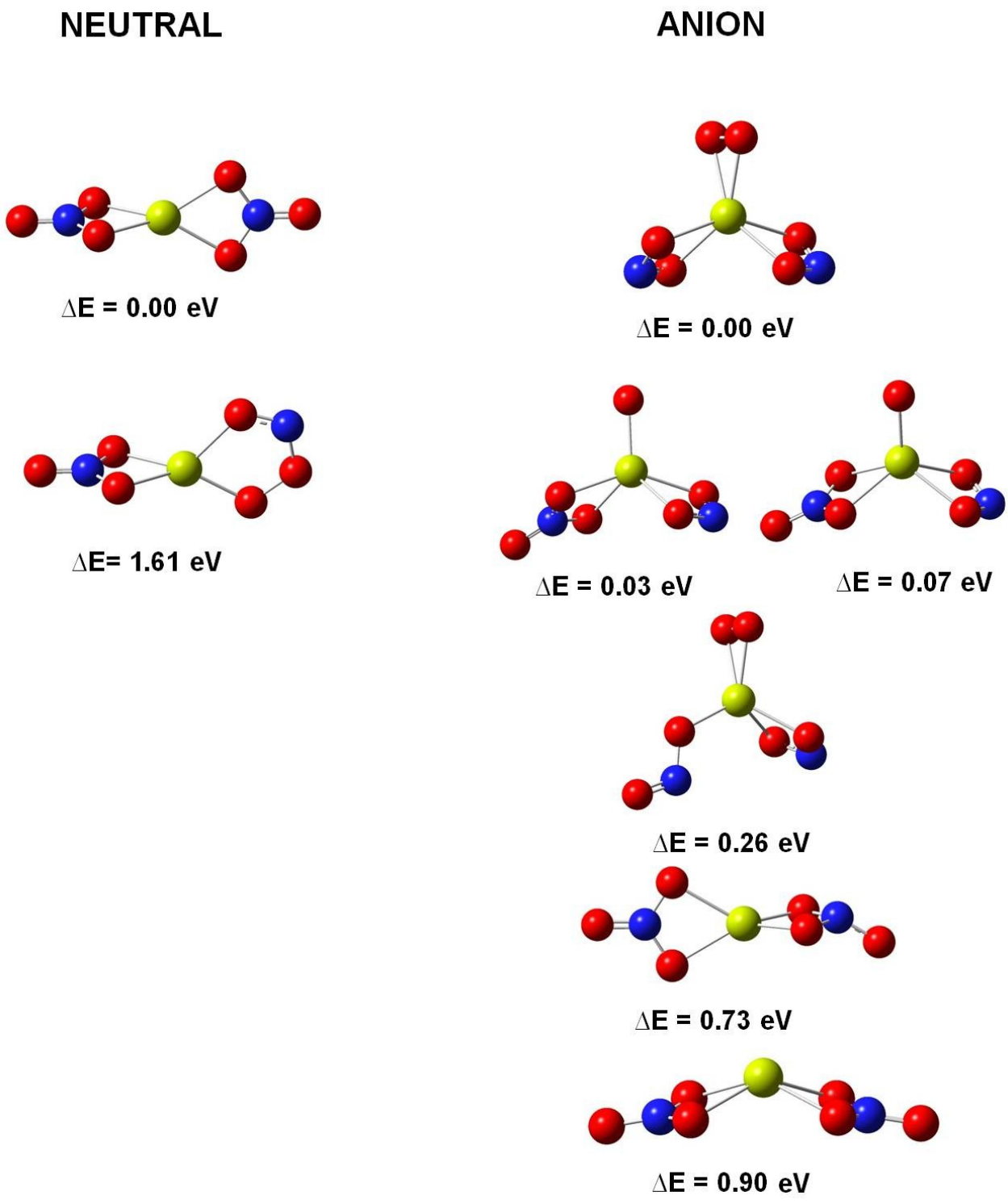

Figure I4: Isomers of neutral and anionic clusters of $Mg(NO_3)_2$ optimized using B3LYP/6-311++G** showing the energy difference (ΔE) measured with respect to its ground state counterpart.

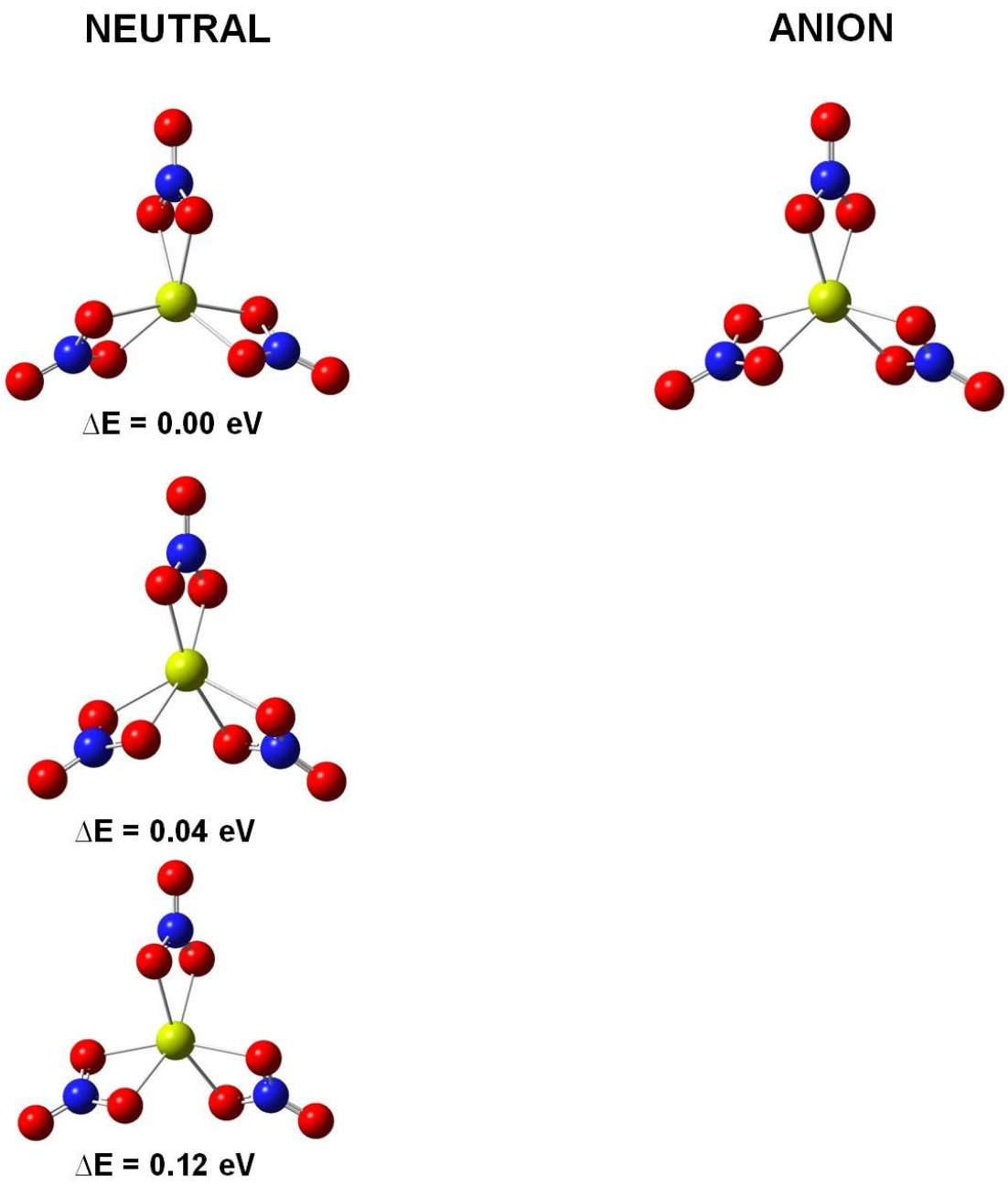

Figure I5: Isomers of neutral and anionic clusters of $Mg(NO_3)_3$ optimized using B3LYP/6-311++G** showing the energy difference (ΔE) measured with respect to its ground state counterpart.

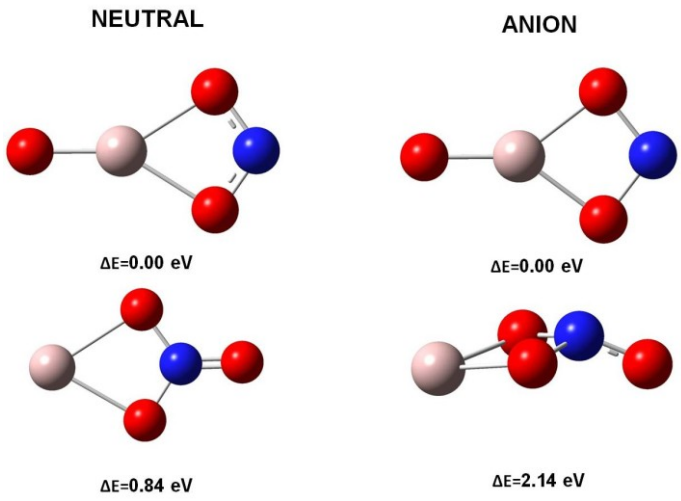

Figure I6: Isomers of neutral and anionic clusters of $AlNO_3$ optimized using B3LYP/6-311++G** showing the energy difference (ΔE) measured with respect to its ground state counterpart.

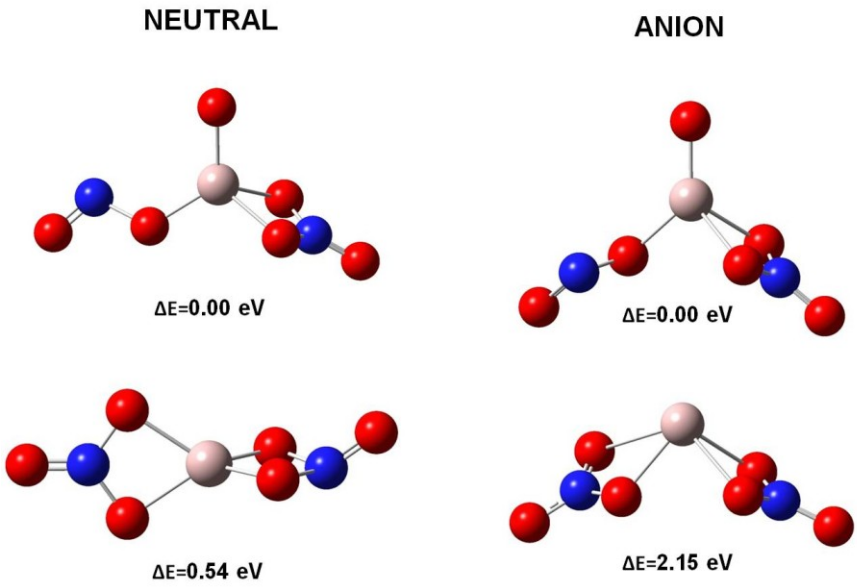

Figure I7: Isomers of neutral and anionic clusters of $Al(NO_3)_2$ optimized using B3LYP/6-311++G** showing the energy difference (ΔE) measured with respect to its ground state counterpart.

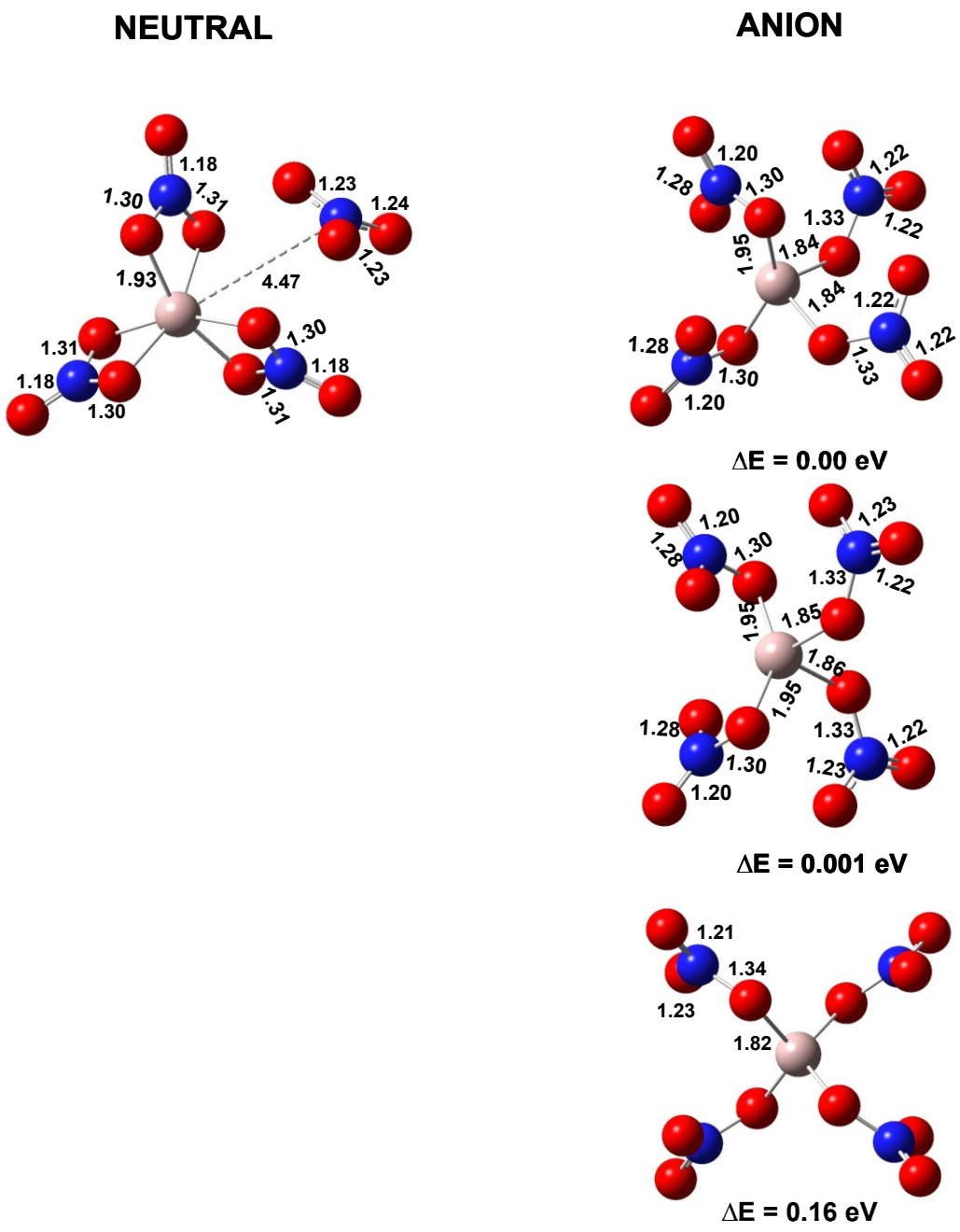

Figure I8: Isomers of neutral and anionic clusters of $Al(NO_3)_4$ optimized using B3LYP/6-311++G** showing the energy difference (ΔE) measured with respect to its ground state counterpart.

Appendix II

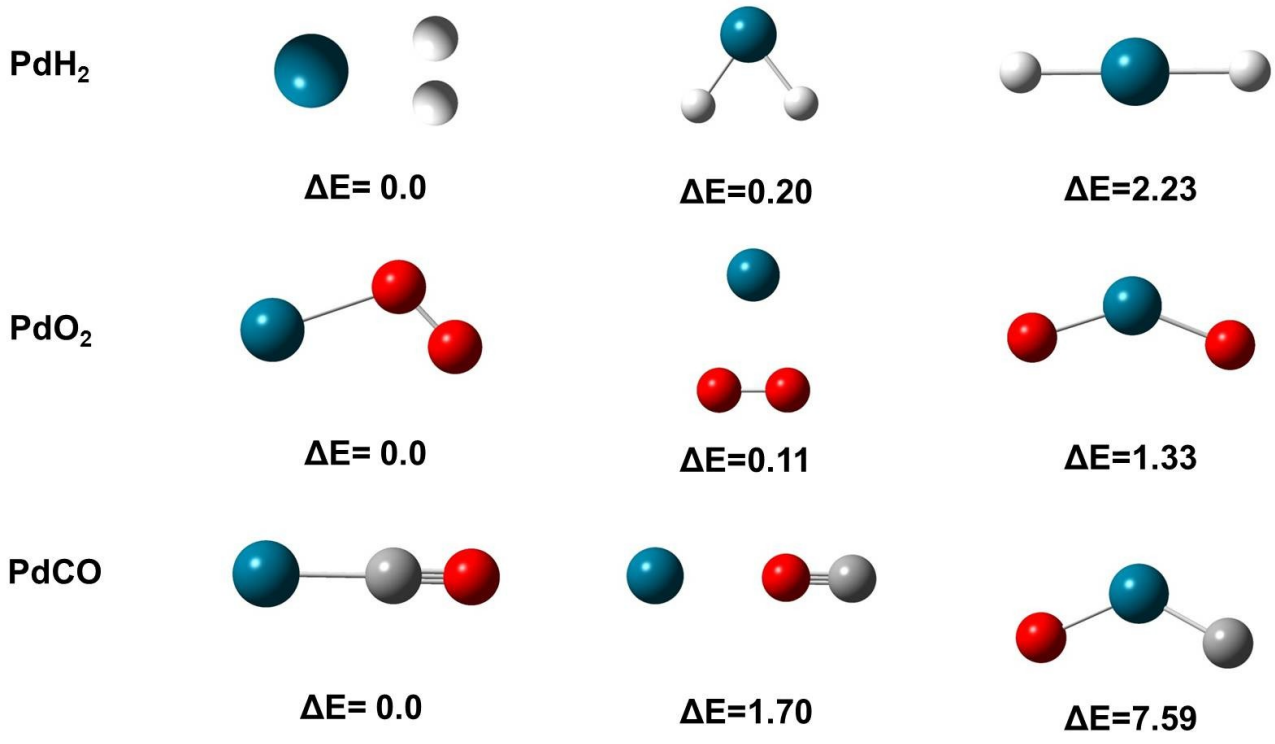

Figure II1: Isomers for the adsorption of H_2, O_2 and CO to neutral Pd. The energy difference (ΔE) is measured with respect to its ground state.

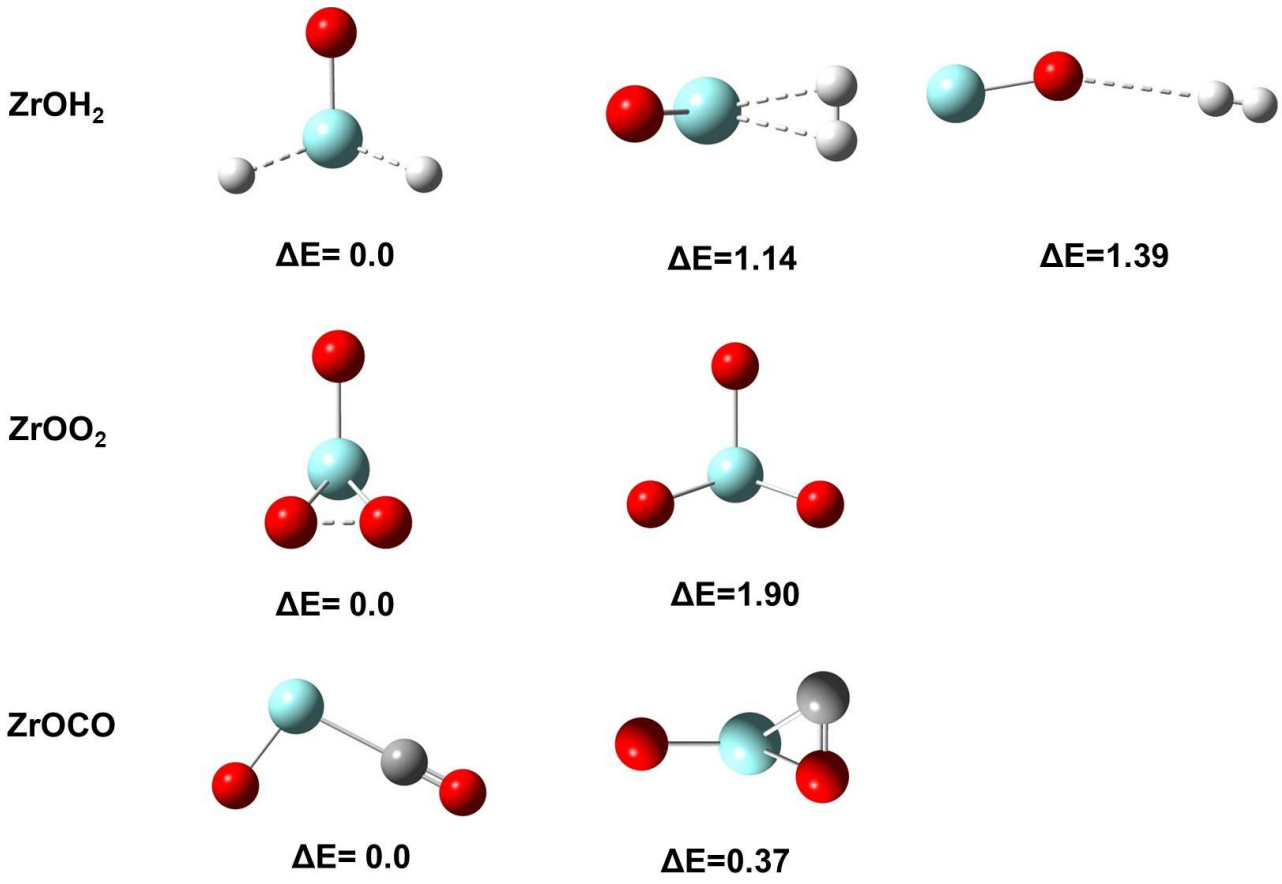

Figure II2: Isomers for the adsorption of H_2, O_2 and CO to neutral ZrO. The energy difference (ΔE) is measured with respect to its ground state.

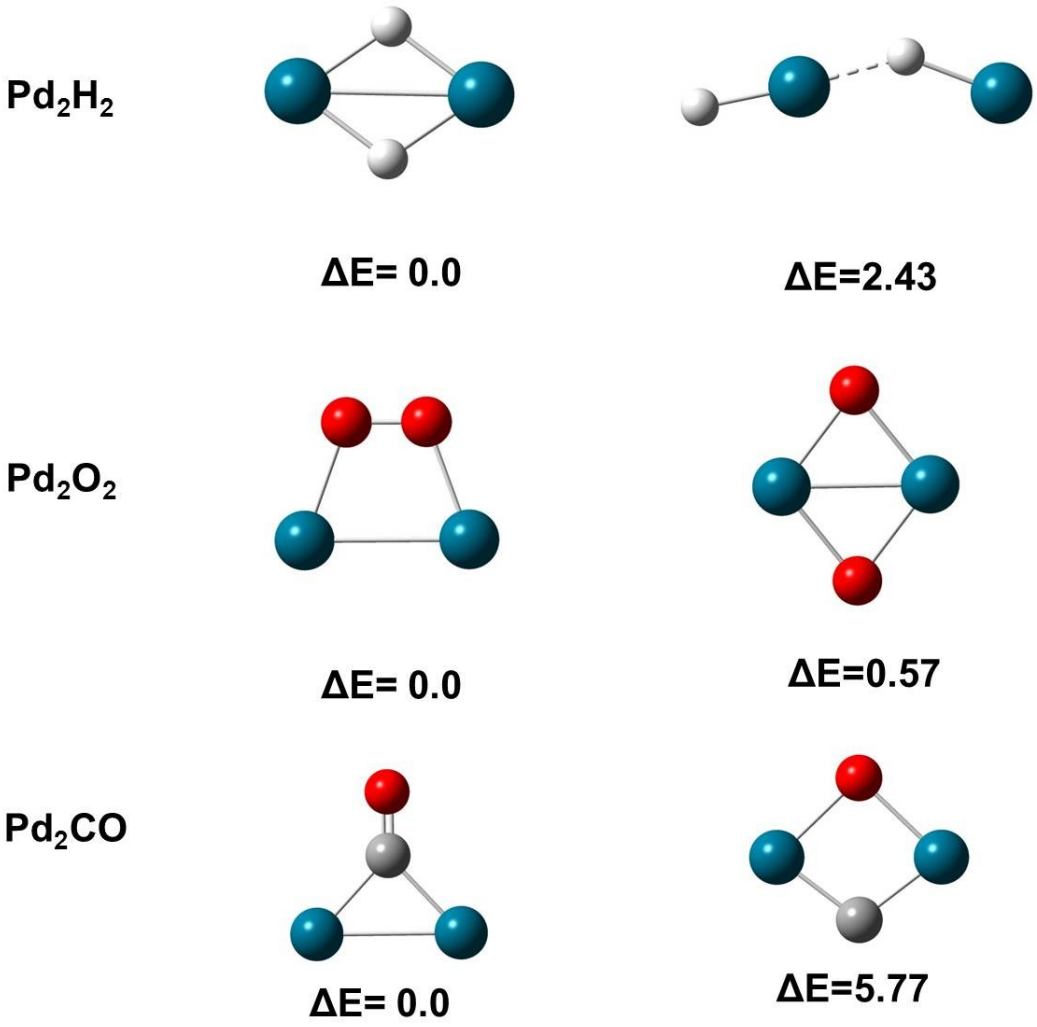

Figure II3: Isomers for the adsorption of H_2, O_2 and CO to neutral Pd_2. The energy difference (ΔE) is measured with respect to its ground state.

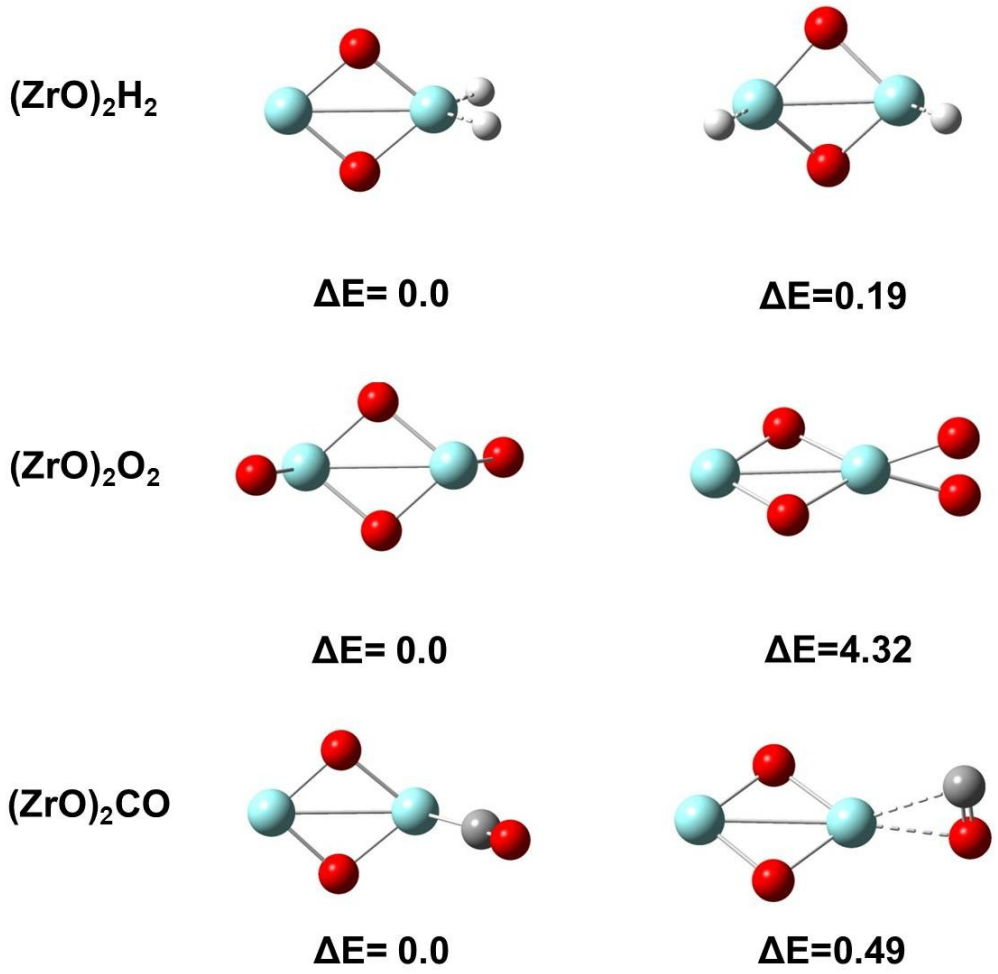

Figure II4: Isomers for the adsorption of H_2, O_2 and CO to neutral $(ZrO)_2$. The energy difference (ΔE) is measured with respect to its ground state.

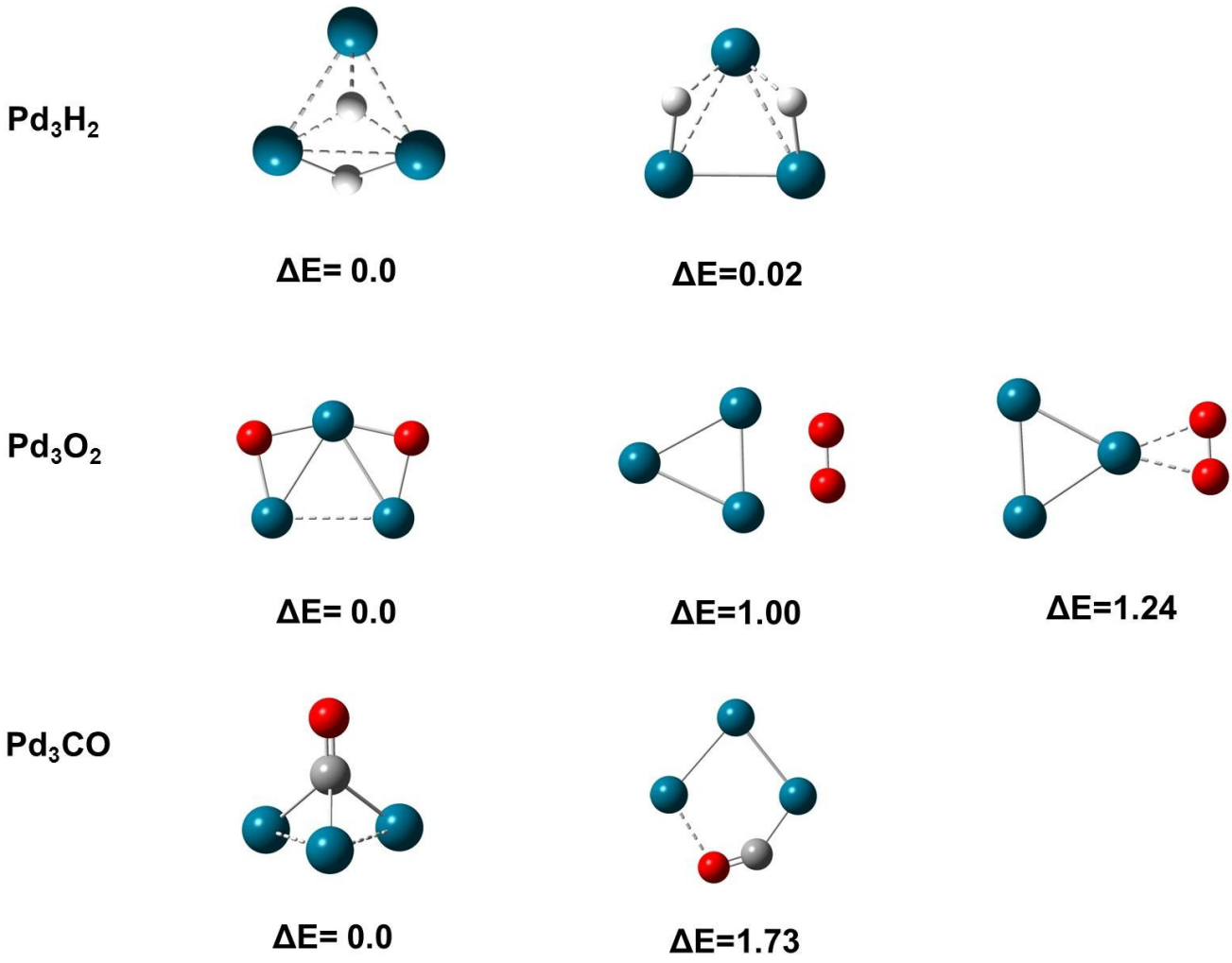

Figure II5: Isomers for the adsorption of H_2, O_2 and CO to neutral Pd_3. The energy difference (ΔE) is measured with respect to its ground state.

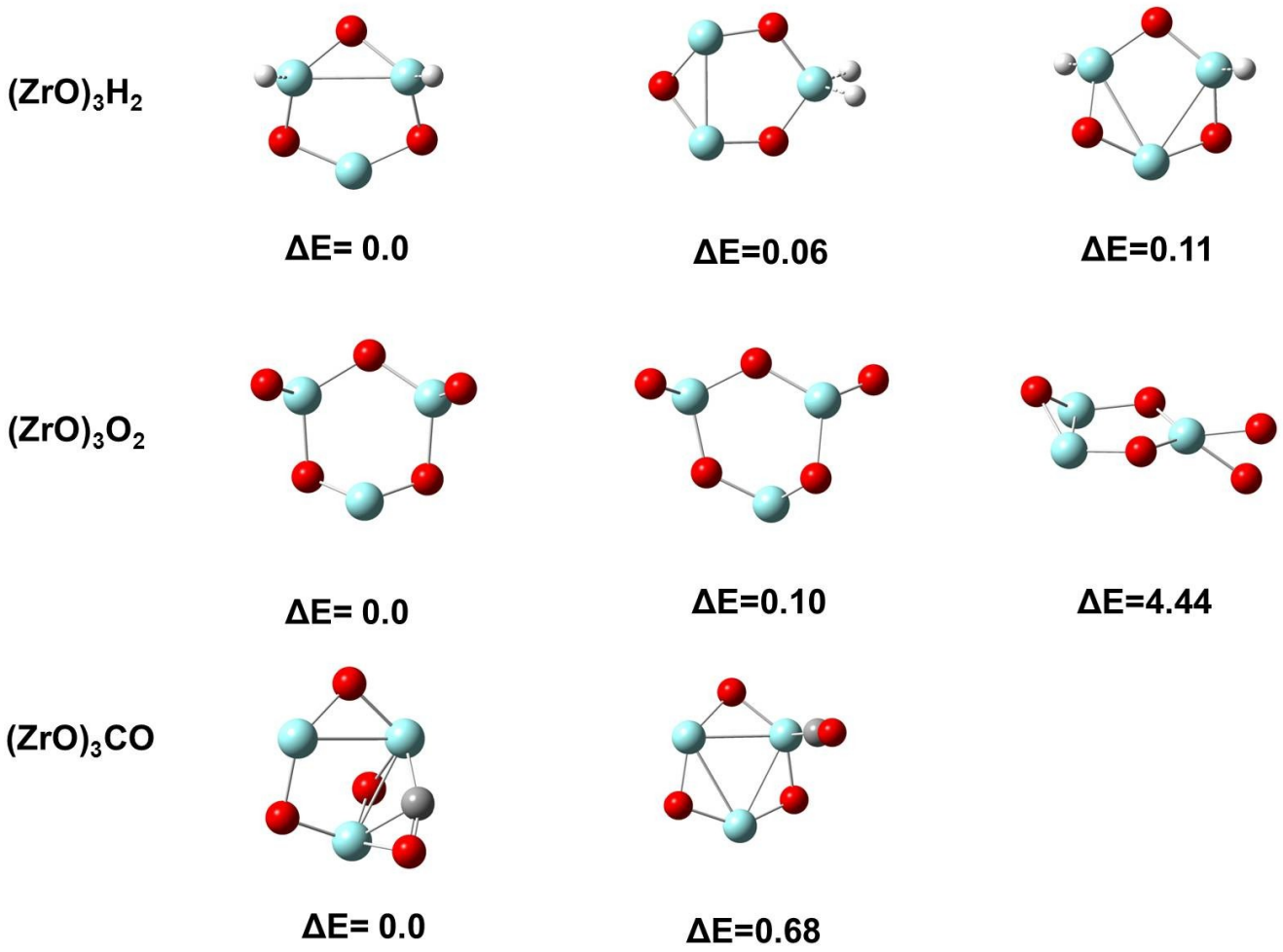

Figure II6: Isomers for the adsorption of H_2, O_2 and CO to neutral $(ZrO)_3$. The energy difference (ΔE) is measured with respect to its ground state.

Appendix III

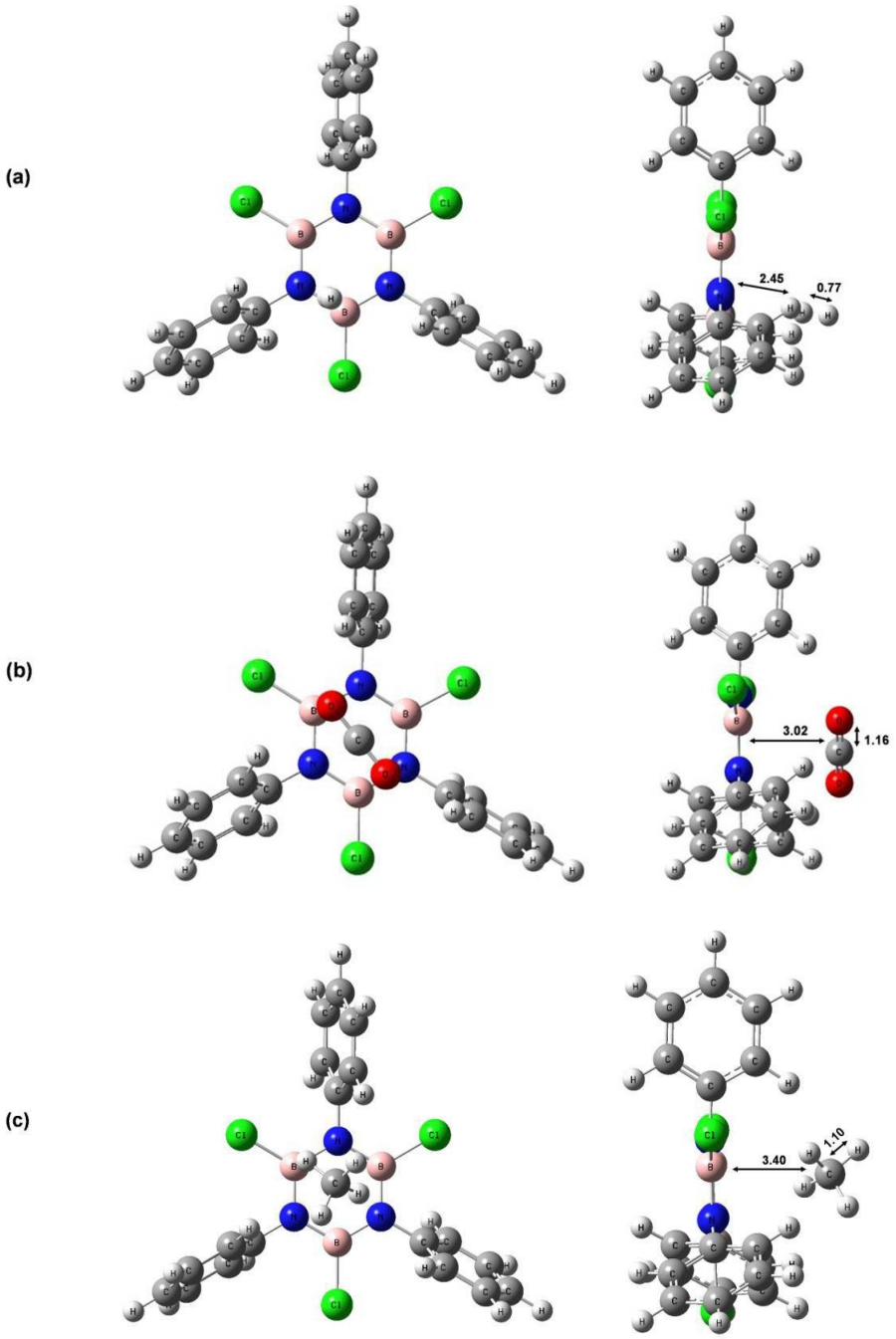

Figure III1: Optimized geometries of (a) H_2, (b) CO_2 and (c) CH_4 adsorbed on chlorinated borazine calculated at LDA/6-311+G* level of theory. The bond lengths are in Å. Front and side views are given on the left and right panel, respectively.

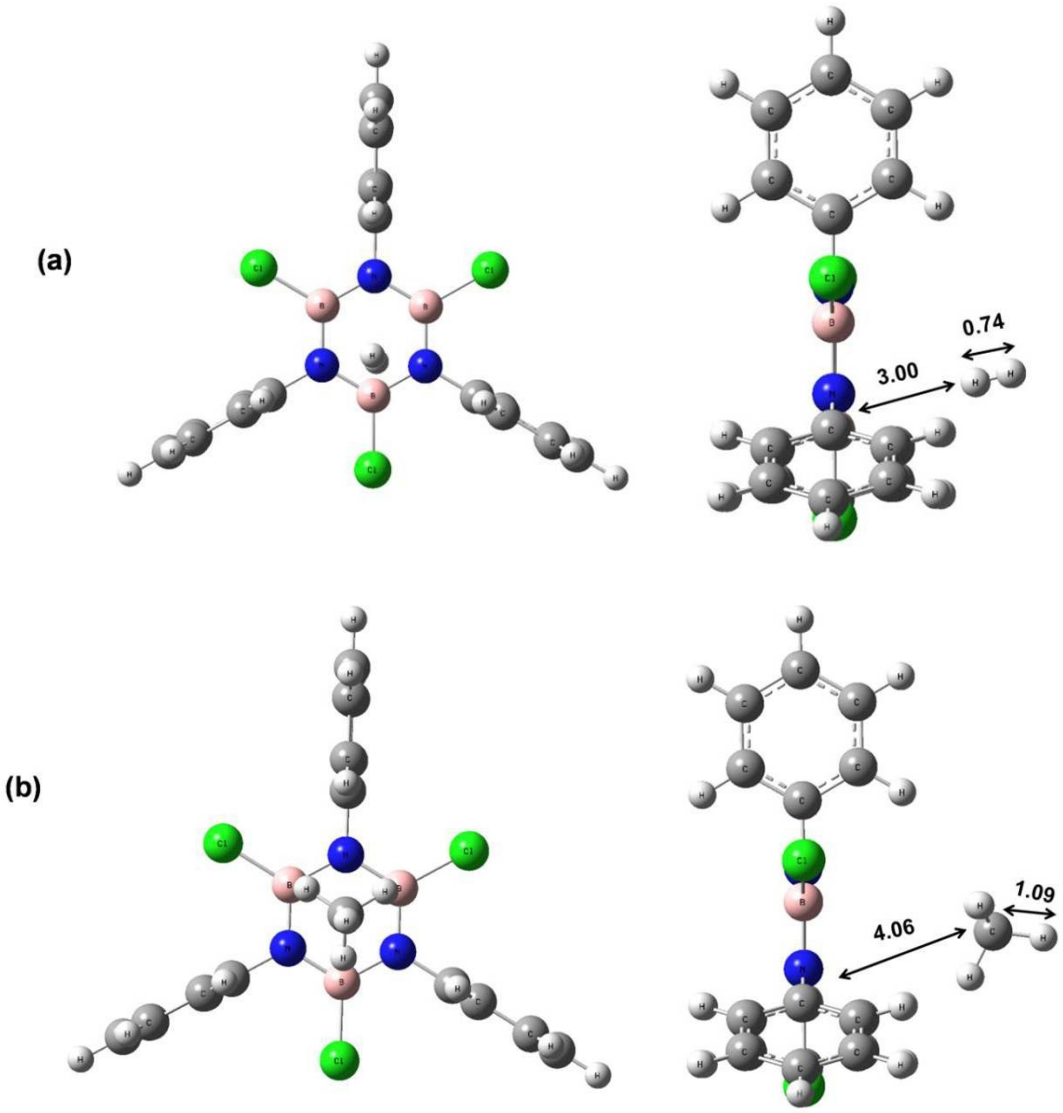

Figure III2: Optimized geometries of (a) H_2, (b) CH_4 adsorbed on chlorinated borazine calculated at B3LYP/6-311+G* level of theory. The bond lengths are in Å. Front and side views are given on the left and right panel, respectively.

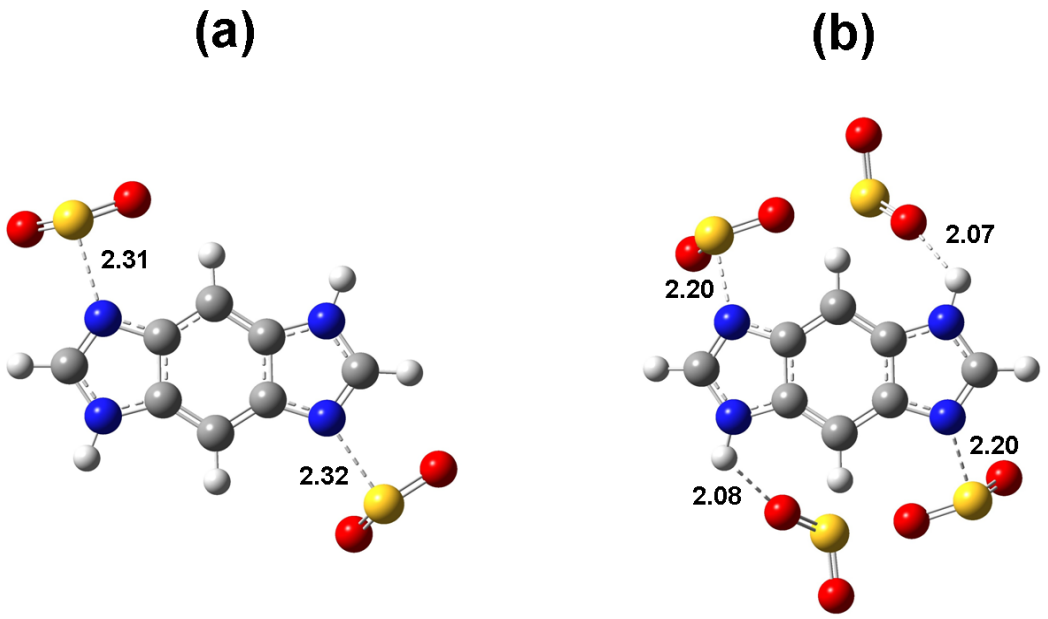

FigureIII3: Fully optimized geometries of (a) BILP-4@2SO_2 and (b) BILP-4@4SO_2 calculated at LDA/6-311+G* level of theory. The bond lengths are in Å.

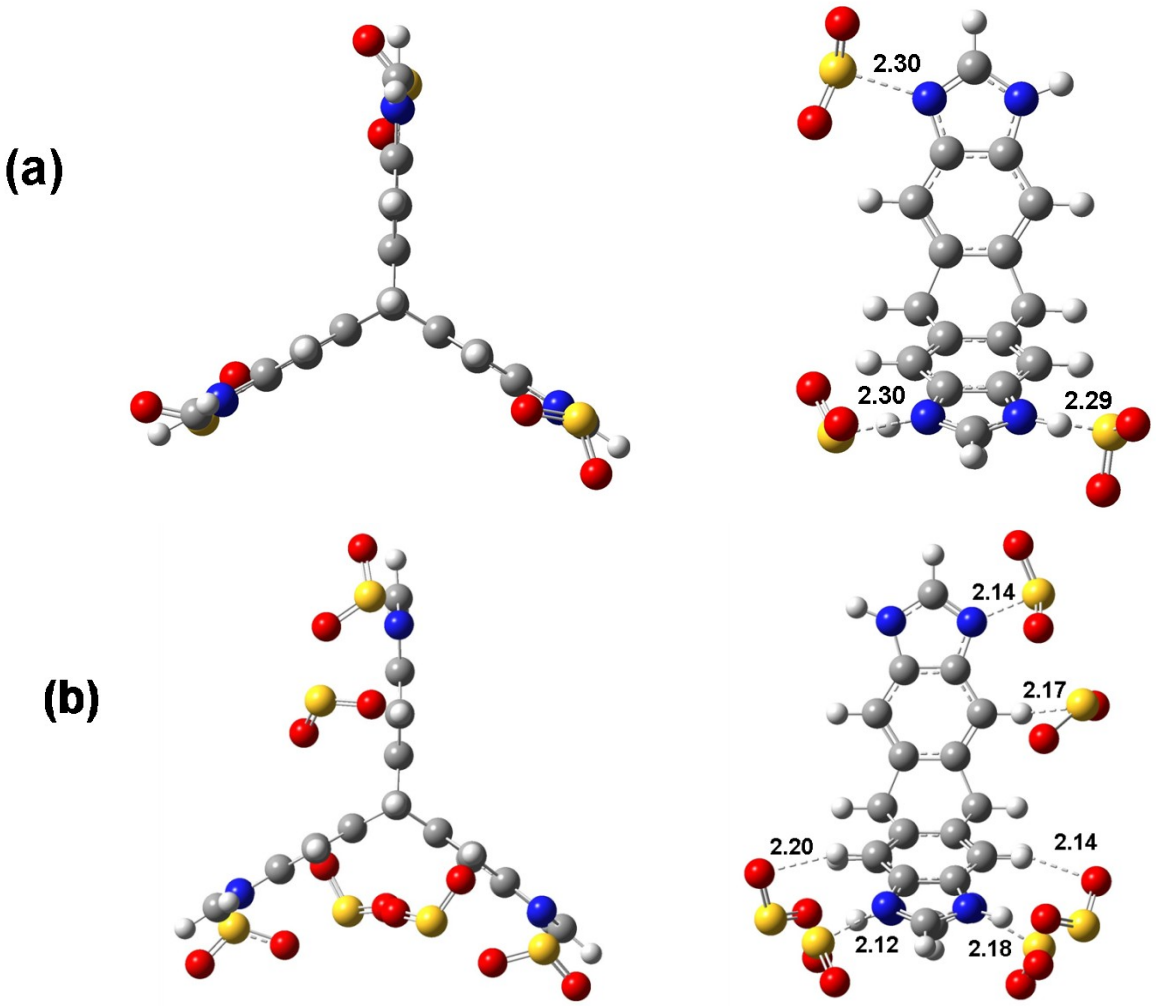

Figure III4: Partially optimized geometries of (a) BILP-3@3SO_2 and (b) BILP-3@6SO_2 calculated at LDA/6-311+G* level of theory. The bond lengths are in Å. Front and side views are given on the left and right panel respectively.

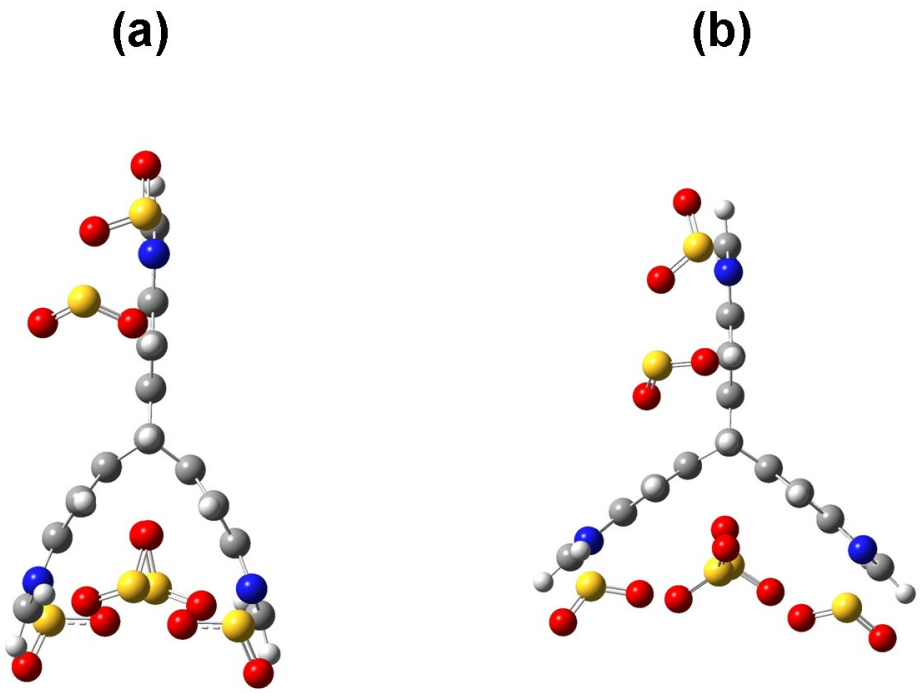

Figure III5: Fully Optimized geometries of BILP-3@6SO_2 calculated at (a) LDA/6-311+G* and (b) M06/6-311+G* level of theory.

Table III-1: Binding affinities (E_b) of BILP-3@*n*SO_2 (n=3, 6) using different methods after fully optimizing the geometries:

Cluster	**Binding Energy E_b**	
	LDA/6-311+G*	**M06/6-311+G***
BILP-3@3SO_2	-0.75 eV (-72.36 kJ/mol)	-0.44 eV(-42.45 kJ/mol)
BILP-3@6SO_2	-0.79 eV (-76.22 kJ/mol)	-0.46 eV(-44.38 kJ/mol)